Probing the Trojan-Hilda-KBO Connection: An Empirical Test of Dynamical Instability Models of Solar System Evolution

Thesis by
Ian Yu Wong

In Partial Fulfillment of the Requirements for the
degree of
Doctor of Philosophy in Planetary Science

CALIFORNIA INSTITUTE OF TECHNOLOGY
Pasadena, California

2018
Defended February 20, 2018

Ian Yu Wong
ORCID: 0000-0001-9665-8429

ACKNOWLEDGEMENTS

On a sunny morning in June 2013, when I stepped onto the Caltech campus and strolled into South Mudd to start off my graduate student life, I had little background in planetary science and was largely unaware of the myriad paths that lay before me – a true science novice. While my interest in astronomy in general and planets in particular had been cultivated for many years, I had not yet gotten a taste of what planetary science research entailed. I would have been hard-pressed to explain with any confidence why Pluto had been demoted to dwarf planet status, or what the generally-accepted theory of planet formation was. And I certainly wasn't cognizant of such a thing as Jupiter Trojans.

Over the past four-and-a-half years, countless individuals have helped me in immeasurable ways to mature as a scientist, to develop a deep and broad knowledge of astronomy, and to cultivate a skill set that will prove invaluable in my future endeavors as an independent researcher. I would like to begin by acknowledging first and foremost my thesis adviser Professor Mike Brown, without whom none of this would have been possible. From teaching me the ropes of telescope observing and proposal writing, to the long discussions about the minutiae of data analysis and interpretation, his devotion to nurturing me as a budding researcher and his philosophy of encouraging self-reliance and independent thinking from an early stage have been indispensable throughout my graduate work. Working with Mike has been instrumental in helping me define myself as a scientist and blaze my path forward as I move on from graduate life to a postdoctoral fellowship position at MIT. I would also like to acknowledge the others in Mike's research group, both old and new – Elizabeth Bailey, Samantha Trumbo, Harriet Brettle, Katherine de Kleer, James Tuttle Keane, Patrick Fischer, and Henry Ngo – who have always lent a receptive ear during group meetings, contributed insightful comments and suggestions, and witnessed the latest developments in my research as they happened.

While only my academic adviser on paper, Professor Heather Knutson has very much been a co-adviser throughout the entirety of my time at Caltech. Beginning from my first-year project on the secondary eclipses of XO-3b, I have continued working with her and a large group of collaborators on intensive atmospheric characterization of exoplanets, ranging from multiband near-infrared phase curve studies of hot Jupiters to cutting-edge transmission spectroscopy of cool gas giants. My research with Heather has opened up a whole new facet of planetary science and enriched my

scientific endeavors with a different perspective on the same fundamental questions of planet formation and solar system evolution. My exoplanet studies have also greatly honed my programming and data analysis acumen, with substantial benefits to my primary thesis research, as well as my future work. Heather has always taken great interest in my latest progress in minor bodies research and offered encouraging advice on how to be an effective researcher and responsible collaborator.

To the others in the Planetary Science entering class of 2013 – Dana Anderson, Peter, Buhler, Pushkar Kopparla, and Christopher Spalding – I would like to extend my most heartfelt gratitude. From our first classes together, periodic discussions about research, life, current events, etc. both in the office and out, to the social gatherings, we have all helped each other grow immensely during our time here at Caltech. And to the Planetary Science administrative staff, who have made the department run exceptionally smoothly with their professionalism and experience, I sincerely thank you for the support you have provided me and everyone else in the department, whether it be processing reimbursements for conference travel or even just the cookies and apple cider during the holidays.

Last, and certainly not least, I want to thank my parents – Jing Wu and Wing Wong – for their love and support during my graduate student years. They have pushed me to work hard and stay focused, especially during the times I felt the most discouraged or unmotivated. Whenever I needed to talk to them, for whatever reason, they were always there to chat or a short (by LA standards) 90-minute drive away. I love you Mom and Dad. And to my parents' pet cat Sushi, who tragically passed a few weeks before my thesis defense, thank you for being the sweetest kitty and providing affection and companionship through all my highs and lows over the past eight years. I will never forget the cherished times we spent together on my visits home.

ABSTRACT

In recent decades, the paradigm of solar system formation has undergone radical change. Many current models posit that a significant reorganization of the outer Solar System occurred after the end of planet formation. Specifically, it is hypothesized that Jupiter and Saturn crossed a mutual mean motion resonance, leading to a chaotic expansion of the ice giants' orbits that disrupted the large population of planetesimals situated further out. While the majority of these bodies were ejected from the Solar System, a fraction of them were retained as the present-day Kuiper Belt, while others were scattered inward and captured into resonances with Jupiter to become the Trojans and Hildas. These dynamical instability models invariably predict that the Trojans, Hildas, and Kuiper Belt objects (KBOs) were sourced from the same primordial body of outer solar system planetesimals. Therefore, a comparative exploration of these minor body populations serves as one of the definitive observational tests of our present understanding of solar system evolution. Over the past four-and-a-half years, I have carried out a diverse series of systematic studies aimed at synthesizing a detailed picture of Trojan, Hildas, and KBOs. By combining novel analyses of archival data with new photometric surveys, I have derived the first debiased color distributions of Trojans and KBOs and expanded our knowledge of their respective size distributions. In addition, I have explored the peculiar color bimodality attested in the all three asteroid populations, which indicates the presence of two sub-populations. Utilizing the full body of observations, I have formulated the first self-consistent hypothesis outlining the formation, composition, and dynamical/chemical evolution of the primordial outer solar system planetesimals, with special attention given to explaining the color bimodality, size distribution shapes, and collisional families. My results lay the groundwork for future studies with next-generation instruments and ultimately, the Trojan flyby mission *Lucy*.

PUBLISHED CONTENT AND CONTRIBUTIONS

Wong, I. & Brown, M. E. (2015). "The color-magnitude distribution of small Jupiter Trojans". *Astronomical Journal*, 150, 174. DOI: 10.1088/0004-6256/150/6/174.

[I.W. assisted in the telescope observations, carried out the reduction of the telescope data and analysis, and prepared the manuscript for publication. M.E.B. designed and led the observations and advised the analysis and interpretation.]

Wong, I. & Brown, M. E. (2016). "A hypothesis for the color bimodality of Jupiter Trojans". *Astronomical Journal*, 152, 90. DOI: 10.3847/0004-6256/152/4/90.

[I.W. carried out the modeling and data analysis and prepared the manuscript for publication. M.E.B. advised the analysis and interpretation.]

Wong, I. & Brown, M. E. (2017a). "The bimodal color distribution of small Kuiper Belt objects". *Astronomical Journal*, 153, 145. DOI: 10.3847/1538-3881/aa60c3.

[I.W. assisted in the telescope observations, carried out the reduction of the telescope data and analysis, and prepared the manuscript for publication. M.E.B. designed and led the observations and advised the analysis and interpretation.]

Wong, I. & Brown, M. E. (2017b). "The color-magnitude distribution of Hilda asteroids: Comparison with Jupiter Trojans". *Astronomical Journal*, 153, 69. DOI: 10.3847/1538-3881/153/2/69.

[I.W. carried out the data analysis and collision simulations and prepared the manuscript for publication. M.E.B. advised the analysis and interpretation.]

Wong, I., Brown, M. E., & Emery, J. P. (2014). "The differing magnitude distributions of the two Jupiter Trojan color populations". *Astronomical Journal*, 148, 112. DOI: 10.1088/0004-6256/148/6/112.

[I.W. carried out the data analysis and collision simulations and prepared the manuscript for publication. M.E.B. advised the analysis and interpretation. J.P.E. contributed suggestions in the manuscript revision process.]

Wong, I., Brown, M. E., & Emery, J. P. (2017). "0.7 – 2.5 μm spectra of Hilda asteroids". *Astronomical Journal*, 154, 104. DOI: 10.3847/1538-3881/aa8406.

[I.W. applied for, designed, and carried out the observations, led the data reduction and analysis, and prepared the manuscript for publication. M.E.B. and J.P.E. advised the observation planning and data analysis.]

TABLE OF CONTENTS

Acknowledgements . . . iii
Abstract . . . v
Published Content and Contributions . . . vi
Table of Contents . . . vii
List of Illustrations . . . ix
List of Tables . . . xix
Chapter I: Introduction . . . 1
Chapter II: The differing magnitude distributions of the two Jupiter Trojan color populations . . . 7
2.1 Introduction . . . 7
2.2 Trojan data . . . 9
2.3 Analysis . . . 15
2.4 Discussion . . . 24
2.5 Conclusion . . . 32
Chapter III: The color-magnitude distribution of small Jupiter Trojans . . . 36
3.1 Introduction . . . 37
3.2 Observations . . . 38
3.3 Analysis . . . 48
3.4 Discussion . . . 57
3.5 Conclusion . . . 63
Chapter IV: A hypothesis for the color bimodality of Jupiter Trojans . . . 67
4.1 Introduction . . . 68
4.2 Colors of Trojans and KBOs . . . 70
4.3 Volatile loss model . . . 72
4.4 Surface colors . . . 76
4.5 Conclusion . . . 82
Chapter V: The color-magnitude distribution of Hilda asteroids: Comparison with Jupiter Trojans . . . 87
5.1 Introduction . . . 88
5.2 Data and analysis . . . 89
5.3 Discussion . . . 95
5.4 Conclusion . . . 101
Chapter VI: The bimodal color distribution of small Kuiper Belt objects . . . 105
6.1 Introduction . . . 105
6.2 Observations . . . 108
6.3 Data analysis . . . 111
6.4 Discussion . . . 117
6.5 Conclusion . . . 124
Chapter VII: 0.7 – 2.5 μm spectra of Hilda asteroids . . . 128

7.1 Introduction 128
7.2 Observations and data reduction 130
7.3 Results and discussion 131
7.4 Conclusion 142
Chapter VIII: Concluding remarks and Future work 147
8.1 Evaluating the Trojan-Hilda-KBO connection 147
8.2 Experimental study of Trojan surface analogs 149
8.3 Further spectroscopic study 150
8.4 JWST, *Lucy*, and beyond 153

LIST OF ILLUSTRATIONS

Number *Page*

2.1 Distribution of spectral slopes of all 254 Trojans in the Sloan sample with $H < 12.3$ (solid green), and the distributions of spectral slopes of 24 Trojans classified into the LR and R populations per Emery et al. (2011) and Grav et al. (2012) (blue with diagonal hatching and red with cross hatching, respectively). The best-fit Gaussian distribution functions for the two color populations are shown as black dashed lines. 14

2.2 Plot of the unscaled cumulative magnitude distributions for the main Trojan sample (black circles) and the categorized R and LR color populations (red squares and blue triangles, respectively). These data have not yet been corrected for incompleteness. 16

2.3 Plot of the ratio between the cumulative number of objects in the Sloan sample and the cumulative number of objects in the main sample for various absolute magnitude bins (red circles). The black dashed line indicates the average value R_* for bins with $H = 10.0 \rightarrow 11.2$. 18

2.4 Plot depicting the scaled (white squares) and unscaled (black circles) cumulative magnitude distributions for the total Trojan population, along with the best-fit curve describing the true Trojan cumulative distribution. 21

2.5 Plot depicting the scaled (magenta squares) and unscaled (red circles) cumulative magnitude distributions for R population, along with the best-fit curve describing the true cumulative distribution. 22

2.6 Plot depicting the scaled (cyan triangles) and unscaled (blue circles) cumulative magnitude distributions for LR population, along with the best-fit curve describing the true cumulative distribution. 23

2.7 Comparison between the results from the best test run ($\alpha_1 = 1.11$, $\alpha_2 = 0.47$, $H_0 = 7.09$, $H_b = 8.16$, $c = 6$, $k = 4.5$) and the observed Trojan magnitude distributions. 30

3.1 Locations of the 147 observed Subaru Suprime-Cam fields, projected in geocentric ecliptic longitude-latitude space (blue diamonds). The size of the diamonds corresponds to the total field of view of each image. The positions of numbered Trojans and non-Trojans during the time of our observations with apparent sky motions in the range $14 \leq |v| < 22''/\mathrm{hr}$ are indicated by black squares and red dots, respectively. The solid, dashed, and dotted curves denote respectively the approximate 50%, 10%, and 5% relative density contours in the sky-projected L4 Trojan distribution (Szabó et al. 2007). 40

3.2 Distribution of apparent RA and Dec velocities for numbered Trojans (black squares) and non-Trojans (red dots) with positions in the range $130^\circ \leq \lambda < 190^\circ$ and $-8^\circ \leq \beta < 8^\circ$. The dotted curves denote the $|v| = 14''/\mathrm{hr}$ and $|v| = 22''/\mathrm{hr}$ contours, which separate the Trojans from the majority of non-Trojan minor bodies. 42

3.3 Map of Trojan fraction γ among numbered minor bodies at various locations in the space of ecliptic longitude, ecliptic latitude, and apparent sky motion during the time of our observations. Regions in dark red have 0% predicted contamination by non-Trojans, and our operational Trojan data set includes only objects detected in observed fields located within these regions. 43

3.4 Seeing of the worst image (highest seeing) in every chip for each set of four exposures in the 147 observed fields, plotted as a function of the first exposure time. The dotted line indicates the cutoff at $1.2''$ seeing – objects in fields with higher seeing (red triangles) are not included in the filtered Trojan set. 46

3.5 Comparison of the measured standard deviation error in the difference of g magnitudes, $\sigma_{\Delta g}$, binned in 0.5 mag intervals (blue squares) with the corresponding values from our empirical model combining the measured photometric magnitude errors with a constant contribution from asteroid rotation (green squares). The binned medians of the photometric errors only are denoted by black crosses. The agreement between the measured and modeled $\sigma_{\Delta g}$ values shows that the assumption of a magnitude-invariant contribution to the dispersion in Δg from asteroid rotation is good. 47

3.6 Cumulative absolute magnitude distribution of the filtered Trojan set from our Subaru observations, binned by 0.1 mag (green dots). The best-fit broken power law curve describing the distribution is overplotted (solid black line), with the power law slopes indicated. The dashed line is an extension of the $\alpha_1 = 0.45$ slope and is included to make the slope rollover more discernible. 50

3.7 Cumulative magnitude distribution of all L4 Trojans contained in the Minor Planet Center (MPC) catalog brighter than $H = 12.3$ (white squares; corrected for incompleteness in the range $H = 11.3 - 12.3$ following the methodology of Wong et al. 2014) and the cumulative magnitude distribution of the filtered Trojan set from our Subaru observations, approximately scaled to reflect the true overall number and binned by 0.1 mag (green dots). The error bars on the scaled Subaru Trojan magnitude distribution (in green) denote the 95% confidence bounds derived from scaling the Poisson errors on the Subaru survey data. The uncertainties on the corrected MPC catalog Trojan magnitude distribution in the range $H = 11.3 - 12.3$ are much smaller than the points. The best-fit broken power law curves describing the MPC and Subaru data are overplotted (solid black and dashed red lines, respectively), with the power law slopes (in the text: α_0', α_1', α_1, and α_2) indicated for their corresponding magnitude regions. 51

3.8 Cumulative magnitude distribution of the less-red and red L4 Trojan populations, as constructed using the methods of Wong et al. (2014) for objects in the Minor Planet Center catalog through $H = 12.3$ (cyan triangles and red squares, respectively). These distributions have been scaled to correct for catalog and categorization incompleteness; the error bars denote the 95% confidence bounds and are derived from the binomial distribution errors associated with correcting for uncategorized less-red and red Trojans, as well as the uncertainties from the catalog incompleteness correction in the range $H = 11.3 - 12.3$. The best-fit curves describing the distributions are overplotted (solid blue and red lines, respectively), with the power law slopes indicated for their corresponding magnitude regions. 53

3.9 Histogram of the $g - i$ color distribution for Trojans contained in the SDSS-MOC4 catalog brighter than $H = 12.3$ (green) and fainter Trojans detected in our Subaru survey (blue). There is clear bimodality in the distribution of brighter objects in the SDSS-MOC4 catalog, while the distribution of faint Trojan colors does not display a clear bimodality. This is likely due to the large relative uncertainties associated with the measurement of faint Trojan colors due to asteroid rotation. 55

3.10 Mean $g - i$ colors and corresponding uncertainties for the combined set of Trojans detected in our Subaru survey and L4 Trojans listed in SDSS-MOC4 (blue squares with error bars). Red dots denote the predicted mean $g - i$ color values computed from extrapolation of the best-fit less-red and red population magnitude distributions, assuming mean less-red and red colors of 0.73 and 0.86, respectively. The mean less-red and red $g - i$ colors are indicated by dashed green lines. The monotonic decrease in mean $g - i$ color indicates an increasing fraction of less-red Trojans with decreasing size. The agreement between the extrapolated values and the measured ones suggests that the best-fit color-magnitude distributions derived from bright catalogued Trojans likely extend throughout the magnitude range studied by our Subaru survey. 56

3.11 Comparison between the results from the best test run of our collisional simulation (dotted lines) and the observed L4 Trojan magnitude distributions (solid lines). The initial total magnitude distribution for the best test run is a broken power law with $\alpha_1 = 0.91$, $\alpha_2^* = 0.44$, $H_0 = 7.22$, $H_b = 8.46$, an initial R-to-LR number ratio $k = 5.5$ and a strength normalization factor $c = 1.0$. Black, red, and blue colors indicate the magnitude distribution of the total, red, and less-red populations, respectively. The consistency of the model results and the best-fit distributions demonstrates that the proposed conversion of R objects to LR fragments upon collision is capable of explaining the different shapes of the LR and R magnitude distributions. 61

3.12 Comparison of the best-fit cumulative magnitude distribution curve from the survey data (solid line) with the final predicted distribution from two collisional simulation runs: (1) test run assuming bodies with collisional strength given by Equation (3.7) (dashed line) and (2) test run assuming strengthless bodies with collisional strength scaling given by Equation (3.8) (dot-dash line). The better agreement of the latter suggests that Trojans have very low material strength, similar to comets. 62

4.1 Histograms of the measured spectral slope values of small KBOs (top panel), Centaurs (middle panel), and Trojans (bottom panel). The small KBO and Centaur color distributions include only objects fainter than $H = 7$ and spectral slope uncertainties smaller than the bin size. Cold classical KBOs have been filtered out by omitting all KBOs with inclinations less than 5°. Color bimodalities are evident in all three minor body populations; they are labeled with their corresponding relative colors: less-red (LR), red (R), and very red (VR). 71

4.2 Sublimation lines in the early Solar System, as a function of formation distance. Objects located to the left of a line have the respective volatile ice species depleted from a 100 m layer at the surface after the corresponding elapsed time on the y-axis, while objects located to the right of a line have retained the respective volatile ice species on the surface. The approximate location of the pre-instability primordial planetesimal disk is depicted by the green band. Notably, the H_2S sublimation line (in red) passes through the region of the primordial disk. 77

4.3 Pictoral representation of the hypothesis presented in this paper and the major predictions thereof. Panel a depicts the initial state of bodies within a primordial planetesimal disk extending from 15 AU to roughly 30 AU at the moment when the nebular gas dispersed and the objects were first exposed to sunlight. Each body was composed of a pristine mix of rocky material and ices; volatile ice sublimation began. Panel b illustrates the development of the primordial R and VR colors: Objects that formed inside of the H_2S sublimation line were depleted in H_2S after ~100 Myr and formed a dark, reddish irradiation crust (due primarily to retained methanol). Meanwhile, objects that formed farther out beyond the H_2S sublimation line retained H_2S on their surfaces and thus developed a much redder coloration. The emplacement of Trojans and KBOs during the Nice model dynamical instability is denoted in panel c. We expect that the primordial R and VR objects became R and VR KBOs and Centaurs, respectively, while the Trojans experienced surface color evolution, maintaining the initial color bimodality but resulting in relatively less red colors. Panel d describes the result of collisions in the current Trojan and KBO populations: The surfaces of Trojan collisional fragments of Trojans become depleted in all volatile ice species, thereby becoming LR objects. Although no observational evidence exists at present, we propose that the collisional fragments of small KBOs likely retain H_2S on their surfaces, eventually developing into VR objects. 79

5.1 Distribution of the 3801 objects in our Hilda dataset, plotted in the space of semi-major axis (a), eccentricity (e), and inclination (i). Objects belonging to the Hilda and Schubart collisional families are denoted by magenta and yellow dots, respectively; background Hildas are denoted by blue dots. 90

5.2 Cumulative absolute magnitude distributions of the total Hilda population (white), as well as the Hilda and Schubart collisional families individually (magenta and yellow, respectively). The best-fit power law curves describing the distributions are overplotted (dashed green lines). 91

5.3 Top panel: the overall spectral slope distribution of Hildas, as derived from SDSS-MOC4 photometry, demonstrating a robust color bimodality that divides the population into less-red and red objects. Bottom panel: the spectral slope distributions for Hilda and Schubart family members, as well as background non-family members. Note that the background color distribution is bimodal, while the individual collisional family color distributions are both unimodal. 93

5.4 The cumulative magnitude distributions of the LR and R sub-populations, where objects (including family members) have been categorized into the sub-populations by spectral slope. The distributions are statistically distinct from each other at the 98% confidence level. Both distributions have a characteristically wavy shape that is not consistent with a single or double power law curve. 95

5.5 Comparison of the Hilda and Trojan color distributions, with family members removed. For Hildas, all objects brighter than $H = 14$ are shown, while for Trojans, all objects brighter than $H = 12.3$ are shown; these are the established completeness limits of the corresponding analyses (see Wong et al. 2014 for the discussion of Trojans). Both distributions show a clear bifurcation in color, corresponding to the LR and R sub-populations present in both populations, with comparable mean colors. The R-to-LR number ratio in both Hilda and Trojan background populations are also similar. . . . 96

5.6 Comparison of the total cumulative magnitude distributions of Hildas (black dots) and Trojans (blue squares). The Trojan distribution has been corrected for incompleteness, following the methods of Wong et al. (2014). The Hilda magnitude distribution is notably shallower throughout the entire magnitude range of the data. 99

6.1 Locations of the 52 Subaru Hyper Suprime-Cam fields observed as part of our two-night Kuiper Belt color survey (blue points). The position of the ecliptic on each night is indicated by the solid black line. The number of objects detected in each field is given by the number above the corresponding point. The shaded ellipse shown in the lower right corner of each panel represents the field of view of each exposure, to scale. 109

6.2 Distribution of heliocentric distance for the 372 asteroids detected in our survey. Objects with heliocentric distances greater than 30 AU are classified as KBOs, while the closer-in objects are Centaurs. The typical uncertainty of our heliocentric distance estimates is 3.5 AU. . 110

6.3 Histogram of $g - i$ colors for hot KBOs detected in our survey: the unfilled graph shows the distribution of all 136 objects in the dataset, while the filled graph shows the distribution of only the 118 objects with color uncertainties $\sigma_{g-i} \leq 0.15$. A robust bimodality is evident in both distributions, dividing the objects into two sub-populations — red (R) and very red (VR). The vertical dashed lines indicate the computed mean colors of the R and VR sub-populations — $\overline{(g-i)}_R = 0.91$ and $\overline{(g-i)}_{VR} = 1.42$. 113

6.4 Absolute H magnitude distributions of the total survey hot KBO dataset (black points), as well as the categorized R and VR sub-populations (magenta squares and red triangles, respectively). The error bar in the lower right represents the typical magnitude uncertainty: 0.2 mag. The two color-magnitude distributions have very similar shapes throughout the entire magnitude range. The dashed green line indicates the best-fit power law distribution to the total magnitude distribution through $H_{\max} = 7.5$, which has a power law slope of $\alpha = 1.45$. 115

6.5 Top panel: spectral slope distribution of 200 hot KBOs, incorporating objects in the filtered KBO dataset from our survey as well as objects contained in the Peixinho et al. (2015) database spanning the same magnitude range. Bottom panel: same as top panel, but for 53 Centaurs detected by our survey or listed in the Peixinho et al. (2015) database (with $H \geq 7$). All of these spectral slope values have uncertainties less than 10×10^{-5} Å^{-1}. Both spectral slope distributions are bimodal, with the R and VR modes in each population located at similar spectral slope values. 118

6.6 Color-magnitude plot for hot KBOs and Centaurs combining data tabulated in Peixinho et al. (2015) (dots) and the results of our Subaru survey (squares). Only spectral slope measurements with uncertainties less than 10×10^{-5} Å^{-1} are included; error bars on data points are omitted for the sake of clarity, with the size of the maximum uncertainty indicated by the example error bar in the upper right. Bimodality in color is discernible among all objects fainter than $H \sim 7$. The horizontal dashed line indicates the approximate boundary between R and VR colors. Meanwhile, the larger hot KBOs display a uniform color distribution, with the exception of a small clustering of neutral colored objects in the range $H = 2 - 6$ that is dominated by Haumea collisional family members. 120

7.1 Average of spectra in the LR and R Hilda sub-populations, normalized to unity at 2.2 μm. The two spectra are averages of 12 and 14 individual object spectra, respectively. Gray bars mark regions of strong telluric water vapor absorption. The two sub-populations are distinguished primarily by the difference in spectral slope at shorter near-infrared wavelengths ($\lambda < 1.5$). The error bars shown here and in subsequent figures are the uncertainties on the individual reflectance values derived from the weighted average of individual object spectra. 135

7.2 Comparison of combined visible and near-infrared average spectra of LR (top) and R (bottom) Hildas and Trojans. The absolute reflectivity level at 0.55 μm for each spectrum is set by the published visible albedos: 0.04 for Hildas (Ryan & Woodward 2011) and 0.041 for Trojans (Fernández et al. 2009). Average $u - g - r - i - z$ broadband reflectances for objects in our spectral sample with SDSS-MOC photometry are overplotted. R Hildas and Trojans have largely identical spectra. On the other hand, LR Hildas are systematically bluer in the visible and redder in the near-infrared than LR Trojans, suggesting the presence of a broad, shallow absorption feature between 0.5 and 1.0 μm. 137

7.3 Two-color plot derived from the near-infrared spectra of Hildas (colored points) and Trojans (black points). Hildas that are classified as less-red (LR) and red (R) via visible color and/or infrared reflectivity are denoted by blue and red, respectively; unclassifed objects are marked in yellow. The Hilda near-infrared color distribution lacks the robust bimodality evident in the Trojan data. Nevertheless, LR and R Hildas occupy distinct regions in color space, implying systematically different surface properties and allowing us to classify an additional 4 objects into the LR and R sub-populations. 139

8.1 Continuum subtracted average laboratory spectra of the experimental ice samples with or without the inclusion of H_2S ice in the near-ultraviolet and blue optical wavelength region. Notably, the no sulfur spectrum shows a relatively narrow absorption feature centered at around 230 nm, which is absent in the spectrum with sulfur. 151

8.2 Average normalized reflectance spectra of LR and R Trojans (from Brown 2016). The 3.1 μm absorption feature is prominently seen in the LR spectrum. The broadband reflectance data are derived from Wide-field Infrared Survey Explorer data (Grav et al. 2012). Both spectra indicate the presence of a major absorption feature in the 4–5 μm region. 152

LIST OF TABLES

Number *Page*

7.1 Observation Details 132

7.2 Near-infrared Color Indices and Sub-population Classifications . . . 134

Chapter 1

INTRODUCTION

Understanding the formation and evolution of the Solar System is one of the central objectives of modern astronomy. Over the past century, researchers have utilized the burgeoning body of observations to inform increasingly complex theories of planet accretion and migration. The overarching goal of these endeavors is to synthesize a self-consistent narrative describing the initial conditions of the protoplanetary disk, as well as the various physical and chemical processes that govern planet formation and the subsequent evolution of the Solar System to its current state.

The so-called classical paradigm of solar system formation – the solar nebular disk model – was developed throughout the second half of the 20th century, although the hypothesis of a nebular origin for the protoplanetary disk can be traced back to the 18th century. In short, the solar nebular disk model outlines the initial formation of the protoplanetary disk from the gravitational collapse of a portion of a much larger molecular cloud, perhaps triggered by nearby supernovae in a dense star-forming region (see, for example, Montmerle et al. 2006 and references therein). Subsequent coagulation of dust grains into sub-kilometer sized clumps, followed by pairwise collision-driven hierarchical growth into larger gravitationally-bound planetesimals of tens of kilometers in size, resulted in the formation of planetary-mass embryos throughout the protoplanetary disk. In the inner disk, temperatures were too high to allow for volatile molecules like water and methane to condense, limiting the possible growth of these embryos. Meanwhile, beyond the frost line, the abundance of solid-phase volatile material enabled the rapid formation of much larger embryos, which eventually attained sufficient mass to capture the hydrogen and helium from the surrounding disk into a gaseous envelope and become the giant planets.

Within the standard model, the eight planets in the Solar System formed within the protoplanetary disk near their current heliocentric distances; after the remaining gas and dust in the protoplanetary disk were cleared away by the young Sun's solar wind, which occurred within roughly 10 Myr after the formation of the disk, the orbital architecture of the Solar System did not undergo any significant further alterations. In recent decades, however, this particular portion of the classical paradigm has come under increasing scrutiny, as persistent unresolved problems and surprising

new observations have called into question the idea of a quiescent evolution of the Solar System following the era of planet formation.

Uranus and Neptune currently inhabit a region where the reduced density of the protoplanetary disk and the longer orbital times would have made their formation via hierarchical accretion highly implausible, suggesting that they may have formed closer in to the Sun, nearer to the present-day orbits of Jupiter and Saturn, before migrating outward. The higher-than-expected eccentricities and inclinations of the outer planets likewise point toward a period of planetary migration that transpired sometime after the dispersal of the protoplanetary disk, which would have otherwise damped the eccentricities and inclinations to near zero. The discovery and characterization of the irregular satellites of the gas giants, whose orbital and surface properties preclude an *in situ* formation, as well as the dynamically-excited, yet relatively low-mass Kuiper Belt, further add to the growing list of observations that indicate that significant alterations in solar system architecture likely occurred after the end of planet formation.

In the past few decades, the rapid maturation of the field of exoplanet studies has uncovered a rich diversity of exoplanetary system architectures, many of which bear little resemblance to our Solar System. It has become evident that planetary migration might not only be the key to resolving many of the mysteries of the Solar System, but may also be an important and ubiquitous process that figures prominently in the general evolution of planetary systems throughout the galaxy.

Current models of solar system evolution (e.g., Morbidelli et al. 2005; Gomes et al. 2006; Tsiganis et al. 2005) seek to account for the deficiencies in the classical paradigm of *in situ* formation by positing a scenario in which the giant planets were originally situated in a much more compact orbital configuration. The precise spacings of the outer planets vary across different iterations of the model, but most scenarios describe a system immediately after the dispersal of the protoplanetary disk in which the outermost planet lay within ~20 AU (e.g., Levison et al. 2008a; Levison et al. 2008b). A large, dense reservoir of icy planetesimals with a combined mass of some tens of Earth masses – leftover material from the era of planet formation – extended beyond the outermost giant planet in a wide disk. Close encounters between the outermost gas giant and planetesimals within this primordial disk led to a cascade of scattering events, during which the planetesimals were flung inward by each planet until they encountered Jupiter and were perturbed onto highly-eccentric or hyperbolic orbits. Each scattering encounter exchanged angular momentum

between the planetesimal and the larger planet, with the result being a gradual outward migration of all the gas giants, with the exception of Jupiter, which moved slightly inward.

It is hypothesized that an eventual mean motion resonance crossing between Jupiter and Saturn set off a period of major dynamical restructuring throughout the middle and outer Solar System. The resonance crossing shifted Saturn outward, which subsequently led to mutual gravitational encounters between Saturn and the ice giants. Afterwards, the arrangement of the giant planets altered dramatically as the ice giants were excited onto eccentric orbits that plowed into the primordial planetesimal disk. The disruption of the planetesimals removed more than 99% of the total mass within the primordial outer solar system disk, thereby explaining the current absence of a dense trans-Neptunian minor body population. Eventually, dynamical friction between the outer planets and the remaining planetesimals damped down the eccentricities of the ice giants to their present-day values, bringing an end to the period of dynamical instability.

Dynamical instability models of solar system evolution have undergone several modifications and refinements since their inception. Some of the more recent models propose a sudden stepwise resonance crossing of Jupiter and Saturn via interactions with an ice giant, which prevents the excessive excitation of the Main Asteroid Belt due to sweeping secular resonances that would occur in the case of a smooth migration toward the mean motion resonance (e.g., Brasser et al. 2009; Nesvorný et al. 2013). Other iterations of these models strive to more precisely reproduce the dynamical structure of the present-day Kuiper Belt by including additional ice giants that are eventually ejected from the Solar System (e.g., Nesvorný & Morbidelli 2012). Nevertheless, numerical simulations of dynamical instability scenarios invariably show that the majority of the initial planetesimal disk was ejected from the Solar System (e.g., Roig & Nesvorný 2015). Of the remaining bodies, some were scattered outward to become the current Kuiper Belt, while others were scattered inward to be captured as irregular satellites or into resonant orbits by Jupiter. The latter group of objects became the present-day Jupiter Trojans and Hilda asteroids, which occupy the 1:1 and 3:2 mean motion resonances with Jupiter, respectively.

The major prediction of dynamical instability models, therefore, is that the Trojans, Hildas, and Kuiper Belt objects (KBOs) originated from a single primordial population of minor bodies in the outer Solar System and should share similar properties.

These three asteroid populations provide windows into the earliest epochs of the Solar System and contain a wealth of information regarding the chemical composition and dynamical processes within the protoplanetary disk, extending from the giant planet region out to the farthest reaches of the young Solar System. An in-depth comparison of their properties serves as perhaps the only available robust empirical test of dynamical instability models. However, due to their greater distance, these minor body populations have not garnered the same level of detailed observational analysis as the more accessible Main Belt. The recent advent of new models of solar system evolution has thrust these asteroids into the forefront of planetary science, and their importance in furthering our understanding of solar system history has become more widely recognized.

Over the last four-and-a-half years, I have embarked on a systematic study of the observable properties of Trojans, Hildas, and KBOs. The results of my analyses represent a significant leap in our knowledge of these hitherto poorly-understood minor bodies. These studies are fundamentally motivated as part of a concerted effort to verify the predictions of current dynamical instability models of solar system evolution, with the specific objective of evaluating the similarities and differences between the characteristics of the various populations in the context of their hypothesized common origin in the outer Solar System.

My multifaceted comparative approach has combined novel analyses of archival data from major surveys and earlier targeted studies with new observations utilizing some of the most advanced telescopes currently in operation. Via coordinated consideration of photometry, spectroscopy, and size distributions, my research has brought us closer to understanding the surface composition of these enigmatic objects and tied the populations together within the broader narrative of solar system evolution. Guided by the results of previous published studies of Trojans and Hildas, I have focused on exploring the color bimodality evident in both populations through the lens of formulating a hypothesis to explain their origin, with special attention given to examining the effect of collisions. I have also extended our knowledge of the color and size distributions of Trojans and KBOs through major photometric surveys, including, notably, the robust confirmation of a color bimodality among small KBOs. My latest near-infrared spectra of Hildas have provided a crucial point of comparison with analogous data collected for Trojans, elucidating general similarities as well as curious discrepancies that likely underscore secondary processing of the surfaces of these objects and further constrain their surface chemistry. My endeavors have

yielded the first detailed compositional model of these primordial planetesimals within the framework of the dynamical instability scenario of solar system evolution, which outlines their formation location, the development of color bimodality, and the alterations that have occurred following emplacement into their current locations throughout the middle and outer Solar System.

This thesis represents the culmination of my graduate study probing the relationships between Trojans, Hildas, and KBOs and overviews all the major results of my research as presented in their peer-reviewed, published forms. The detailed analyses of the color and size distribution of Trojans and Hildas are described in Chapters 2 and 5, respectively. The results of my wide-field photometric surveys of small Trojans and KBOs are presented in Chapters 3 and 6, respectively. Chapter 4 explains the hypothesis for the color bimodality evident in all three minor body populations and outlines the major implications of the model for future experimental and observational study. Chapter 7 summarizes the analysis of near-infrared spectra of Hilda asteroids and compares them to corresponding spectra for Trojans. Finally, in Chapter 8, the full body of research is brought together and evaluated alongside the predictions from dynamical instability models of solar system evolution. I also discuss potential fruitful avenues for future follow-up study.

References

Brasser, R., Morbidelli, A., Gomes, R., Tsiganis, K., & Levison, H. F. (2009). "Constructing the secular architecture of the solar system II: the terrestrial planets". *A&A*, 507, 1053.

Gomes, R., Levison, H. F., Tsiganis, K., & Morbidelli, A. (2006). "Origin of the cataclysmic Late Heavy Bombardment period of the terrestrial planets". *A&A*, 455, 725.

Levison, H. F., Bottke, W., Gounelle, M., et al. (2008a). "Chaotic capture of planetesimals into regular regions of the Solar System. II. Embedding comets in the asteroid belt". In: *AAS/Division of Dynamical Astronomy Meeting 39 #12.05*.

Levison, H. F., Morbidelli, A., Van Laerhoven, C., & Gomes, R. (2008b). "Origin of the structure of the Kuiper belt during a dynamical instability in the orbits of Uranus and Neptune". *Icarus*, 196, 258.

Montmerle, T., Augereau, J.-C., Chaussidon, M., & Gounelle, M. (2006). "From Suns to Life: A Chronological Approach to the History of Life on Earth 3. Solar System Formation and Early Evolution: the First 100 Million Years". *Earth, Moon, and Planets*, 98, 39.

Morbidelli, A., Levison, H. F., Tsiganis, K., & Gomes, R. (2005). "Chaotic capture of Jupiter's Trojan asteroids in the early Solar System". *Nature*, 435, 462.

Nesvorný, D. & Morbidelli, A. (2012). "Statistical study of the early Solar System's instability with four, five, and six giant planets". *AJ*, 144, 117.

Nesvorný, D., Vokrouhlický, D., & Morbidelli, A. (2013). "Capture of Trojans by jumping Jupiter". *ApJ*, 768, 45.

Roig, F. & Nesvorný, D. (2015). "The evolution of asteroids in the jumping-Jupiter migration model". *AJ*, 150, 186.

Tsiganis, K., Gomes, R., Morbidelli, A., & Levison, H. F. (2005). "Origin of the orbital architecture of the giant planets of the Solar System". *Nature*, 435, 459.

Chapter 2

THE DIFFERING MAGNITUDE DISTRIBUTIONS OF THE TWO JUPITER TROJAN COLOR POPULATIONS

Wong, I., Brown, M. E., & Emery, J. P. (2014). "The differing magnitude distributions of the two Jupiter Trojan color populations". *AJ*, 148, 112.

ABSTRACT

The Jupiter Trojans are a significant population of minor bodies in the middle Solar System that have garnered substantial interest in recent years. Several spectroscopic studies of these objects have revealed notable bimodalities with respect to near-infrared spectra, infrared albedo, and color, which suggest the existence of two distinct groups among the Trojan population. In this paper, we analyze the magnitude distributions of these two groups, which we refer to as the red and less-red color populations. By compiling spectral and photometric data from several previous works, we show that the observed bimodalities are self-consistent and categorize 221 of the 842 Trojans with absolute magnitudes in the range $H < 12.3$ into the two color populations. We demonstrate that the magnitude distributions of the two color populations are distinct to a high confidence level ($> 95\%$) and fit them individually to a broken power law, with special attention given to evaluating and correcting for incompleteness in the Trojan catalog as well as incompleteness in our categorization of objects. A comparison of the best-fit curves shows that the faint-end power-law slopes are markedly different for the two color populations, which indicates that the red and less-red Trojans likely formed in different locations. We propose a few hypotheses for the origin and evolution of the Trojan population based on the analyzed data.

2.1 Introduction

The Jupiter Trojans are a collection of asteroids that lie in a 1:1 mean motion resonance with Jupiter and are confined to two extended swarms centered about the L_4 and L_5 Lagrangian points, which lead and trail the planet's motion by an angular distance of ~60 degrees. Since the first such asteroid was discovered more

than a century ago, thousands of Trojans have been confirmed, and the current catalog contains over 6000 objects ranging in size from 624 Hektor, with a diameter of roughly 200 km, to subkilometer-sized objects. Estimates of the total number of Trojans larger than 1 km in diameter range from $\sim 1.0 \times 10^5$ (Nakamura & Yoshida 2008) to $\sim 2.5 \times 10^5$ (Szabó et al. 2007), corresponding to a bulk mass of approximately 10^{-4} Earth masses. These values are comparable with those calculated for main belt asteroids of similar size, making the Trojans a significant population of minor bodies located in the middle Solar System. The orbits of Trojans librate around the stable Lagrangian points with periods on the order of a hundred years and are stable over the age of the Solar System, although long-timescale dynamical interactions with the other outer planets decrease the regions of stability and lead to a gradual diffusion of objects from the Trojan swarms (Levison et al. 1997). Escaped Trojans may serve as an important source of short-period comets and Centaurs, a few of which may have Earth-crossing orbits (Marzari et al. 1997).

Due to their peculiar location and dynamical properties, Trojans lie at the intersection of several of the most important topics in planetary science. The origin and evolution of this population have been a subject of particular interest in recent decades. Early theories proposed a scenario in which the Trojans formed at the same heliocentric distance as Jupiter. In this model, Trojans were created out of the body of planetesimals and dust in the primordial solar nebula that remained after the runaway mass accretion phase of Jupiter and were subsequently stabilized into their current orbits around the Lagrangian points (Marzari & Scholl 1998). However, it has been shown that such *in situ* formation at 5.2 AU cannot explain the presently observed total mass and broad orbital inclination distribution. A recent theory, known as the Nice model, suggests a more complex picture in which the Trojan population originated in a region beyond the primordial orbit of Neptune, and the orbits of Jupiter and Saturn were initially situated much closer to the Sun than they are now (Tsiganis et al. 2005). Through interactions with neighboring planetesimals and perhaps an encounter with a large Neptune-sized body (Nesvorný & Morbidelli 2012), the gas giants underwent a rapid migration, crossing resonances and setting off a period of chaotic dynamical alterations in the outer Solar System. It is hypothesized that during this time, the primordial trans-Neptunian planetesimals were disrupted, and a fraction of them were scattered inwards and captured by Jupiter as Trojan asteroids, while the remaining objects were thrown outwards to larger heliocentric distances and eventually formed the Kuiper Belt (Morbidelli et al. 2005).

The current understanding of the composition of Trojan asteroids remains incomplete. Visible spectroscopy has shown largely featureless spectra with spectral slopes ranging from neutral to moderately red (e.g., Dotto et al. 2006; Fornasier et al. 2007; Melita et al. 2008). Spectroscopic studies of Trojans have also been carried out in the near-infrared, a region which contains absorption bands of materials prevalent in other minor body populations throughout the Solar System, such as hydrous and anhydrous silicates, organics, and water ice (e.g., Emery & Brown 2003; Dotto et al. 2006; Yang & Jewitt 2007; Emery et al. 2011). These spectra were likewise found to be featureless and did not reveal any incontrovertible absorption signals to within noise levels. As such, models of the composition and surface properties of Trojans remain poorly constrained. However, several authors have noted bimodality in the distribution of various spectral properties: Bimodality in spectral slope has been detected in both the visible (Szabó et al. 2007; Roig et al. 2008; Melita et al. 2008) and the near-infrared (Emery et al. 2011). The infrared albedo of Trojans has also been shown to display bimodal behavior (Grav et al. 2012). These observations indicate that the Trojans may be composed of two separate sub-populations that categorically differ in their spectroscopic properties.

While future spectroscopic study promises to improve our knowledge of Trojan composition and structure, a study of the size distribution, or as a proxy, the magnitude distribution, may offer significant insight into the nature of the Trojan population. The magnitude distribution preserves information about the primordial environment in which the Trojans were accreted as well as the processes that have shaped the population since its formation, and can be used to test models of the origin and evolution of the Trojans. In particular, an analysis of the distribution of the attested sub-populations may further our understanding of how these sub-populations arose and how they have changed over time. In this paper, we use published photometric and spectroscopic data to categorize Trojans into two sub-populations and compare their individual magnitude distributions. When constructing the data samples, we evaluate and correct for incompleteness to better model the true Trojan population. In addition to fitting the magnitude distributions and examining their behavior, we explore various interpretations of the data.

2.2 Trojan data

Several sources were consulted in compiling the Trojan data samples analyzed in this work. They are described in the following.

Selection of Trojan data samples

The primary data set contains Trojan asteroids listed by the Minor Planet Center (MPC),[1] which maintains a compilation of all currently confirmed Trojans. The resulting data set, referred to in the following as the *main sample*, contains 6037 Trojans. Of these, 3985 are from the L_4 swarm and 2052 are from the L_5 swarm, corresponding to a leading-to-trailing number ratio of 1.95. This significant number asymmetry between the two swarms has been widely noted in the literature and appears to be a real effect that is not attributable to any major selection bias from Trojan surveys, at least in the bright end of the asteroid catalog (Szabó et al. 2007). The brightest object in the main sample has an absolute magnitude of 7.2, while the faintest object has an absolute magnitude of 18.4. The vast majority of Trojans in the main sample (4856 objects) have $H \geq 12.5$, with most of these faint asteroids having been discovered within the last 5 years. In the literature, estimates of the threshold magnitude below which the current total Trojan asteroid catalog is complete lie within the range $H \sim 10.5 - 12$. Therefore, it is only possible to adequately analyze the magnitude distribution of faint Trojans if appropriate scaling techniques are invoked to correct for sample incompleteness. These techniques are discussed in Section 2.3.

Another data set used in this work consists of observations from the fourth release of the Moving Object Catalog of the Sloan Digital Sky Survey (SDSS-MOC4). The SDSS-MOC4 contains photometric measurements of more than 470,000 moving objects from 519 observing runs obtained prior to March 2007. Of these objects, 557 have been identified to be known Trojans listed in the ASTORB file (243 from L_4 and 314 from L_5), and will be referred to in the following as the *Sloan sample*. This data sample includes measured flux densities in the *u, g, r, i, z* bands, centered at 3540, 4770, 6230, 7630, and 9130 Å, respectively, and with bandwidths of $\sim$ 100 Å. As discussed in detail by Szabó et al. (2007), the distribution of the positions of SDSS observing fields through June 2005 in a coordinate system centered on Jupiter indicates that both L_4 and L_5 Trojan swarms were well-covered (i.e., the positions of the observing fields cover a wide range of orbital eccentricity and relative longitude values consistent with Trojan asteroids). Those authors identified 313 known Trojans in the SDSS-MOC3 (previous release) and determined that the survey detected all known Trojans within the coverage area brighter than $H = 12.3$. Observing runs since then have expanded the coverage of the sky to include new

[1] `www.minorplanetcenter.org` (Accessed 2014 May 10)

Trojan swarm regions, yielding 244 additional known Trojans. It is expected that the detection threshold of the Sloan survey (i.e., magnitude to which the SDSS has detected all Trojans within its observing fields) in these newly-covered regions is similar to that determined for the previously-covered regions, and therefore, we may consider our Sloan sample to be a reliable subset of the total Trojan population up to $H \sim 12.3$. This means that the detection threshold of the Sloan sample lies at least 1 mag fainter than the completeness limit of the main sample mentioned above. As part of the analysis presented in the next section, we will confirm the detection threshold of the Sloan sample and use it to arrive at a better estimate of the completeness of the main sample.

Categorizing Trojans

Recent observational studies have identified bimodality in the Trojan population with respect to various photometric and spectroscopic quantities. In this work, we used three earlier analyses of Trojans to classify objects into two color populations.

In Emery et al. (2011), near-infrared (0.7-2.5 μm) spectra of 58 Trojans were collected during four observing runs at the NASA Infrared Telescope Facility and were combined with previously-published spectra of 10 other Trojans. Together, these objects range in magnitude from $H = 7.2$ to $H = 10.7$. For each object, the authors measured the reflectance fluxes in four bands, centered at 0.85, 1.22 (J-band), 1.63 (H-band), and 2.19 (K-band) μm, from which color indices were calculated using $m_{\lambda 1} - m_{\lambda 2} = 2.5 \log(R_{\lambda 2}/R_{\lambda 1})$, where $m_{\lambda 1} - m_{\lambda 2}$ is the color index for two wavelengths, and $R_{\lambda 2}/R_{\lambda 1}$ is the ratio between the corresponding reflectance fluxes. These color indices quantify the spectral slopes of the Trojans in the near-infrared, with higher index values corresponding to redder spectra. Notably, the plot of the J-K color index versus the 0.85-J color index for the asteroids analyzed is not continuous; rather, there is a distinct break separating a redder group (Group I) from a less-red group (Group II). The distribution of the 0.85-H color index likewise shows a clear bimodality, while the H-K histogram is unimodal, suggesting that the difference between the two groups of asteroids is concentrated primarily in the short-wavelength end of the near-infrared spectrum ($\lambda < 1.5$ μm). Both L_4 and L_5 swarms were shown to display similar bimodal behavior, and it was determined that the two identified groups in the analyzed Trojan sample could not have been drawn from a unimodal distribution to a very high confidence level ($> 99.99\%$). We included the color indices of 15 additional Trojans (Emery et al., in prep.) for a total of 83 objects, which we categorized into Group I (19 objects) and Group II

(64 objects).

Grav et al. (2012) presented thermal model fits for 478 Trojans observed with the Wide-field Infrared Survey Explorer (WISE), which conducted a full-sky survey in four infrared wavelengths: 3.4, 4.6, 12, and 22 μm (denoted W1, W2, W3, and W4, respectively). Using the survey data, the W1 albedo was computed for each object, and it was shown that the distribution of the W1 albedos as a function of diameter is discernibly bimodal for the 66 objects with diameters larger than ~60 km, which corresponds to objects brighter than $H \sim 9.6$; for the smaller (fainter) Trojans, the errors in the measured albedos are much larger, and a clear bimodality would not be able to be discerned. Among these 66 large Trojans, 51 have W1 albedo values between 0.11 and 0.18 (Group A), while 15 have W1 albedo values between 0.05 and 0.10 (Group B). Within each group, the albedo values show no dependence on diameter and are tightly clustered, with average separations between adjacent albedo values of 0.001 and 0.004 for Group A and Group B, respectively. Most importantly, when considering the Trojans that are in both the Grav et al. (2012) and the Emery et al. (2011) data sets, one finds that every object in Group A is a member of Group I, and every object in Group B is a member of Group II, with the sole exception of 1404 Ajax, which has high H-K and 0.85-J color indices characteristic of redder Group I objects, but a relatively low W1 albedo value of 0.085. This correspondence between groups categorized with respect to different spectroscopic quantities reinforces the proposal presented by Emery et al. (2011) that the Trojans are composed of two distinct populations with dissimilar spectral properties and likely different compositions. In particular, we conclude that Group I and Group A are both sampled from one of the two Trojan populations; these objects have redder color indices, and we will refer to this population as the red (R) population. Analogously, Group II and Group B are both sampled from the second Trojan population, which will be referred to as the less-red (LR) population, due to the relatively lower near-infrared color indices of its members.

Using the robust and consistent bimodalities observed by Emery et al. (2011) and Grav et al. (2012), we categorized 93 Trojans as either LR (20 objects) or R (73 objects). However, these population sizes are too small to allow for statistically meaningful statements about the overall Trojan population. Moreover, the faintest object in this group has an absolute magnitude of $H = 10.7$, which would restrict our analysis of the Trojan color populations to just the relatively bright objects. In order to expand our categorization of Trojans into color populations, we turned to

photometric data from the Sloan survey.

Roig et al. (2008) studied 250 known Trojans from the SDSS-MOC3 and computed spectral slopes from the listed *u, g, r, i, z* band flux densities. The authors noted that the distribution of spectral slopes is bimodal. We expanded on this study, reproducing the spectral slope calculations and including new Trojans listed in the SDSS-MOC4. Following the procedure used in Roig et al. (2008), we corrected the flux densities using the solar colors provided in Ivezić et al. (2001): $c_{u-r} = (u-r) - 1.77$, $c_{g-r} = (g-r) - 0.45$, $c_{r-i} = (r-i) - 0.10$, and $c_{r-z} = (r-z) - 0.14$. The reflectance fluxes (or albedos), F, normalized to 1 in the r band, were defined as: $F_u = 10^{-0.4c_{u-r}}$, $F_g = 10^{-0.4c_{g-r}}$, $F_i = 10^{0.4c_{r-i}}$, and $F_z = 10^{0.4c_{r-z}}$. The relative errors $\Delta F/F$ were estimated using the second-order approach in Roig & Gil-Hutton (2006):

$$\Delta F/F = 0.9210\Delta c(1 + 0.4605\Delta c), \tag{2.1}$$

where the color errors Δc are computed as the root-squared sum of the corresponding magnitude errors, e.g., $\Delta c_{u-r} = \sqrt{(\Delta u)^2 + (\Delta r)^2}$. The error in F_r was estimated using $\Delta c_{r-r} = \sqrt{2}\Delta r$. We discarded all asteroid observations that had a relative error greater than 10% in any of the fluxes besides F_u, which usually has larger errors due to the effects of instrument noise in and around the *u*-band. We also considered only asteroids with magnitudes in the range $H < 12.3$, over which the Sloan survey is expected to have detected all Trojans within its survey area.

The resulting asteroid set contains 254 objects (114 in L_4 and 140 in L_5), 24 of which were included in the Emery et al. (2011) and/or Grav et al. (2012) analyses and previously categorized by spectrum. For each object, the spectral slope S was computed from a linear least-squares fit to a straight line passing through the fluxes F_g, F_r, F_i, and F_z, taking into account the individual errors ΔF (F_u was not used in this computation, as per Roig et al. 2008). If an object had multiple observations, the average of the spectral slopes computed for all observations was used. The histogram of spectral slopes is shown in Figure 2.1. From the plot, the bimodality in the spectral slope distribution is evident.[2] By fitting the spectral slope distribution with two Gaussians, we found that one of the two modes is centered at $S = 5.3 \times 10^{-5}$ Å^{-1}, while the other mode is located at higher spectral slopes (i.e., redder colors), with a peak at $S = 9.6 \times 10^{-5}$ Å^{-1}; the best-fit Gaussian distribution functions are plotted in Figure 2.1. This two-peaked distribution shape

[2]In Roig et al. (2008), it was reported that only objects in the L4 swarm showed this bimodality in spectral slope. Our present analysis includes many more asteroids from the SDSS-MOC4, and we observe bimodality in both L4 and L5 swarms.

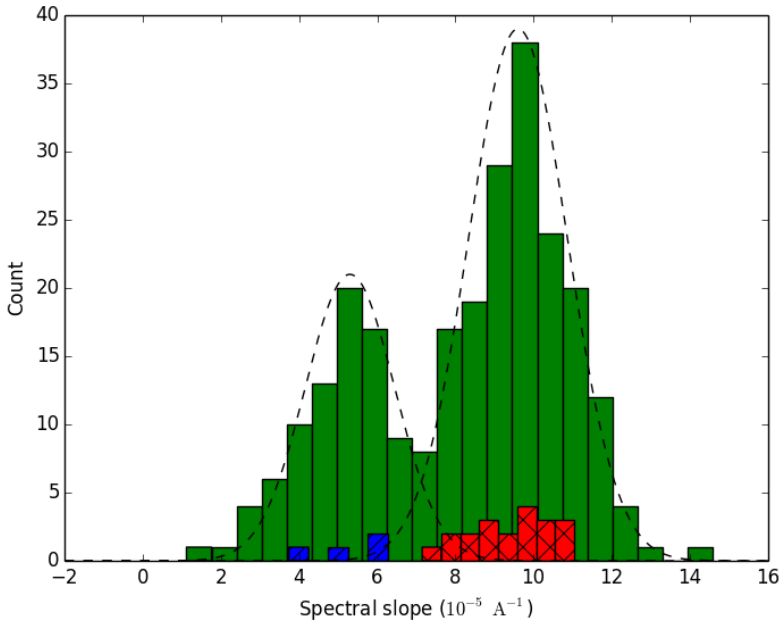

Figure 2.1: Distribution of spectral slopes of all 254 Trojans in the Sloan sample with $H < 12.3$ (solid green), and the distributions of spectral slopes of 24 Trojans classified into the LR and R populations per Emery et al. (2011) and Grav et al. (2012) (blue with diagonal hatching and red with cross hatching, respectively). The best-fit Gaussian distribution functions for the two color populations are shown as black dashed lines.

is similar to the one presented by Emery et al. (2011) for the $H - K$ color index. In particular, the 24 Trojans in the Sloan sample that have already been categorized into LR and R populations (4 in LR and 20 in R) align with the two modes shown in Figure 2.1. Therefore, we can say that objects with spectral slope values consistent with the left mode belong to the LR population, while objects with spectral slope values consistent with the right mode belong to the R population. There is some overlap between the two modes, which makes it difficult to categorize all of the Trojans observed by the SDSS into populations. Nevertheless, we may expand our categorization by adopting conservative break-off spectral slope values: All Trojans with $S \leq 5.3 \times 10^{-5}$ Å^{-1} were classified as less-red, while all Trojans with $S \geq 9.6 \times 10^{-5}$ Å^{-1} were classified as red. Using this method, we were able to categorize 151 of the 254 asteroids in the SDSS-MOC4 with $H < 12.3$; 47 objects belong to the LR population, and 104 objects belong to the R population, with the remaining 103 objects being uncategorized.

The estimated 95% detection flux density thresholds for the *u, g, r, i, z* bands are 22.0, 22.2, 22.2, 21.3, and 20.5, respectively (Ivezić et al. 2001). The average relative band magnitudes for the 151 Trojans in the color populations that were imaged by the SDSS are $u - r = 2.08$, $g - r = 0.62$, $i - r = -0.26$, $z - r = -0.42$ for R objects and $u - r = 2.01$, $g - r = 0.52$, $i - r = -0.18$, $z - r = -0.26$ for LR objects. For an object to be listed on the Moving Object Catalog, it must have detections in at least three bands. The detection threshold in the *z*- and *i*-bands are the lowest. For objects with the same *r*-band magnitude, LR objects are less reflective at longer wavelengths, so for objects with magnitudes near the detection thresholds, there is a bias against LR objects. However, the differences between the relative band magnitudes among the two color populations are not large, and this bias is only expected to affect the objects with absolute magnitudes at the very faint end of our considered range and beyond. Therefore, for our data samples, this effect is minor and is not taken into consideration in our analysis.

We have compared three photometric and spectroscopic studies of Trojans and determined that the bimodal behaviors observed in all these studies are consistent and indicative of the existence of two separate color populations. Of the 842 objects in the main sample with $H < 12.3$, 478 are in the L_4 swarm, and 364 are in the L_5 swarm, which entails a leading-to-trailing number ratio of 1.31. This ratio is notably smaller than the value of 1.93 obtained for the total Trojan catalog, which suggests that there may be major detection biases favoring L_4 Trojans among the faintest objects. After categorizing the objects in the main sample, we found that 64 objects belong to the LR population, and 157 objects belong to the R population, while the remaining 621 objects were not categorized because they have either not been analyzed by any of the three studies discussed above or have spectral slope values between 5.3×10^{-5} Å^{-1} and 9.6×10^{-5} Å^{-1}. In Figure 2.2, the cumulative magnitude distribution $N(H)$, i.e., the total number of asteroids with absolute magnitude less than or equal to H, is plotted for the main sample and the two color populations. The distributions plotted here have not been scaled to correct for incompleteness.

2.3 Analysis

In this section, the magnitude distributions of the Trojan populations are studied. We present best-fit curves to describe the magnitude distributions and compare their behavior.

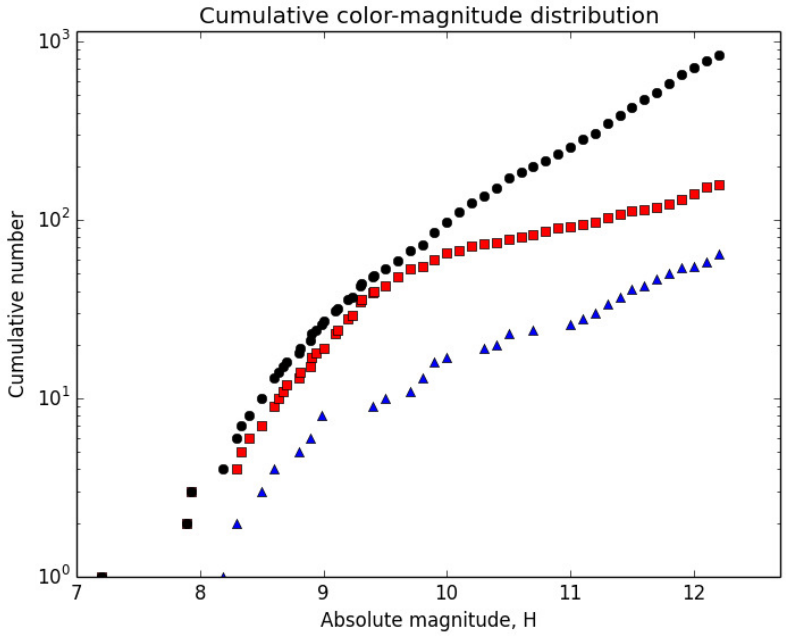

Figure 2.2: Plot of the unscaled cumulative magnitude distributions for the main Trojan sample (black circles) and the categorized R and LR color populations (red squares and blue triangles, respectively). These data have not yet been corrected for incompleteness.

Population distinctness

Previously, we classified Trojans into LR and R populations based on various spectroscopic quantities. While the observed bimodalies indicate that the two populations differ categorically with respect to several spectral properties, the current lack of understanding of Trojan surface composition makes it difficult to use these spectral properties in studying the origin and evolution of Trojans. Moreover, the distinction in spectroscopic properties does not preclude the possibility that the Trojans are simply a mixed population of LR and R objects, with a constant number ratio between the two populations at each magnitude. To determine whether the two color populations are distinct, we must compare the shape of their distributions.

While the LR and R populations are incomplete, there is no reason to believe that one of the two populations is significantly more complete than the other. In particular, the ratio of R to LR objects at each magnitude is not expected to be affected by any major bias (see below for details of our analysis of sample completeness). Since the difference in shape of two magnitude distributions is determined largely by the variation of the number ratio of the two distributions with respect to magnitude, we

may test for population distinctness of the Trojan color samples by using the current LR and R populations as plotted in Figure 2.2, without the need to scale up both populations to correct for incompleteness.

Already from the unscaled cumulative magnitude distributions plotted in Figure 2.2, one can see that the distributions of the color populations are dissimilar. To analytically examine the distinctness of the LR and R populations, we used the two-sample Kuiper variant of the Kolmogorov-Smirnov test (Kuiper-KS test; Press et al. 2007). This nonparametric statistic quantifies the likelihood that two data samples are drawn from the same underlying distribution. It evaluates the sum of the maximum distances of one distribution above and below the other and returns a test decision value, p, between 0 and 1, which represents the probability that the two data samples are not drawn from the same underlying distribution. The Kuiper-KS test is sensitive to differences in both the relative location and the shape of the two cumulative distributions. It is particularly appropriate when dealing with distributions that differ primarily in their tails, as is the case with the Trojan color populations.

Running the Kuiper-KS test on the two color populations, we obtained a p-value of 0.973. This high test decision value demonstrates that the two color populations are not sampled from a single underlying distribution to a confidence level of 97.3%. In other words, the LR and R Trojan populations are distinct not only with respect to the spectral properties of their members, but also with respect to their overall size/magnitude distributions.

Sample completeness

When analyzing a population distribution, it is important to determine and properly correct for any incompleteness in the data sample. To ensure that our curve-fitting adequately models the true Trojan magnitude distribution, we used the Sloan sample to estimate the incompleteness of the main sample and color populations.

As discussed in Section 2.2, the detection threshold of the SDSS within its coverage area is much fainter than the completeness threshold of the overall Trojan catalog. The Sloan survey broadly sampled the orbital parameter space characteristic of both Trojan swarms. Important to our analysis is whether there exists any variation in the magnitude distribution of objects across different regions of the Trojan swarms, since such variation would lead to the total magnitude distribution of the Sloan sample being significantly different from the true total magnitude distribution. Recent studies of Trojans have not observed any discernible correlation between absolute

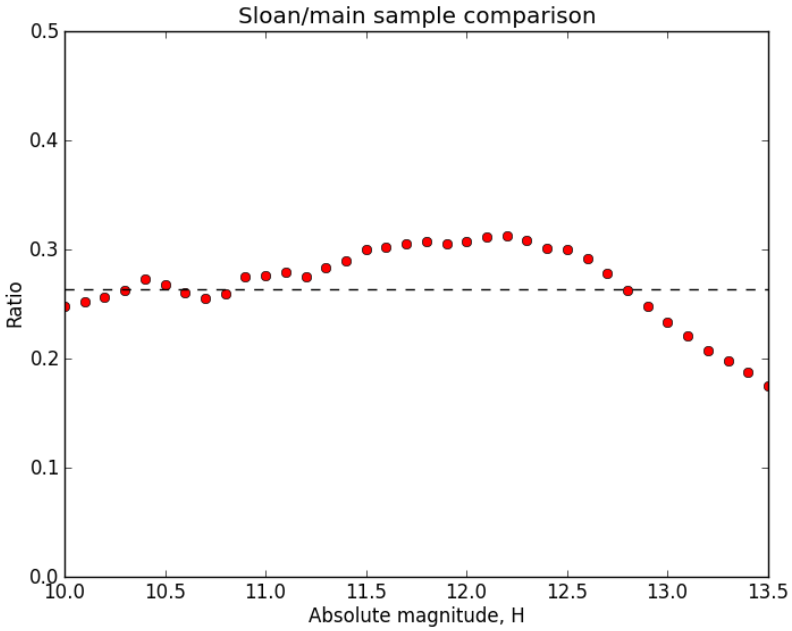

Figure 2.3: Plot of the ratio between the cumulative number of objects in the Sloan sample and the cumulative number of objects in the main sample for various absolute magnitude bins (red circles). The black dashed line indicates the average value R_* for bins with $H = 10.0 \rightarrow 11.2$.

magnitude and eccentricity or inclination in either the leading or the trailing swarm (c.f., Szabó et al. 2007; Fernández et al. 2009), so it is unlikely that the Sloan sample is characterized by any bias with respect to magnitude. We may therefore consider the Sloan sample to be an accurate scaled-down representation of the overall Trojan population. With the exception of a few bright Trojans, all objects in the data samples have absolute magnitudes given with tenth-place accuracy (e.g., $H = 10.1$); in other words, they are effectively binned into 0.1-mag groups. To evaluate the completeness of our main sample, we examine the ratio R between the cumulative number of objects in the Sloan sample and the cumulative number of objects in the main sample for each 0.1-mag bin. In the interval of magnitudes for which both the main sample and the Sloan sample are complete, R should be roughly constant at some value. As the magnitude increases up to the detection threshold of the Sloan sample, the main sample becomes incomplete and R should increase steadily. At higher magnitudes, past the detection threshold of the Sloan sample, R is expected to decrease, since a large number of faint Trojans have been discovered since the release of SDSS-MOC4.

Figure 2.3 shows the values of R plotted with absolute magnitude. From the plot, the expected behavior described earlier is evident: for bins with $H < 11.3$, the value of R is roughly constant at $R_* = 0.264$, which is the average of R for bins with $H = 10.0 \rightarrow 11.2$. (Bright objects were omitted from the average, since the small bin numbers lead to significant scatter in R.) At fainter magnitudes, R increases until $H = 12.3$, after which it decreases rapidly. From this, we conclude that every Trojan brighter than $H = 11.3$ is contained in the main sample (that is, the total Trojan catalog), while the Sloan sample is complete up to $H = 12.3$ (that is, contains an unbiased subsample of Trojans), which confirms the completeness limit estimate given in Szabó et al. (2007). Using the calculated values of R, we can now evaluate the catalog efficiency η_{mpc} of the main sample, i.e., the ratio of the number of Trojans n_{mpc} currently cataloged by the Minor Planet Center to the true number of Trojans n_0, in each bin with $H < 12.3$. For $H < 11.3$, the main sample is complete, so $\eta_{\mathrm{mpc}} = 1$. For $11.3 \leq H < 12.3$, we first evaluate the ratio $r(H)$ between the non-cumulative (i.e., differential or bin-only) number of Trojans in the Sloan and main samples for each 0.1-mag bin; the values of $r(H)$ in this interval are greater than the benchmark value of $r_* = \bar{r} = 0.29$, where $\bar{r}$ is the average of $r(H)$ over the interval $H = 10.0 \rightarrow 11.2$. The catalog efficiency value for each bin is given by $r(*)/r_H$. We subsequently fit a fifth-order polynomial through the binned catalog efficiency values over the domain $11.3 \leq H < 12.3$ to arrive at a smooth functional form $\eta_1(H)$. The catalog efficiency can be expressed as a single piecewise-defined function:

$$\eta_{\mathrm{mpc}}(H) = \begin{cases} 1, & \text{for } H < 11.3 \\ \eta_1(H), & \text{for } 11.3 \leq H < 12.3 \end{cases} . \tag{2.2}$$

More careful consideration must be made when correcting for incompleteness in the color populations. While the absolute magnitude distribution of Trojans does not appear be dependent on the location in orbital parameter space and would not be affected by the particular locations of observed fields within the Trojan swarms, as discussed earlier, correlations between the color of objects and orbital parameters may lead to biases in the resulting magnitude distributions of the color populations. Most Trojans (621 out of 842) were not categorized as either less-red or red, with the brightest unclassified asteroid having $H = 9.6$. The majority of objects in our color populations (152 out of 221) were classified using the spectral slope categorization method based off Sloan data. Using data from the SDSS-MOC3, Szabó et al. (2007) and Roig et al. (2008) reported a weak correlation between spectral slope and

inclination, with objects at larger inclinations tending to be redder; Fornasier et al. (2007) reported a similar correlation in their study of visible spectral slope and interpreted it as a lack of faint objects with low spectral slope. This color-inclination correlation was found to be the same in both swarms. Szabó et al. (2007) identified a bias in their data: the L_5 subsample of Trojans had a significantly larger fraction of objects with high inclinations than the L_4 subsample. In our analysis, such asymmetric coverage would cause the number ratio of R-to-LR L_5 Trojans to be unrealistically inflated and skew the overall color distributions.

To determine whether a similar bias is present among the 254 objects in the current Sloan sample, we computed the fraction of objects in the SDSS-MOC4 with large inclinations ($i > 20°$) for the leading and trailing swarms independently. It was found that the fraction is similar for the two swarms (0.24 for L_4 and 0.22 for L_5). This means that observing runs since the release of SDSS-MOC3 have captured more high-inclination regions of the L_4 swarm, and as a result, the leading and trailing swarms are equally well-sampled in the SDSS-MOC4 data. Therefore, no selection bias with respect to inclination is discernible in the Sloan sample, and we may consider the LR and R color populations defined in Section 2.2 to be a representative subset of the true color composition of the overall Trojan population. In particular, the number ratio of red to less-red Trojans in each bin should be approximately the same as the true ratio at that magnitude. We define a categorization efficiency value for each bin, which is the ratio between the number of already-categorized Trojans in the LR and R populations, $n_{LR}(H) + n_R(H)$, and the total number of detected Trojans, $n_{\rm det}(H)$. Over the domain $9.6 \leq H < 12.3$, where the color classification is incomplete, we followed a similar procedure to that used in deriving the detection efficiency and fitted a polynomial through the categorization efficiency values to obtain a smooth function $\eta_2(H)$. We can write the overall categorization efficiency function as

$$\eta_{\rm cat}(H) = \begin{cases} 1, & \text{for } H < 9.6 \\ \eta_2(H), & \text{for } 9.6 \leq H < 12.3 \end{cases} . \tag{2.3}$$

This categorization efficiency function is the same for both LR and R populations and must be coupled with the detection efficiency function $\eta_{\rm det}(H)$ for $H \geq 11.3$.

The total efficiency functions for the main sample and color populations, which take into account catalog and/or categorization incompleteness, are given by

$$\eta(H) = \begin{cases} \eta_{\rm mpc}(H), & \text{for the main sample} \\ \eta_{\rm cat}(H) \times \eta_{\rm mpc}(H), & \text{for the LR and R populations} \end{cases} . \tag{2.4}$$

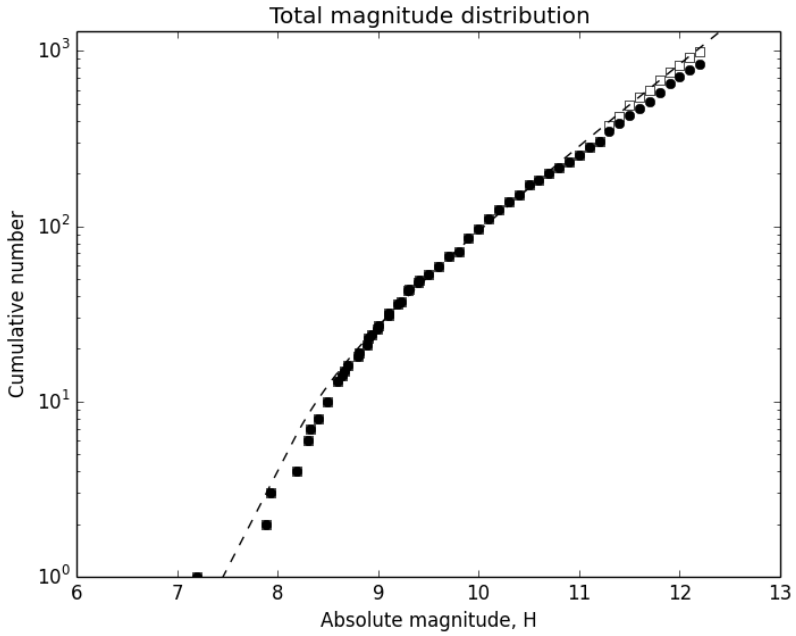

Figure 2.4: Plot depicting the scaled (white squares) and unscaled (black circles) cumulative magnitude distributions for the total Trojan population, along with the best-fit curve describing the true Trojan cumulative distribution.

We used catalog and categorization efficiency to scale up the data samples so that they approximate the true Trojan population. Similar scaling methods have been employed in the study of the size distribution and taxonomy of main belt asteroids (DeMeo & Carry 2013). We demonstrate our method with the following example: At $H = 11.5$, there are 43 objects in the main sample, 17 of which are also contained in the Sloan sample. The ratio between the number of objects in the Sloan and main samples is $r = 17/43 \approx 0.395$, which yields a catalog efficiency value of $\eta = r*/r \approx 0.73$. Thus, the approximate true number of Trojans with $H = 11.5$ is $n_0 = 43/\eta \sim 59$. The scaled and unscaled cumulative magnitude distributions for the main sample and color populations are shown in Figures 2.4-2.6.

Distribution fits

Previous analyses of the magnitude distributions of Trojans (see, for example, Jewitt et al. 2000) have shown that the differential magnitude distribution, $\Sigma(H) = dN(M)/dH$, is well-described by a broken power law with four parameters:

$$\Sigma(\alpha_1, \alpha_2, H_0, H_b|H) = \begin{cases} 10^{\alpha_1(H-H_0)}, & \text{for } H < H_b \\ 10^{\alpha_2 H+(\alpha_1-\alpha_2)H_b-\alpha_1 H_0}, & \text{for } H \geq H_b \end{cases}, \tag{2.5}$$

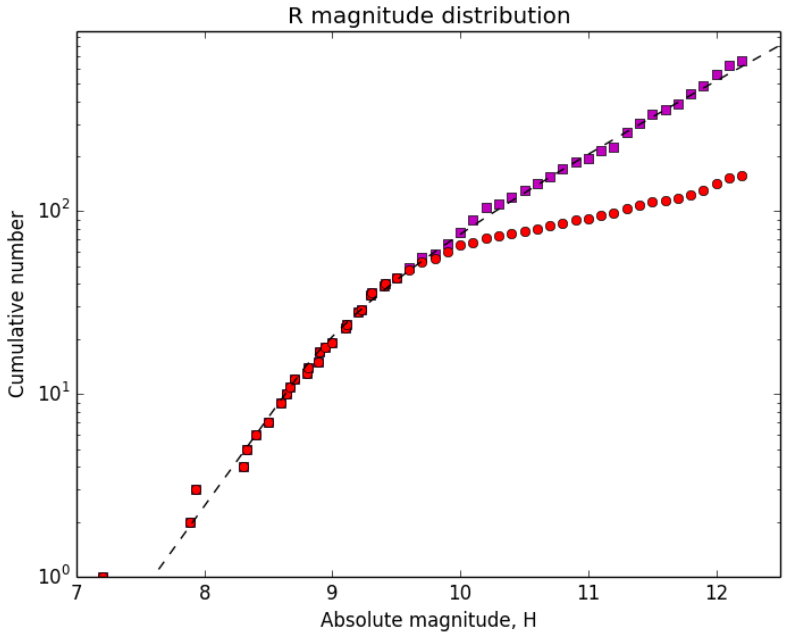

Figure 2.5: Plot depicting the scaled (magenta squares) and unscaled (red circles) cumulative magnitude distributions for R population, along with the best-fit curve describing the true cumulative distribution.

where there is a sudden change from a bright-end slope α_1 to a shallower faint-end slope α_2 at some break magnitude H_b. H_0 is the threshold magnitude for which $\Sigma(H_0) = 1$ and serves to properly normalize the distribution to fit the data. Jewitt et al. (2000) obtained the slope values $\alpha_1 = 1.1$ and $\alpha_2 = 0.4$ from their study of 257 Trojans, which did not correct for incompleteness in the faint-end distribution. More recent studies of faint Trojans by Szabó et al. (2007) and Yoshida & Nakamura (2005) obtained faint-end slope values of 0.44 and 0.38, respectively.

We fitted the magnitude distributions of the total Trojan sample and the two color populations to the broken power law distribution function in Equation (2.5) by using a maximum likelihood method similar to the one used in Fraser et al. (2008) for their study of Kuiper Belt objects. Given a list of Trojan magnitudes and a particular set of parameters for the distribution function to be fitted, this technique defines a likelihood function L, which returns the probability that a random sampling of the distribution will yield the data. The maximum likelihood method is well-suited for analyzing data sets like the ones under consideration, since it is robust to small data counts and non-Gaussian statistics, for which typical χ^2 fitting methods are inappropriate. Also, other statistical considerations like catalog and categorization

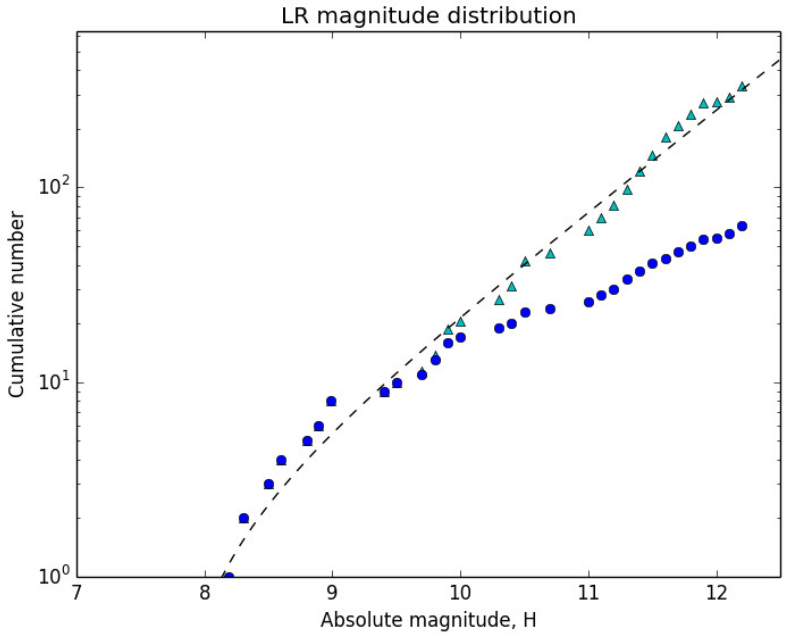

Figure 2.6: Plot depicting the scaled (cyan triangles) and unscaled (blue circles) cumulative magnitude distributions for LR population, along with the best-fit curve describing the true cumulative distribution.

efficiency can be easily integrated into the formulation.

The likelihood function used in our fitting takes the form

$$L(\alpha_1, \alpha_2, H_0, H_b|H_i) \propto e^{-N} \prod_i P_i, \tag{2.6}$$

where H_i is the absolute magnitude of each detected Trojan, N is the total number of detected objects expected in the magnitude range under consideration, and P_i is the probability of having object i with magnitude H_i given the underlying distribution function Σ. Taking into account detection and categorization incompleteness, N is given by

$$N = \int_{-\infty}^{H_{\max}} \eta(H)\Sigma(\alpha_1, \alpha_2, H_0, H_b|H)\, dH, \tag{2.7}$$

where $\eta(H)$ is the efficiency function defined in Equation (2.4), and $H_{max} = 12.3$. By including the efficiency function, we ensure that the curves are fitted to the true Trojan distribution, not the incomplete detected Trojan distribution. The probability P_i is simply the differential density function evaluated at H_i, i.e., $P_i = \Sigma(\alpha_1, \alpha_2, H_0, H_b|H_i)$.

The best-fit distribution functions were obtained by maximizing the likelihood function over the four-dimensional parameter space using an affine-invariant Markov Chain Monte Carlo (MCMC) Ensemble sampler with 100,000 steps (Foreman-Mackey et al. 2013). The optimal parameters and corresponding 1σ errors were computed for each distribution. The magnitude distribution of the main sample (all Trojans with $H < 12.3$) is best-fit by $\alpha_1 = 1.11 \pm 0.20$, $\alpha_2 = 0.46 \pm 0.01$, $H_0 = 7.09^{+0.03}_{-0.02}$, and $H_b = 8.16^{+0.03}_{-0.04}$. The bright-end slope is consistent with the value calculated in Jewitt et al. (2000), while the faint-slope is steeper than previously-obtained values, due to our correction for incompleteness in the Trojan catalog past $H = 11.3$. The L_4 and L_5 Trojans were independently analyzed for detection completeness and fitted in a similar fashion. The optimal values of the slopes α_1 and α_2 for the two swarm distributions were found to be indistinguishable within calculated uncertainties. This agrees with the results of earlier studies (see, for example, Yoshida & Nakamura 2008) and demonstrates that the leading and trailing Trojan swarms have magnitude distributions that are identical in shape, differing only in overall asteroid number.

The magnitude distributions of the color populations were both individually fitted to a broken power law. The optimal parameters for the R population magnitude distribution are $\alpha_1 = 0.97^{+0.05}_{-0.04}$, $\alpha_2 = 0.38 \pm 0.02$, $H_0 = 7.24^{+0.05}_{-0.07}$, and $H_b = 8.70^{+0.08}_{-0.11}$, while for the LR population magnitude distribution, they are $\alpha_1 = 1.25^{+0.09}_{-0.04}$, $\alpha_2 = 0.52^{+0.03}_{-0.01}$, $H_0 = 7.77^{+0.04}_{-0.09}$, and $H_b = 8.15^{+0.06}_{-0.10}$. Figures 2.4-2.6 show the cumulative magnitude distributions for the main sample and the color populations, along with the best-fit curves that describe the true distributions. In each plot, the lower distribution is the cumulative count for the unscaled data set, and the upper distribution is the approximate true distribution, scaled to correct for catalog and/or categorization incompleteness (as described earlier).

2.4 Discussion

The analysis of the Trojan magnitude distributions in the previous section, which utilized the most current asteroid catalog and corrected for catalog incompleteness, presents the most accurate picture to date of the true Trojan population up to the cutoff magnitude $H = 12.3$. Using the distribution fits calculated for both the total and the two color populations, we can try to reach a better understanding of the origin and evolution of the Trojans, and in particular, the nature of the two color populations.

The most notable feature of the magnitude distributions is the transition from a steep power-law slope to a shallower slope at $H \sim 8-9$. Previous studies of the total Trojan magnitude distribution (e.g., Morbidelli et al. 2005) have suggested that the broken power-law shape separates the population into two groups: Objects with magnitudes brighter than the break magnitude are described by a power-law slope that reflects the primordial accretion processes that created the original Trojan population. On the other hand, objects with magnitudes fainter than the break magnitude form a sub-population that has reached collisional equilibrium and is mostly composed of collisional fragments of larger objects. It was demonstrated in pioneering work by Dohnanyi (1969) that the magnitude distribution of a small body population that evolves solely through self-collisions attains an equilibrium power-law slope of $\alpha_* \sim 0.5$ when collisional equilibrium is achieved, regardless of the initial shape of the distribution. The faint-end slope of the total Trojan magnitude distribution that we obtained by fitting the data is $\alpha_2 = 0.46 \pm 0.01$, which is consistent with the canonical collisional equilibrium slope. In relation to the history of the Trojan population, there arises the question of whether the sharp roll-over to a shallower faint-end slope in the currently-observed population is a consequence of collisional evolution after the Trojans were emplaced in their current orbits around Jupiter, or a result of collisional interactions in the primordial trans-Neptunian region prior to emplacement. Several authors have modeled the collisional evolution of Trojans and determined that the observed broken power-law distribution is best reproduced when assuming that a break was present at the time of emplacement (c.f., Marzari et al. 1997; de Elía & Brunini 2007). Furthermore, these studies have shown that the intrinsic collision probabilities characteristic of the Trojan swarms are insufficiently high to have brought about any significant collisional evolution among objects with magnitudes brighter than the break. Thus, the currently-observed bright-end distribution reflects the shape of the primordial size distribution of large Trojans at the time of emplacement.

A more peculiar aspect of the Trojans is the magnitude distributions of the color populations – in particular, the difference between the faint-end slopes of the R and LR populations (0.38 ± 0.02 and $0.52^{+0.03}_{-0.01}$, respectively). The Kuiper-KS test demonstrated that the magnitude distributions of the color populations are remarkably distinct, which indicates that the two populations likely formed in different places before being emplaced into the Trojan regions. While the fitted bright-end slopes are different, the distinction is most apparent in the faint-end portion of the distributions. (Running the Kuiper-KS test on just the bright-end portions of the

color distributions yielded intermediate p-values, which are inconclusive as a metric for population distinctness.) A hypothesis that posits a scenario in which the two color populations arose from different regions in the primordial trans-Neptunian disk would be able to explain the different bright-end slopes, which are determined primarily by the accretion environment. However, in light of the interpretation that the faint-end portion of the broken power-law distributions is a result of collisional evolution, the significant difference between the faint-end slopes poses a challenge. One possible explanation would be that just as different accretion environments can lead to different bright-end slopes, non-uniform collisional dynamics in the primordial trans-Neptunian disk could have resulted in the color populations experiencing different early collisional histories owing to their different formation regions. Various areas of the primordial disk may have been characterized by a wide range of impact velocities and intrinsic collision probabilities. In such a model, the currently-observed discrepancy between the faint-end slopes would be a relic of the pre-emplacement collisional evolution of the two color populations. Indeed, very little is known about the nature of the early Solar System, so one could not exclude this possibility.

That said, the fact that the overall Trojan population is characterized by a faint-end slope so close to the canonical collisional equilibrium slope suggests that perhaps there is another explanation in which the two color populations experienced a similar collisional evolution within the primordial trans-Neptunian disk and were emplaced with similar faint-end slopes. In this case, the different faint-slopes would be explained by positing a mechanism that converts R objects to LR objects, hence flattening the faint-end slope of the R population, while simultaneously steepening the faint-end slope of the LR population.

Previous laboratory work has shown that irradiation of surfaces rich in terrestrial bitumens and other organic compounds, which tend to have a characteristic red color, leads to the flattening of the spectral slope and a resulting less-red color (Moroz et al. 2004; Kaňuchová et al. 2012). However, since the incident radiation flux on the surface of a spherical body scales in tandem with size, this flattening effect is expected to be the same across the full range of Trojan sizes and hence does not explain the discrepant faint-end slopes observed in the magnitude distributions of the color populations. Furthermore, the timescale for flattening the spectrum of a R Trojan is much smaller than the time that has elapsed since emplacement and formation (Melita et al. 2009), so if irradiation is the sole mechanism for converting

R objects to LR ones, one would not expect any R objects to remain. In Melita et al. (2009), an additional mechanism is proposed whereby minor cratering events disrupt the spectrally flattened irradiation crust and excavate underlying material, which the authors of that work posit as being red in color, consistent with that of typical surfaces rich in complex organic materials. The added contribution of cratering leads to irradiated LR objects becoming R objects once again through resurfacing, thereby preventing all the R objects from turning into LR objects. However, the characteristic collisional timescale and, correspondingly, the timescale of resurfacing decrease with decreasing asteroid size, while the rate of irradiation is the same for all objects, as mentioned earlier. Therefore, the resurfacing of Trojans through cratering becomes more effective at returning irradiated LR objects to R objects when one goes to smaller sizes. This would lead to a relative excess of R objects at faint magnitudes, which is the opposite of what is evident in the observed color distributions.

In this work, we suggest an alternative explanation for the discrepancy in faint-end slopes and examine the possibility that the fragments resulting from a catastrophic shattering impact on a red object are less-red. In other words, we hypothesize that R and LR Trojans have more or less identical interiors, differing only in the spectroscopic properties of their outer surfaces, and that the destruction of red objects is the primary mechanism by which red objects become less-red, thereby resulting in a relative depletion of red Trojans in the range of sizes for which shattering collisions have been significant. To assess the viability of this conversion hypothesis, we ran a series of simple numerical simulations that model the collisional evolution of the Trojan population since emplacement. The mechanics of our algorithm are similar to those used in previous studies of Trojan collisions (c.f., Marzari et al. 1997). Earlier works have shown that the overall Trojan-Trojan collisional frequency among large objects with $H > 9$ is very low ($\ll 1$ per Gyr). This means that most of the collisional activity is concentrated in the faint-end of the magnitude range, and that the magnitude distribution of bright objects is expected to remain almost unchanged over the age of the Solar System. Therefore, we only considered initial magnitude distributions that are broken power-laws of the form described in Equation (2.5) with a bright-end distribution identical to that of the currently-observed population ($\alpha_1 = 1.11$, $H_0 = 7.09$, and $H_b = 8.16$). For the initial faint-end slope, we considered values ranging from 0.45 to 0.55, in increments of 0.01. Objects in the initial population with absolute magnitudes in the range $H = 7 \rightarrow 23$ were divided into 50 logarithmic diameter bins using the conversion

formula $D = 1329 \times 10^{-H/5}/\sqrt{p_v}$, where we have assumed a uniform geometric albedo of $p_v = 0.04$ (Fernández et al. 2009).

The initial color populations were constructed by taking constant fractions of the total population across all bins; based on the calculated 0.1-mag bin number ratios between R and LR Trojans in the bright-end portion of our data, we considered initial R-to-LR number ratios, k, ranging from 4 to 5, in increments of 0.5. The collisional evolution was carried out over 4 Gyr in 100000 time steps of length $\Delta t = 40000$. At each time step, the expected number of collisions $N_{\rm coll}$ between bodies belonging to any pair of bins is given by

$$N_{\rm coll} = \frac{1}{4}\langle P \rangle N_{\rm tar} N_{\rm imp} \Delta t (D_{\rm tar} + D_{\rm imp})^2, \tag{2.8}$$

where $N_{\rm tar}$ and $N_{\rm imp}$ are the number of objects in a target bin with diameter $D_{\rm tar}$ and an impactor bin with diameter $D_{\rm imp}$, respectively; $\langle P \rangle = 7.35 \times 10^{-18}$ yr^{-1} km^{-2} is the intrinsic collision probability for Trojan-Trojan collisions and was approximated by the weighted average of the probabilities calculated by Dell'Oro et al. (1998) for L_4 and L_5 Trojans, taking into account the currently-observed number asymmetry between the two swarms. For a target bin with diameter $D_{\rm tar}$, only impactor bins with diameters satisfying the condition $D_{\rm imp} \geq D_{\rm min}$ were considered, where $D_{\rm min}$ is the minimum impactor diameter necessary for a shattering collision and defined as (Bottke et al. 2005)

$$D_{\rm min} = \left(\frac{2Q_D^*}{V_{\rm imp}^2} \right)^{1/3} D_{\rm tar}, \tag{2.9}$$

where $V_{\rm imp} = 4.6$ km s^{-1} is the weighted average of the L_4 and L_5 impact velocities calculated by Dell'Oro et al. (1998), and Q_D^* is the strength of target. In our algorithm, we utilized a size-dependent strength scaling law based off one used by Durda et al. (1998) in their treatment of collisions among small main-belt asteroids:

$$Q_D^* = c \cdot 10 \cdot (155.9 D^{-0.24} + 150.0 D^{0.5} + 0.5 D^{2.0}) \, \mathrm{J\,kg^{-1}}, \tag{2.10}$$

where a parameter c was included to adjust the overall scaling of the strength and varied in increments of 1 from 1-10 in our test trials.

Our model tracked the collisional evolution of the two color populations separately and computed the number of collisions between objects of the same color, as well as collisions involving objects of different colors. For each time step, the number of collisions between all relevant pairs of bins was calculated, and the corresponding target and impactor numbers were subtracted from their respective bins. In all cases,

regardless of the color of the target and/or impactor, the collisional fragments were redistributed into less-red bins, thereby modeling the conversion of red objects to less-red fragments through shattering. After running simulations for all possible values of the parameters (α_2, k, c), we found that a large number of test runs yielded final total and color magnitude distributions that were consistent with the observed distributions analyzed in Section 2.3. To determine which run best reproduced the calculated faint-end slopes, we compared the simulation results directly with the fitted distribution curves. The test run that resulted in the best agreement with the data had an initial total distribution with faint-end slope $\alpha_2 = 0.47$, a strength scaling parameter $c = 6$, and began the collisional time integration with a R-to-LR bin number ratio $k = 4.5$. Plots comparing the final simulated distributions from this test run with the observed data are shown in Figure 2.7.

Although the simulations did not take into account other processes that may have affected the Trojan asteroids (e.g., dynamical dissipation), several conclusions about the evolution of Trojans can be made. First, the similarity between the initial test distributions that yielded good agreement with the data and the present-day total magnitude distribution indicates that collisional evolution has not played a major role in the post-emplacement development of the Trojan population, at least in the magnitude range we have considered in this work. In fact, our simulations are consistent with there being only 1 or 2 major collisions (involving asteroids with $D > 100$ km) in the past 4 Gyr. To date, the only incontrovertible asteroid family that has been detected among the Trojans is the Eurybates family (Brož & Rozehnal 2011), which shows that the currently-observed bright-end distribution is largely identical to the bright-end distribution of the primordial Trojan population at the time of emplacement. Second, the R-to-LR collisional conversion model has yielded simulated final color distributions that match the currently-observed color magnitude distributions well. This model is also supported by photometric data from members of the Eurybates family, all of which have very low spectral slope values that are consistent with LR objects (Fornasier et al. 2007). Thus, the conversion hypothesis offers a feasible explanation for the curious faint-end slope discrepancy between the R and LR populations.

The R-to-LR conversion model assessed here is attractive because it has some basis in recent work on Kuiper Belt objects (KBOs), which, in the Nice model, arise from the same body of material as the Jupiter Trojans. The Kuiper Belt contains several sub-populations, among which are the so-called “red” and “very red” small

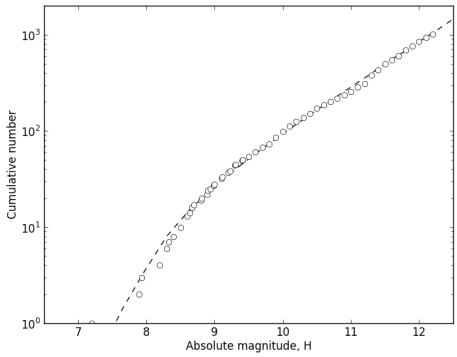

(a) Comparison plot showing the final total distribution generated by the simulation (dashed black line) and the observed total distribution of Trojans, scaled to correct for incompleteness (white circles).

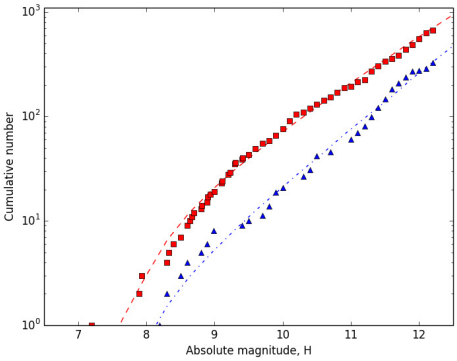

(b) Same as (a), but for the R (red dashed line and squares) and LR (blue dash-dotted line and triangles) color distributions.

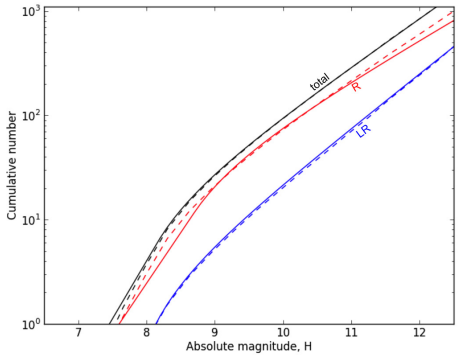

(c) Plot comparing the best-fit distribution curves computed from the observed data (solid lines) with the final distribution curves generated by the simulation (dashed liens) for the total, R, and LR populations.

Figure 2.7: Comparison between the results from the best test run ($\alpha_1 = 1.11$, $\alpha_2 = 0.47$, $H_0 = 7.09$, $H_b = 8.16$, $c = 6$, $k = 4.5$) and the observed Trojan magnitude distributions.

KBOs (Fraser et al. 2008; Peixinho et al. 2012). A recent hypothesis describes a scenario in which KBOs formed in the trans-Neptunian disk at a range of heliocentric distances (Brown et al. 2011). During formation in the primordial disk, all of these objects would have accumulated a mix of rock and volatile ices of roughly cometary composition. After the disk dissipated, the surface ices on these bodies began sublimating from solar radiation, leading to differential sublimation of individual ice species based on the location of the object. Whether a particular volatile ice species on the surface of these objects is retained or sublimates away is dependent on the volatility of the ice species and the temperature of the region where the object resides. As a result, for each ice species, there would have existed some threshold heliocentric distance for which objects at greater heliocentric distances would have retained that ice species on their surfaces, while those that formed closer in would have surfaces that were completely depleted in that ice species. Irradiation of surface ices would lead to significant darkened irradiation mantle, which serves to protect ices embedded deeper down from sublimation and the further action of irradiation. Therefore, the hypothesis in Brown et al. (2011) argues that the presence or absence of one particular volatile ice species may be the key factor in producing the observed bimodality in color among the small KBOs: objects that retained that volatile ice species on their surfaces formed a "very red" irradiation mantle, while those that lost that volatile ice species from their surfaces formed a "red" irradiation mantle.

If the LR and R Jupiter Trojans were drawn from the same two sources as the "red" and "very red" KBOs, any exposed volatile ices on the surface would have evaporated away during the process of emplacement to smaller heliocentric distances. In our hypothesis, we posit that the more intense irradiation at $\sim$ 5 AU flattens the spectral slope of the irradiation mantles that formed prior to emplacement. As a result, the Trojans that formed a "red" irradiation mantle would be left with surfaces that appear relatively less-red, while those that formed at greater heliocentric distances and developed a "very red" irradiation mantle would end up with the relatively redder surfaces characteristic of R Trojans. When a Trojan shatters during a catastrophic impact, the irradiation mantle on the surface would disintegrate and any newly-exposed volatile ices in the interior (including, crucially, the particular species responsible for the formation of the "very red" irradiation mantle) would sublimate away within a relatively short timescale. Thus, if one assumes that LR and R Trojans have similar interior compositions, the fragments resulting from the shattering of a R Trojan would indeed be spectroscopically identical to those that would result from shattering a LR Trojan. Subsequent irradiation of these pristine fragments

would eventually raise the spectral slope slightly, but not to the extent as would result if volatile ices were retained on the surface. As a consequence, in the range of magnitudes for which collisions are significant, shattering events since emplacement would have gradually depleted the number of red Trojans while simultaneously enriching the number of less-red Trojans.

Ultimately, the nature of the Trojans and the source of their bimodal color distribution may involve a complex interplay between several different physical processes. A full understanding of the origin of this color bimodality and the mechanisms that have shaped the Trojan color populations hinges upon better knowledge of the composition and chemistry of these objects, which may be obtained in the future with higher-quality spectroscopic observations.

2.5 Conclusion

In this paper, we have examined the magnitude distributions of the two color populations that make up the Jupiter Trojans. Earlier spectroscopic studies in the visible, near-infrared, and infrared were compared and shown to be consistent with one another, confirming the existence of two separate populations of Trojans whose members differ categorically with respect to various spectral properties. Using primarily the spectral slope values calculated from SDSS-MOC4 photometric data, we were able to categorize 221 Trojans with absolute magnitudes less than 12.3 into the red and less-red color populations. In the process of compiling the data samples and evaluating for catalog and categorization incompleteness, we concluded that the current Trojan catalog is complete to $H = 11.3$, while the Sloan Digital Sky Survey is likely to have detected all Trojans in its coverage area with $H < 12.3$.

Using the Kuiper-KS test, we demonstrated that the two color populations have magnitude distributions that are distinct to a high confidence level. Fitting the distributions to a broken power law, we found that both the bright-end ($\alpha_1^R = 0.97^{+0.05}_{-0.04}$ vs. $\alpha_1^{LR} = 1.25^{+0.09}_{-0.04}$) and the faint-end ($\alpha_2^R = 0.38 \pm 0.02$ vs. $\alpha_2^{LR} = 0.52^{+0.03}_{-0.01}$) power-law slopes are different, with the most evident distinction in the faint-end portion of the magnitude distribution. Meanwhile, the total Trojan magnitude distribution is characterized by power-law slopes that are largely consistent with previously-published values ($\alpha_1 = 1.11 \pm 0.20$ and $\alpha_2 = 0.46 \pm 0.01$). The distinctness of the red and less-red magnitude distributions suggests that the color populations likely formed in different regions of the primordial debris disk. The discrepancy between the faint-end slopes in particular may indicate that the color

populations underwent different collisional evolutions before being emplaced into their current orbits. By running simulations of Trojan self-collisions, we have shown that this discrepancy is also consistent with a scenario in which the red objects differ from the less-red objects only by the presence of a thin outer irradiation crust, and the color populations were emplaced with similar faint-end slopes. Subsequent shattering collisions could have led to the observed divergence of the faint-end slopes as all collisional fragments would be spectroscopically less-red. Future study of Trojan asteroid spectra and composition promises to further our understanding of the origin and evolution of the two color populations.

References

Bottke, W. F., Durda, D. D., Nervorný, D., et al. (2005). "The fossilized size distribution of the main asteroid belt". *Icarus*, 175, 111.

Brown, M. E., Schaller, E. L., & Fraser, W. C. (2011). "A hypothesis for the color diversity of the Kuiper belt". *ApJ*, 739, L60.

Brož, M. & Rozehnal, J. (2011). "Eurybates – the only asteroid family among Trojans?" *Mon. Not. R. Astron. Soc.* 414, 565.

de Elía, G. C. & Brunini, A. (2007). "Collisional and dynamical evolution of the L_4 Trojan asteroids". *A&A*, 475, 375.

Dell'Oro, A., Marzari, F., Paolicchi, P., Dotto, E., & Vanzani, V. (1998). "Trojan collision probability: A statistical approach". *A&A*, 339, 272.

DeMeo, F. E. & Carry, B. (2013). "The taxonomic distribution of asteroids from multi-filter all-sky photometric surveys". *Icarus*, 226, 723.

Dohnanyi, J. S. (1969). "Collisional model of asteroids and their debris". *Journal of Geophysical Research*, 74, 2531.

Dotto, E., Fornasier, S., Barucci, M. A., et al. (2006). "The surface composition of Jupiter Trojans: Visible and near-infrared survey of dynamical families". *Icarus*, 183, 420.

Durda, D. D., Greenberg, R., & Jedicke, R. (1998). "Collisional models and scaling laws: A new interpretation of the shape of the main-belt asteroid size distribution". *Icarus*, 135, 431.

Emery, J. P. & Brown, R. H. (2003). "Constraints on the surface composition of Trojan asteroids from near-infrared (0.8 – 4.0 micron) spectroscopy". *Icarus*, 164, 104.

Emery, J. P., Burr, D. M., & Cruikshank, D. P. (2011). "Near-infrared spectroscopy of Trojan asteroids: Evidence for two compositional groups". *AJ*, 141, 25.

Fernández, Y. R., Jewitt, D., & Ziffer, J. E. (2009). "Albedos of small Jovian Trojans". *AJ*, 138, 240.

Foreman-Mackey, D., Hogg, D. W., Lang, D., & Goodman, J. (2013). "emcee: The MCMC Hammer". *pre-print*. arXiv:1202.3665.

Fornasier, S., Dotto, E., Hainaut, O., et al. (2007). "Visible spectroscopic and photometric survey of Jupiter Trojans: Final results on dynamical families". *Icarus*, 190, 622.

Fraser, W. C., Kavelaars, J. J., Holman, M. J., et al. (2008). "The Kuiper belt luminosity from m_R = 21 to 26". *Icarus*, 195, 827.

Grav, T., Mainzer, A. K., Bauer, J. M., Masiero, J. R., & Nugent, C. R. (2012). "WISE/NEOWISE observations of the Jovian Trojan population: Taxonomy". *ApJ*, 759, 49.

Ivezić, Ž., Tabachnik, S., Rafikoc, R., & al., et (2001). "Solar System Objects Observed in the Sloan Digital Sky Survey Commissioning Data". *AJ*, 122, 2749.

Jewitt, D. C., Trujillo, C. A., & Luu, J. X. (2000). "Population and size distribution of small Jovian Trojan asteroids". *AJ*, 120, 1140.

Kaňuchová, Z., Brunetto, R., Melita, M., & Strazzulla, G. (2012). "Space weathering and the color indexes of minor bodies in the outer Solar System". *Icarus*, 221, 12.

Levison, H. F., Shoemaker, E. M., & Shoemaker, C. S. (1997). "Dynamical evolution of Jupiter's Trojan asteroids". *Nature*, 385, 42.

Marzari, F., Frinella, P., Davis, D. R., Scholl, H., & Campo Bagatin, A. (1997). "Collision evolution of Trojan asteroids". *Icarus*, 125, 39.

Marzari, F. & Scholl, H. (1998). "Capture of Trojans by a growing proto-Jupiter". *Icarus*, 131, 41.

Melita, M. D., Licandro, J., Jones, D. C., & Williams, I. P. (2008). "Physical properties and orbital stability of the Trojan asteroids". *Icarus*, 195, 686.

Melita, M. D., Strazzulla, G., & Bar-Nun, A. (2009). "Collisions, cosmic radiation and the colors of the Trojan asteroids". *Icarus*, 203, 134.

Morbidelli, A., Levison, H. F., Tsiganis, K., & Gomes, R. (2005). "Chaotic capture of Jupiter's Trojan asteroids in the early Solar System". *Nature*, 435, 462.

Moroz, L., Baratta, G., Strazzulla, G., Starukhina, L., & Dotto, E. (2004). "Optical alteration of complex organics induced by ion irradiation: 1. Laboratory experiments suggest unusual space weathering trend". *Icarus*, 170, 214.

Nakamura, T. & Yoshida, F. (2008). "A new surface density model of Jovian Trojans around triangular libration points". *Publ. Astron. Soc. Japan*, 60, 293.

Nesvorný, D. & Morbidelli, A. (2012). "Statistical study of the early Solar System's instability with four, five, and six giant planets". *AJ*, 144, 117.

Peixinho, N., Delsanti, A., Guilbert-Lepoutre, A., Gafeira, R., & Lacerda, P. (2012). "The bimodal colors of Centaurs and small Kuiper Belt objects". *A&A*, 546, A86.

Press, W. H., Teukolsky, S. A., Vetterling, W. T., & P., Flannery B. (2007). *Numerical Recipes: The Art of Scientific Computing*. Cambridge University Press.

Roig, F. & Gil-Hutton, R. (2006). "Selecting candidate V-type asteroids from the analysis of the Sloan Digital Sky Survey colors". *Icarus*, 183, 411.

Roig, F., Ribeiro, A. O., & Gil-Hutton, R. (2008). "Taxonomy of asteroid families among the Jupiter Trojans: comparison between spectroscopic data and the Sloan Digital Sky Survey colors". *A&A*, 483, 911.

Szabó, Gy. M., Ivezić, Ž., Jurić, M., & Lupton, R. (2007). "The properties of Jovian Trojan asteroids listed in SDSS Moving Object Catalogue 3". *Mon. Not. R. Astron. Soc.* 377, 1393.

Tsiganis, K., Gomes, R., Morbidelli, A., & Levison, H. F. (2005). "Origin of the orbital architecture of the giant planets of the Solar System". *Nature*, 435, 459.

Yang, B. & Jewitt, D. (2007). "Spectroscopic search for water ice on Jovian Trojan asteroids". *AJ*, 134, 223.

Yoshida, F. & Nakamura, T. (2005). "Size distribution of faint Jovian L4 Trojan asteroids". *AJ*, 130, 2900.

Yoshida, F. & Nakamura, T. (2008). "A comparative study of size distributions for small L4 and L5 Jovian Trojans". *Publ. Astron. Soc. Japan*, 60, 297.

Chapter 3

THE COLOR-MAGNITUDE DISTRIBUTION OF SMALL JUPITER TROJANS

Wong, I. & Brown, M. E. (2015). "The color-magnitude distribution of small Jupiter Trojans". *AJ*, 150, 174.

ABSTRACT

We present an analysis of survey observations targeting the leading L4 Jupiter Trojan cloud near opposition using the wide-field Suprime-Cam CCD camera on the 8.2 m Subaru Telescope. The survey covered about 38 deg^2 of sky and imaged 147 fields spread across a wide region of the L4 cloud. Each field was imaged in both the g' and the i' band, allowing for the measurement of $g - i$ color. We detected 557 Trojans in the observed fields, ranging in absolute magnitude from $H = 10.0$ to $H = 20.3$. We fit the total magnitude distribution to a broken power law and show that the power-law slope rolls over from 0.45 ± 0.05 to $0.36^{+0.05}_{-0.09}$ at a break magnitude of $H_b = 14.93^{+0.73}_{-0.88}$. Combining the best-fit magnitude distribution of faint objects from our survey with an analysis of the magnitude distribution of bright objects listed in the Minor Planet Center catalog, we obtain the absolute magnitude distribution of Trojans over the entire range from $H = 7.2$ to $H = 16.4$. We show that the $g - i$ color of Trojans decreases with increasing magnitude. In the context of the less-red and red color populations, as classified in Wong et al. (2014) using photometric and spectroscopic data, we demonstrate that the observed trend in color for the faint Trojans is consistent with the expected trend derived from extrapolation of the best-fit color population magnitude distributions for bright catalogued Trojans. This indicates a steady increase in the relative number of less-red objects with decreasing size. Finally, we interpret our results using collisional modeling and propose several hypotheses for the color evolution of the Jupiter Trojan population.

3.1 Introduction

Residing at a mean heliocentric distance of 5.2 AU, the Jupiter Trojans are asteroids that share Jupiter's orbit around the Sun and are grouped into two extended swarms centered around the stable L_4 and L_5 Lagrangian points. Estimates of the size of this population indicate that the Trojans are comparable in number to main belt asteroids of similar size (Szabó et al. 2007; Nakamura & Yoshida 2008). Explaining the origin and evolution of this significant population of minor bodies is crucial for understanding the formation and dynamical history of the Solar System. While early theories posited that the Trojans could have formed out of the body of planetesimals and dust in the immediate vicinity of a growing Jupiter (Marzari & Scholl 1998), later studies revealed that such *in situ* formation is not consistent with the observed total mass and broad inclination distribution. An alternative theory suggests that the Trojans formed at large heliocentric distances out of the same body of material that produced the Kuiper Belt (Morbidelli et al. 2005). Subsequent migration of the gas giants triggered a period of chaotic dynamical alterations in the outer Solar System, during which the primordial trans-Neptunian planetesimals were disrupted (Tsiganis et al. 2005; Nesvorný & Morbidelli 2012). It is hypothesized that a fraction of these objects were scattered inwards and captured by Jupiter as Trojan asteroids.

A detailed study of the size distribution of Trojans promises to shed light on the relationships between the Trojans and other minor body populations in the outer Solar System, and more broadly, constrain models of late solar system evolution. The size distribution, or as a proxy, the magnitude distribution, offers significant insight into the nature of the Trojan population, as it contains information about the conditions in which the objects were formed as well as the processes that have shaped the population since its formation. Previous studies of the Trojan magnitude distribution have largely focused on objects larger than ~10-20 km in diameter (e.g., Jewitt et al. 2000; Szabó et al. 2007), although the advent of larger telescopes and improved instruments has presented the opportunity to carry out surveys of smaller Trojans. Yoshida & Nakamura (2005) and Yoshida & Nakamura (2008) presented the first magnitude distribution for small L4 and L5 Trojans as part of a small survey, with several dozen objects detected down to sizes of ~2 km. The detection of many more faint objects promises to expand our understanding of the small Trojan population.

Little is known about the composition and surface properties of Trojans. Both large-scale and targeted observational studies over the past few decades have revealed a

population that is notably more homogeneous than the main belt asteroids, with low albedos and spectral slopes ranging form neutral to moderately red (e.g., Szabó et al. 2007; Roig et al. 2008; Fernández et al. 2009). Meanwhile, visible and near-infrared spectroscopy has been unable to detect any incontrovertible spectral features (e.g., Dotto et al. 2006; Fornasier et al. 2007; Yang & Jewitt 2007; Melita et al. 2008; Emery et al. 2011). However, recent work has uncovered bimodalities in the distribution of various spectral properties, such as spectral slope in the visible (Szabó et al. 2007; Roig et al. 2008; Melita et al. 2008) and the near-infrared (Emery et al. 2011). In Wong et al. (2014), the data from these previous studies were compiled and shown to be indicative of the existence of two color populations — the so-called red and less-red populations. The magnitude distributions of these two populations are distinct, differing especially in the power-law distribution slopes of objects smaller than ~50 km. Several hypotheses for the origin of this discrepancy have been posited, including different source regions for red and less-red Trojans, conversion of red objects to less-red fragments upon collision, and space weathering effects (Melita et al. 2008; Wong et al. 2014). By extending the analysis of Trojan colors to smaller objects, we hope to better understand the underlying processes behind the color dichotomy and the differing magnitude distributions of the color populations.

In this paper, we present the results of our survey of small Trojans in the leading L4 cloud. We detected over 550 Trojans and measured their brightness in two filters, from which their magnitudes and colors were computed. We calculate the best-fit curve describing the total magnitude distribution down to a limiting absolute magnitude of $H = 16.4$. In addition, we present the first analysis of the color distribution of faint Trojans to date and compare the measured trends with previously-published results for brighter Trojans (Wong et al. 2014). Lastly, we use collisional modeling to interpret the derived magnitude and color distributions.

3.2 Observations

Observations of the L4 Trojan cloud were carried out on UT 2014 February 27 and 28 at the 8.2 m Subaru Telescope situated atop Mauna Kea, Hawaii. Using the Suprime-Cam instrument — a mosaic CCD camera consisting of ten 2048×4096 pixel CCD chips that covers a $34' \times 27'$ field of view with a pixel scale of $0.20''$ (Miyazaki et al. 2002) — we observed 147 fields, corresponding to a total survey area of 37.5 deg^2. To detect moving objects as well as obtain color photometry, we imaged each field four times — twice in the g' filter ($\lambda_{\rm eff} = 480.9$ nm) and twice in the

i' filter ($\lambda_{\rm eff}$ = 770.9 nm). The average time interval between epochs is about 20 minutes for images in the same filter, and about 30 minutes for images in different filters. We chose an exposure time of 60 seconds for all images to optimize survey depth and coverage. The resulting average observational arc for each moving object is roughly 70 minutes.

The on-sky positions of the 147 observed Suprime-Cam fields are shown in Figure 3.1. The surveyed region was divided into blocks of 10 – 12 observing fields, which we imaged in the filter order $g' - g' - i' - i'$, or in reverse. Blocks observed toward the beginning of each night targeted the trailing edge of the L4 Trojan cloud, while blocks observed later in the night are concentrated closer to the peak of the spatial distribution. To place the observed field locations in the context of the L4 point and the spatial extent of the leading Trojan cloud, we use the empirical L4 Trojan number density model from Szabó et al. (2007): $n(\lambda'_J, \beta'_J) \sim \exp\left[-(\lambda'_J - 60^\circ)^2/2\sigma_\lambda^2\right] \times \exp\left[-\beta'^2_J/2\sigma_\beta^2\right]$ with $\sigma_\lambda = 14^\circ$ and $\sigma_\beta = 9^\circ$, where λ'_J and β'_J are respectively the heliocentric ecliptic longitude and latitude relative to Jupiter. In Figure 3.1, the 50%, 10%, and 5% relative number density contours are shown in geocentric longitude-latitude space (λ, β); the position of the L4 point during the time of our observations is at around $(\lambda, \beta) = (170^\circ, 0^\circ)$. We see that the majority of the observed fields lie in regions with predicted Trojan number densities at least 50% of the peak value.

Moving object detection

After bias-subtracting the images, we flat-fielded them using the twilight flats taken at the start of the first night of observation. For every chip image (10 per exposure, 40 per observed field, 5880 for the entire survey), we calculated the astrometric solution by first creating a pixel position catalog of all the bright sources in the image. This was done using Version 2.11 of SExtractor (Bertin & Arnouts 1996), with the threshold for source detection set at a high value (typically 30 or higher, depending on the seeing, in units of the estimated background standard deviation). The source catalog was then passed to Version 1.7.0 of SCAMP (Bertin 2006), which matches objects in the source catalog with those in a reference catalog of stars and computes the astrometric projection parameters for each chip image; we used the 9th Data Release of the Sloan Digital Sky Survey (SDSS DR9) as our reference catalog. In order to assess the quality of the astrometric solution from SCAMP, we compared the corrected on-sky position of stars in each image with the position of matched reference stars and found typical residual RMS values much less than $0.1''$.

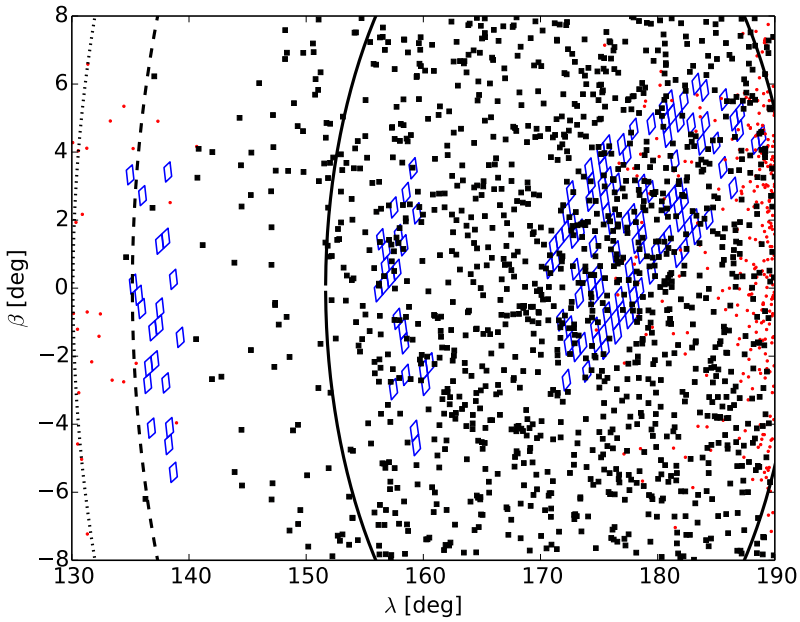

Figure 3.1: Locations of the 147 observed Subaru Suprime-Cam fields, projected in geocentric ecliptic longitude-latitude space (blue diamonds). The size of the diamonds corresponds to the total field of view of each image. The positions of numbered Trojans and non-Trojans during the time of our observations with apparent sky motions in the range $14 \leq |v| < 22''$/hr are indicated by black squares and red dots, respectively. The solid, dashed, and dotted curves denote respectively the approximate 50%, 10%, and 5% relative density contours in the sky-projected L4 Trojan distribution (Szabó et al. 2007).

Likewise, we calculated the position scatter between matched stars from pairs of images taken in the same observing field and found typical RMS values less than $0.05''$.

Next, we passed the distortion-corrected images through SExtractor again, this time setting the detection threshold at 1.2 times the background standard deviation; we also required detected sources to consist of at least two adjacent pixels with pixel values above the detection threshold. These conditions were chosen to minimize the detection of faint non-astrophysical sources in the background noise as well as the loss of possible moving objects of interest. The resulting list contains the right ascension (RA) and declination (Dec) of all detected objects within each image. To search for moving object candidates, we fit orbits through sets of four source positions, one from each of the four images in an observing field, using the methods described in Bernstein et al. (2004). A source was flagged as a moving object

candidate if the resulting χ^2 value from the fit was less than 10. We reduced the number of non-Trojan moving object candidates flagged in this procedure by only considering sets of source positions consistent with apparent sky motion $|v|$ less than $25''$/hr. For comparison, typical sky motions of known Trojans during the time of our observations lie in the range $14 \leq |v| < 22''$/hr.

Each moving object candidate was verified by aligning and blinking 100×100 pixel stamps clipped from each of the four images in the vicinity of the object. We rejected all non-asteroidal moving object candidates (e.g., sets of four sources that were flagged by the previous orbit-fitting procedure, but that included cosmic ray hits and/or anomalous chip artifacts). We also rejected asteroids that passed in front of background stars, coincided with a cosmic ray hit in one or more image, or otherwise traversed regions on the chip that would result in unreliable magnitude measurements. These objects numbered around 10, of which only 2 had on-sky positions and apparent sky motions consistent with Trojans. Therefore, the removal of these objects from our Trojan data set is not expected to have any significant effect on the results of our analysis. Through the procedures described above, we arrived at an initial set of 1149 moving objects.

Selecting Trojans

Observations were taken when the L4 point was near opposition, where the apparent sky motion of an object, $|v|$, is roughly inversely related to the heliocentric distance. Since the short observational arc of ~70 minutes prevented an accurate determination of the heliocentric distance from orbit-fitting, we resorted to using primarily sky motion to distinguish Trojans from Main Belt Asteroids and Hildas. Figure 3.2 shows the distribution of apparent velocities in RA and Dec for all numbered minor bodies as calculated from ephemerides generated by the JPL HORIZONS system for UT 2014 February 27 12:00 (roughly the middle of our first night of observation). We have shown only objects with on-sky positions in the range of our observing fields ($130^\circ \leq \lambda < 190^\circ$ and $-8^\circ \leq \beta < 8^\circ$). A large majority of the objects with $|v| < 20''$/hr are Trojans, while the relative portion of non-Trojan contaminants increases rapidly in the range $20''$/hr] $\leq |v| < 22''$/hr. We made an initial cut in angular velocity to consider only objects in the range $14 \leq |v| < 22''$/hr.

The contamination rate varies across the surveyed area as a function of apparent sky motion, as well as position on the sky. We carried out a more detailed contamination analysis by applying a rough grid in the space of $|v|$, λ, and β spanning the range

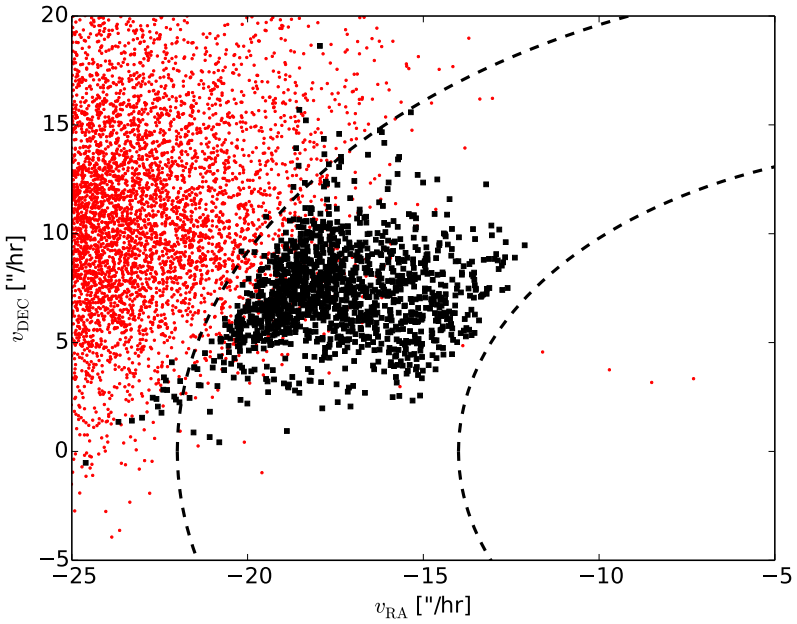

Figure 3.2: Distribution of apparent RA and Dec velocities for numbered Trojans (black squares) and non-Trojans (red dots) with positions in the range $130° \leq \lambda < 190°$ and $-8° \leq \beta < 8°$. The dotted curves denote the $|v| = 14''/\mathrm{hr}$ and $|v| = 22''/\mathrm{hr}$ contours, which separate the Trojans from the majority of non-Trojan minor bodies.

$14 \leq |v| < 22''/\mathrm{hr}$, $130° \leq \lambda < 190°$, and $-8° \leq \beta < 8°$. We then binned all numbered objects contained in the JPL HORIZONS system into this three-parameter space and computed the Trojan fraction $\gamma \equiv$ [numbered Trojans]/[all numbered objects] in each bin. For bins containing no numbered objects, we assigned a value $\gamma = 0$. Figure 3.3 shows the results of this analysis. We note that while the non-Trojan contamination rate over the whole surveyed area among objects with apparent sky motions between 20 and $22''/\mathrm{hr}$ is high, there are regions in the sky where the Trojan fraction is 1. Similarly, for objects with $|v| < 20''/\mathrm{hr}$, there are regions near the edges of the ecliptic longitude space covered by our survey where the non-Trojan contamination rate is very high.

In this paper, our operational Trojan data set includes only those objects detected in regions of the $(\lambda, \beta, |v|)$ space with Trojan fraction $\gamma = 1$ (i.e., zero expected contamination). The resulting data set contains 557 Trojans. Choosing a slightly more lenient Trojan selection criterion (e.g., including objects detected in bins that do not contain numbered objects, where the Trojan fraction is technically unknown) was not found to significantly affect the main results of our magnitude and color

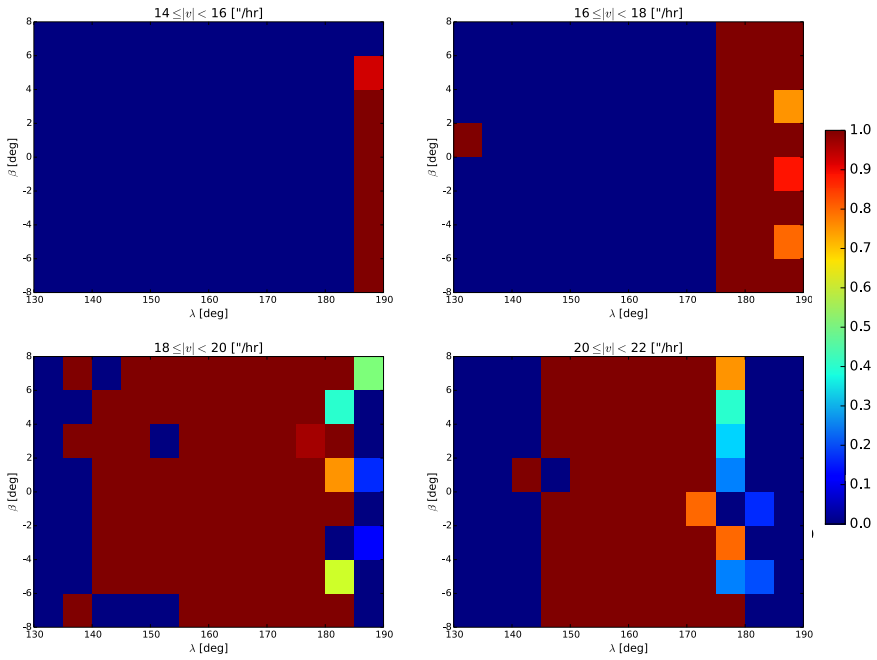

Figure 3.3: Map of Trojan fraction γ among numbered minor bodies at various locations in the space of ecliptic longitude, ecliptic latitude, and apparent sky motion during the time of our observations. Regions in dark red have 0% predicted contamination by non-Trojans, and our operational Trojan data set includes only objects detected in observed fields located within these regions.

distribution analysis.

Photometric calibration

The apparent magnitude m of an object detected in our images is given by $m = m_0 - 2.5\log_{10}(f) = m_0 + m_s$, where f is the measured flux, m_0 is the zero-point magnitude of the corresponding chip image, and the survey magnitude has been defined as $m_s \equiv -2.5\log_{10}(f)$. The flux of each object was calculated by SExtractor through a fixed circular aperture with a diameter of 5 pixels. We computed the zero-point magnitude for each chip image by matching all bright, non-saturated sources detected by SExtractor to reference stars in the SDSS DR9 catalog and fitting a line with slope one through the points (m_s, m). The maximum allowed position difference for a match between image and reference stars was set at $0.5''$, which resulted in an average of ~150 matched stars per chip image. We used Sloan g-band and i-band reference star magnitudes to calibrate images taken in the g' and i' filters of Suprime-Cam, respectively. Consequently, the calculated apparent magnitudes of our detected Trojans are effectively Sloan g and i magnitudes, which greatly

facilitates the comparison of our computed colors with those derived for Trojans in the SDSS Moving Object Catalog (see Section 3.3).

Both the error in the zero-point magnitude σ_0 and the error in the measured flux σ_f (reported by SExtractor) contribute to the error in the apparent magnitude σ, which we calculate using standard error propagation methods: $\sigma = \sqrt{\sigma_0^2 + (2.5(\sigma_f/f)/\ln(10))^2}$. We set the g magnitude of each Trojan detected in our survey to be the error-weighted mean of the apparent magnitudes calculated from the two g' Suprime-Cam images, i.e., $g = \left(\sum_{k=1}^{2} m_{g,k}/\sigma_{g,k}^2\right) / \left(\sum_{k=1}^{2} 1/\sigma_{g,k}^2\right)$, with the corresponding uncertainty in the g magnitude defined by $\sigma_g^2 = 1/\left(\sum_{k=1}^{2} 1/\sigma_{g,k}^2\right)$; the i magnitude and uncertainty of each Trojan were defined analogously.

As mentioned previously, orbit-fitting over the short observational arcs prevented us from precisely determining the orbital parameters of the detected objects. Therefore, we did not directly convert the apparent magnitudes to absolute magnitudes using the best-fit heliocentric distances. Instead, we considered the difference between apparent V-band magnitude and absolute magnitude H of known Trojans, as computed by the JPL HORIZONS system for the time of our observations. By fitting a linear trend through the computed apparent sky motions $|v|$ as a function of the magnitude difference values, we obtained an empirical conversion between the sky motion and $V - H$. Since $V - H$ depends also on the viewing geometry, we divided the ecliptic longitude range $130° \leq \lambda < 190°$ into 5° bins and derived linear fits separately for known Trojans within each bin. We calculated the apparent V-band magnitudes of the detected Trojans from our survey using the empirical mean colors $g - r = 0.55$ and $V - r = 0.25$ reported in Szabó et al. (2007). Then, we translated these V values to H using the measured sky motions and our empirical $V - H$ conversions.

From the absolute magnitude, the diameter of a Trojan can be estimated using the relation $D = 1329 \times 10^{-H/5}/\sqrt{p_v}$, where D is in units of kilometers, and we assumed a uniform geometric albedo of $p_v = 0.04$ (Fernández et al. 2009). The brightest Trojan we detected in our survey has $H = 10.0$, corresponding to a diameter of 66.5 km, while the faintest Trojan has $H = 20.3$, corresponding to a diameter of 0.6 km.

Data completeness

An analysis of the magnitude distribution of a population can be severely affected by detection incompleteness. Varying weather conditions during ground-based surveys lead to significantly different detection completeness limits for observations taken

at different times, resulting in a non-uniform data set and biases in the overall magnitude distribution. Since we required a moving object candidate to be detected in all four images taken in an observed field, the epoch with the highest seeing in each set of four exposures determined the threshold magnitude to which the survey was sensitive in that particular field. Here we set the seeing value of each chip image to be the median of the full-width half-max of the point-spread function for all non-saturated stars, as computed by SExtractor. If the highest seeing value across a four-image set was high, then the object detection pipeline would have missed many of the fainter objects positioned within the field. This is because the signal-to-noise of objects of a given magnitude located on the worst image of the set would be significantly lower than that of the same objects located on an image taken at good seeing. As a result, the magnitude distribution of objects detected in an observing field with high-seeing images would be strongly biased toward brighter objects, and when combined with the full body of data, would affect the overall magnitude distribution.

Figure 3.4 shows the highest measured seeing for each group of four chip images taken in an observing field, plotted with respect to the time of first epoch. A large portion of our first night of observation was plagued by very high seeing – as high as 3.0″ at times. We chose a cutoff seeing value of 1.2″ and defined a filtered Trojan set containing only Trojans detected in images with seeing below this value.

We used signal-to-noise to establish a limiting magnitude for our magnitude distribution analysis. Instead of attempting to generate an empirical model of the detection efficiency for the faintest objects, we elected to stipulate a conservative S/N threshold of 8. We defined the upper magnitude limit of our filtered Trojan data set to be the magnitude of the brightest object (detected at seeing less than 1.2″) with $S/N < 8$. The limiting magnitude was determined to be $H = 16.4$. The final filtered Trojan set contains 150 objects, and when fitting for the total magnitude distribution, we assume that this set is complete (i.e., is not characterized by any size-dependent bias).

Trojan colors

The color c of each Trojan is defined as the difference between the g and i magnitudes: $c \equiv g - i$. When calculating the uncertainty of each color measurement, we must consider the effect of asteroid rotation in addition to the contribution from photometric error. The oscillations in apparent amplitude seen in a typical asteroidal

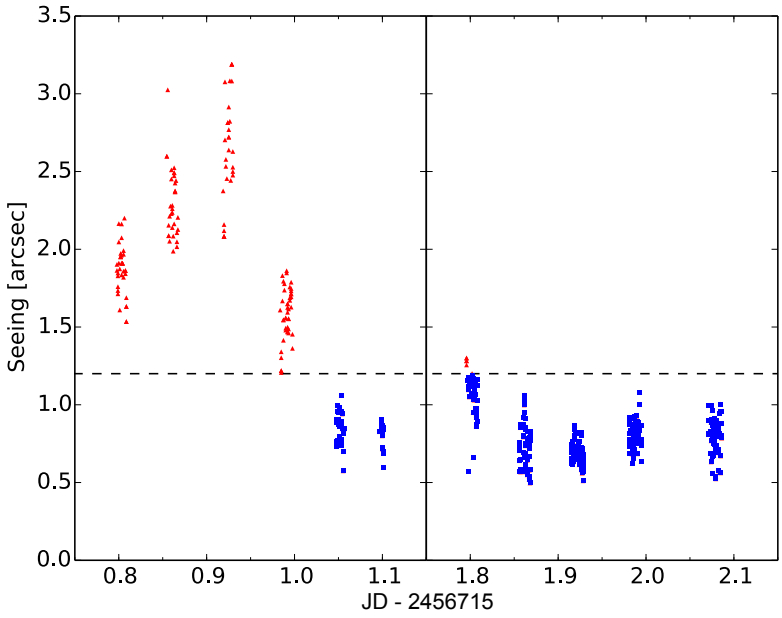

Figure 3.4: Seeing of the worst image (highest seeing) in every chip for each set of four exposures in the 147 observed fields, plotted as a function of the first exposure time. The dotted line indicates the cutoff at 1.2″ seeing – objects in fields with higher seeing (red triangles) are not included in the filtered Trojan set.

rotational light curve arise from the non-spherical shape of the object and peak twice during one full rotation of the asteroid (see, for example, the review by Pravec et al. 2002). The average observational arc of ∼70 minutes for each object may correspond to a significant fraction of a characteristic light curve oscillation period, which can consequently lead to a large variation in the apparent brightness of an object across the four epochs.

In the absence of published light curves for faint Trojans, we must develop a model of the rotational contribution to the color uncertainty in order to accurately determine the total uncertainty of our color measurements. We took advantage of the fact that we obtained two detections of an object in each filter to estimate the effect of asteroid rotation empirically. We considered the difference between the two consecutive g'-band magnitude measurements $\Delta g \equiv g_1 - g_2$. The standard deviation in Δg values, $\sigma_{\Delta g}$, contains a contribution from the photometric error given by the quadrature sum of the individual magnitude uncertainties as defined earlier: $\sigma_{\Delta g,\mathrm{phot}} = \sqrt{\sigma_{g,1}^2 + \sigma_{g,2}^2}$. Figure 3.5 compares the standard deviation of Δg values measured in 0.5 mag bins (blue squares) to the corresponding error contribution from the photometric

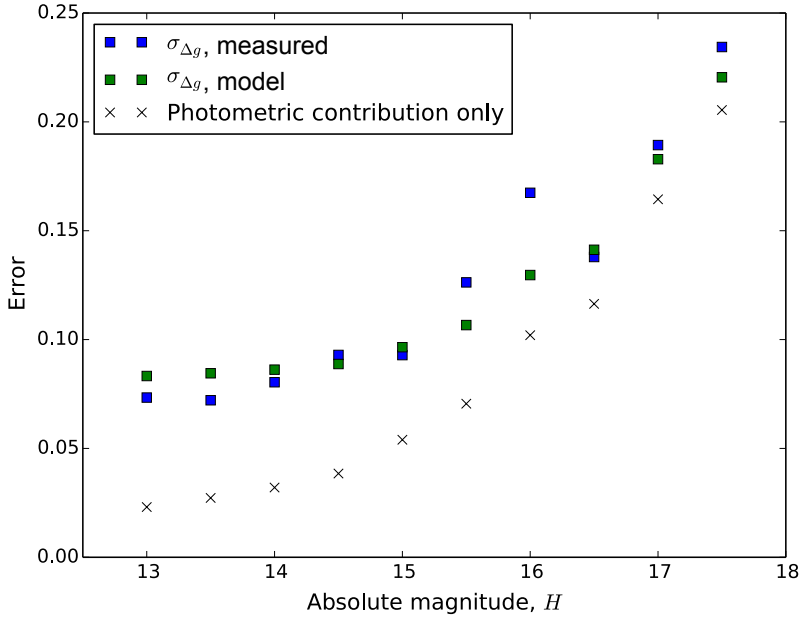

Figure 3.5: Comparison of the measured standard deviation error in the difference of g magnitudes, $\sigma_{\Delta g}$, binned in 0.5 mag intervals (blue squares) with the corresponding values from our empirical model combining the measured photometric magnitude errors with a constant contribution from asteroid rotation (green squares). The binned medians of the photometric errors only are denoted by black crosses. The agreement between the measured and modeled $\sigma_{\Delta g}$ values shows that the assumption of a magnitude-invariant contribution to the dispersion in Δg from asteroid rotation is good.

uncertainty only, $\sigma_{\Delta g,\mathrm{phot}}$ (black crosses).

From the plot, it is evident that an additional contribution attributable to rotation is needed to account for the uncertainty in Δg seen in our data. We observe that the discrepancy between $\sigma_{\Delta g}$ and the photometric error contribution is large at low magnitudes, where the photometric error is small, and decreases with increasing magnitude and increasing photometric error. This overall trend suggests that the total error in Δg can be empirically modeled as a quadrature sum of the photometric contribution and the rotational contribution, i.e., $\sigma_{\Delta g} = \sqrt{\sigma^2_{\Delta g,\mathrm{phot}} + \sigma^2_{\Delta g,\mathrm{rot}}}$, where the rotational contribution is magnitude-invariant. We found that a rotational contribution of $\sigma_{\Delta g,\mathrm{rot}} \sim 0.08$ gives a good match with the measured standard deviation in Δg, and likewise for Δi. In Figure 3.5, the green squares show the binned Δg standard deviation values calculated from our empirical model combining both photometric and rotational contributions.

The rotational contribution to the color uncertainty was estimated as a quadrature sum of the rotational contributions to Δg and Δi: $\sigma_{c,\mathrm{rot}} \sim 0.11$ mag. The total color uncertainty is therefore given by:

$$\sigma_c = \sqrt{\sigma_g^2 + \sigma_i^2 + \sigma_{c,\mathrm{rot}}^2}, \tag{3.1}$$

where σ_g and σ_i are the errors in the g and i magnitudes derived from the flux and calibrated zero-point magnitude errors only.

We note that the effects of bad seeing and detection incompleteness discussed in Section 3.2 are not expected to affect the bulk properties of the Trojan color distribution (e.g., mean color), except at the faintest magnitudes, where there is a slight bias toward redder objects. This is because we used the measured g magnitudes to convert to absolute magnitudes H. For objects with a given g magnitude, redder objects are slightly brighter in the i'-band (lower i magnitude) than less-red objects. The predicted effect is small, since the characteristic difference in $g-i$ color between objects in the red and less-red populations is only ∼0.15 mag (see Section 3.3). In our color analysis, we strove to avoid this small color bias by limiting the analysis to objects with H magnitudes less than 18, thereby removing the faintest several dozen objects from consideration.

3.3 Analysis

In this section, we first present our analysis of the total Trojan magnitude distribution, using both data for faint Trojans from our Subaru survey and data for brighter L4 Trojans listed in the Minor Planet Center catalog. Next, the distribution of measured $g-i$ colors and its magnitude dependence studied in the context of the less-red and red color populations described in Wong et al. (2014).

Total magnitude distribution

The cumulative magnitude distribution $N(H)$ of all objects in the filtered Trojan set (Section 3.2) as a function of H magnitude is shown in Figure 3.6. The main feature of the magnitude distribution is a slight rollover in slope to a shallower value at around $H \sim 15$. Following previous analyses of the magnitude distribution of Trojans (e.g., Jewitt et al. 2000), we fit the differential magnitude distribution, $\Sigma(H) = dN(M)/dH$, with a broken power law

$$\Sigma(\alpha_1, \alpha_2, H_0, H_b|H) = \begin{cases} 10^{\alpha_1(H-H_0)}, & \text{for } H < H_b \\ 10^{\alpha_2 H + (\alpha_1-\alpha_2)H_b - \alpha_1 H_0}, & \text{for } H \geq H_b \end{cases}, \tag{3.2}$$

where the power law slope for brighter objects α_1 changes to a shallower faint-end slope α_2 at a break magnitude H_b. The parameter H_0 defines the threshold magnitude for which $\Sigma(H_0) = 1$.

We fit the model curve in Equation (3.2) to our filtered Trojan magnitude distribution using a maximum likelihood method similar to the one used in Fraser et al. (2008) for their study of Kuiper Belt objects. We defined a likelihood function L that quantifies the probability that a random sampling of the model distribution will yield the data:

$$L(\alpha_1, \alpha_2, H_0, H_b|H_i) \propto e^{-N} \prod_i P_i. \tag{3.3}$$

Here, H_i is the H magnitude of each detected Trojan and $P_i = \Sigma(\alpha_1, \alpha_2, H_0, H_b|H_i)$ is the probability of detecting an object i with magnitude H_i given the underlying distribution function Σ. N is the total number of objects detected in the magnitude range under consideration and is given by

$$N = \int_{-\infty}^{H_{\max}} \eta(H)\Sigma(\alpha_1, \alpha_2, H_0, H_b|H)\, dH, \tag{3.4}$$

where in the case of our filtered Trojan set we have $H_{\max} = 16.4$. We have included the so-called "efficiency" function $\eta(H)$ that represents an empirical model of the incompleteness in a given data set and ensures that the best-fit distribution curve corrects for any incompleteness in the data. Our filtered Trojan data set was defined to remove incompleteness contributions from both bad seeing and low signal-to-noise, so when fitting the broken power law to the corresponding magnitude distribution, we set $\eta = 1$.

We used an affine-invariant Markov Chain Monte Carlo (MCMC) Ensemble sampler (Foreman-Mackey et al. 2013) with 50,000 steps to estimate the best-fit parameters and corresponding 1σ uncertainties. The magnitude distribution of the filtered Trojan set is best-fit by a broken power law with parameter values $\alpha_1 = 0.45 \pm 0.05$, $\alpha_2 = 0.36^{+0.05}_{-0.09}$, $H_0 = 11.39^{+0.31}_{-0.37}$, and $H_b = 14.93^{+0.73}_{-0.88}$. The cumulative magnitude distribution for this best-fit model is plotted in Figure 3.6 as a solid black line. We note that while the difference between the two power-law slopes is small, it is statistically significant; marginalizing over the slope difference $\Delta\alpha = \alpha_1 - \alpha_2$, we obtained $\Delta\alpha = 0.10^{+0.09}_{-0.08}$, which demonstrates that the difference between the two power-law slopes is distinct from zero at the 1.25σ level.

We also fit the magnitude distribution of known bright Trojans contained in the Minor Planet Center (MPC) catalog by repeating the analysis described in Wong

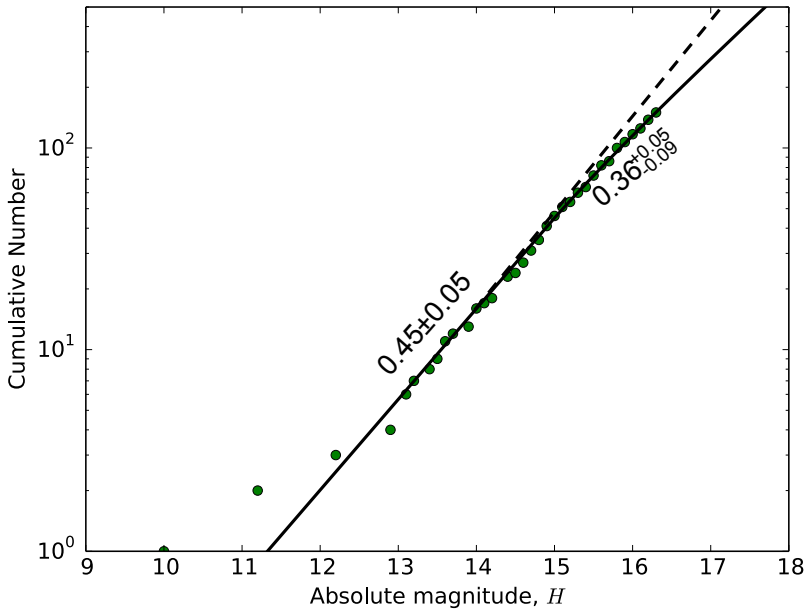

Figure 3.6: Cumulative absolute magnitude distribution of the filtered Trojan set from our Subaru observations, binned by 0.1 mag (green dots). The best-fit broken power law curve describing the distribution is overplotted (solid black line), with the power law slopes indicated. The dashed line is an extension of the $\alpha_1 = 0.45$ slope and is included to make the slope rollover more discernible.

et al. (2014), this time including only L4 Trojans. Fitting the distribution of bright L4 Trojans likewise to a broken power law of the form shown in Equation (3.2), we obtained a best-fit distribution function with $\alpha_0' = 0.91^{+0.19}_{-0.16}$, $\alpha_1' = 0.43 \pm 0.02$, $H_0' = 7.22^{+0.24}_{-0.25}$, and $H_b' = 8.46^{+0.49}_{-0.54}$. We have denoted the best-fit parameters for the MPC Trojan magnitude distribution with primes to distinguish them from the best-fit parameters for the Subaru Trojans; the subscripts on the slope parameters α are adjusted to reflect the magnitude ranges they correspond to in the overall distribution. The cumulative magnitude distribution of MPC L4 Trojans through $H = 12.3$ (corrected for catalog incompleteness following the methodology described in Wong et al. 2014) is shown in Figure 3.7 along with the best-fit curve.

Earlier studies of L4 Trojans in this size range have reported power law slopes that are consistent with our values: Yoshida & Nakamura (2008) fit MPC L4 Trojans with magnitudes in the range $9.2 < H < 12.3$ and derived a slope of 0.40 ± 0.02. We note that their fit did not take into account the incompleteness in the MPC catalog, which we estimated in Wong et al. (2014) to begin at $H = 11.3$. Therefore, the

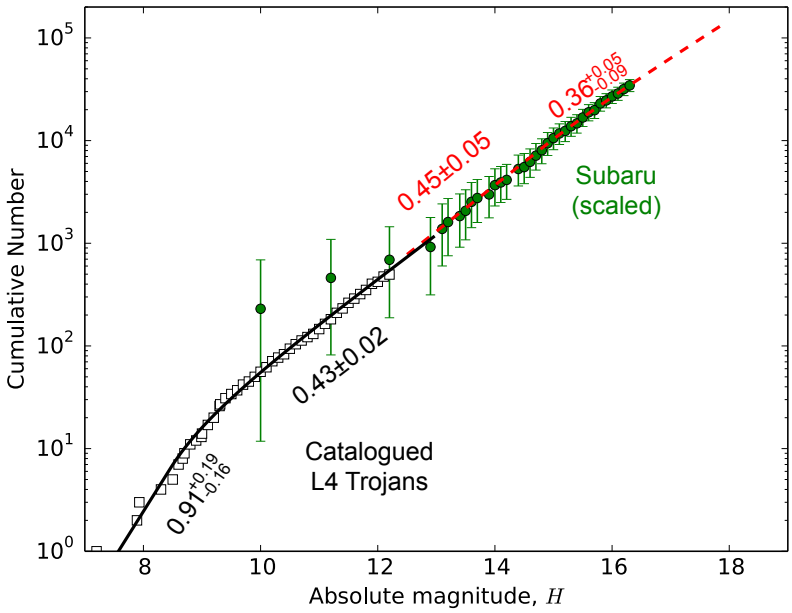

Figure 3.7: Cumulative magnitude distribution of all L4 Trojans contained in the Minor Planet Center (MPC) catalog brighter than $H = 12.3$ (white squares; corrected for incompleteness in the range $H = 11.3-12.3$ following the methodology of Wong et al. 2014) and the cumulative magnitude distribution of the filtered Trojan set from our Subaru observations, approximately scaled to reflect the true overall number and binned by 0.1 mag (green dots). The error bars on the scaled Subaru Trojan magnitude distribution (in green) denote the 95% confidence bounds derived from scaling the Poisson errors on the Subaru survey data. The uncertainties on the corrected MPC catalog Trojan magnitude distribution in the range $H = 11.3 - 12.3$ are much smaller than the points. The best-fit broken power law curves describing the MPC and Subaru data are overplotted (solid black and dashed red lines, respectively), with the power law slopes (in the text: α'_0, α'_1, α_1, and α_2) indicated for their corresponding magnitude regions.

slope value in Yoshida & Nakamura (2008) is somewhat underestimated. Jewitt et al. (2000) carried out a survey of L4 Trojans and computed slopes of 0.9 ± 0.2 and 0.40 ± 0.06 over size ranges corresponding to our reported α'_0 and α'_1 slopes, respectively. Our best-fit power law slopes calculated for bright MPC L4 Trojans are consistent with these previously-published values at better than the 1σ level.

We combined the magnitude distributions of faint Subaru Trojans and brighter catalogued Trojans to arrive at the overall magnitude distribution of L4 Trojans, shown in Figure 3.7, where the cumulative absolute magnitude distribution of faint Trojans was approximately scaled to match the overall number of MPC Trojans at

$H \sim 12$. The error bars indicate 95% confidence bounds derived from Poisson errors on the Subaru survey data and reflect the uncertainty associated with scaling up the survey magnitude distribution to approximate the magnitude distribution of the total L4 population. The combined Subaru and MPC data sets cover the entire magnitude range from $H = 7.2$ to a limiting magnitude of $H_{\rm max} = 16.4$. The best-fit power law distribution slopes in the region containing the overlap between the MPC and Subaru data sets ($\alpha_1' = 0.43 \pm 0.02$ and $\alpha_1 = 0.45 \pm 0.05$) are statistically equivalent, indicating that the magnitude distribution between $H \sim 10$ and $H \sim 15$ is well-described by a single power law slope. The overall magnitude distribution is characterized by three distinct regions. The brightest L4 Trojans have a power law magnitude distribution with slope $\alpha_0 = 0.91$. At intermediate sizes, the magnitude distribution rolls over to a slope of $\alpha_1 \sim 0.44$. Finally, the faintest objects detected in our Subaru survey are characterized by an even shallower magnitude distribution slope of $\alpha_2 = 0.36$. These three regions are separated at the break magnitudes $H_b' = 8.46^{+0.49}_{-0.54}$ and $H_b = 14.93^{+0.73}_{-0.88}$, which correspond to Trojans of size 135^{+38}_{-27} km and 7^{+3}_{-2} km, respectively.

In a previous study, Yoshida & Nakamura (2005) detected 51 faint L4 Trojans near opposition using the Suprime-Cam instrument and found the magnitude distribution to be well-described by a broken power law with a break at around $H \sim 16$ separating a brighter-end slope of 0.48 ± 0.02 from a shallower faint-end slope of 0.26 ± 0.02. The methods used in the Yoshida & Nakamura (2005) fits differed from ours in several ways: The data was binned prior to fitting, and the two slopes were determined from independent fits of the bright and faint halves of their data. To better compare the distribution of Trojans studied by Yoshida & Nakamura (2005) with the best-fit distribution we derived from our Subaru survey, we reanalyzed their data using the techniques described in this paper. Fitting all of the Yoshida & Nakamura (2005) magnitudes through $H = 17.9$ (90% completeness limit) to a broken power-law, we obtained the two slopes $\alpha_{1,\rm Y\&N} = 0.44^{+0.07}_{-0.06}$ and $\alpha_{2,\rm Y\&N} = 0.26^{+0.06}_{-0.04}$ and a roll-over at $H_{b,\rm Y\&N} = 15.11^{+0.89}_{-1.02}$. These values are consistent with the corresponding best-fit values for α_1, α_2, and H_b from the analysis of our Subaru survey data at better than the 1σ level.

Color distribution

Previous spectroscopic and photometric studies of Trojans have noted bimodality in the distribution of various properties, including the visible (Szabó et al. 2007; Roig et al. 2008; Melita et al. 2008) and near-infrared (Emery et al. 2011) spectral slope,

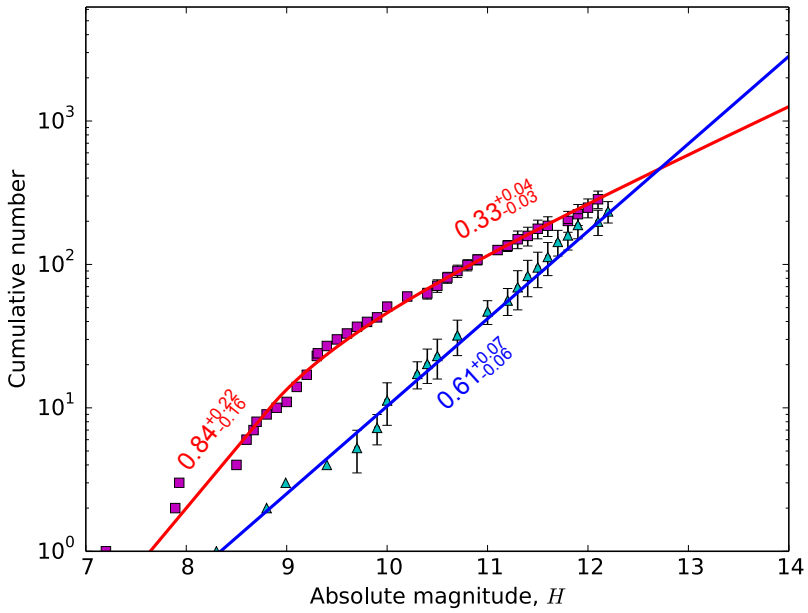

Figure 3.8: Cumulative magnitude distribution of the less-red and red L4 Trojan populations, as constructed using the methods of Wong et al. (2014) for objects in the Minor Planet Center catalog through $H = 12.3$ (cyan triangles and red squares, respectively). These distributions have been scaled to correct for catalog and categorization incompleteness; the error bars denote the 95% confidence bounds and are derived from the binomial distribution errors associated with correcting for uncategorized less-red and red Trojans, as well as the uncertainties from the catalog incompleteness correction in the range $H = 11.3 - 12.3$. The best-fit curves describing the distributions are overplotted (solid blue and red lines, respectively), with the power law slopes indicated for their corresponding magnitude regions.

as well as the infrared albedo (Grav et al. 2012). Wong et al. (2014) demonstrated that the bimodal trends were indicative of two separate populations within the Trojans, which are referred to as the less-red and red populations, in accordance with their relative colors. It was further shown that the magnitude distributions of these two color populations are distinct, with notably different power-law slopes in the magnitude range $H \sim 9.5 - 12.3$.

We repeated the color population analysis presented in Wong et al. (2014), using only L4 Trojans. Objects were categorized as less-red or red primarily based on their visible spectral slopes, which were derived from the g, r, i, and z magnitudes listed in 4th release of the SDSS Moving Object Catalog (SDSS-MOC4). We estimated the incompleteness in color categorization via the fraction of objects in each 0.1 mag bin

that we were able to categorize as either less-red or red; when fitting the magnitude distributions of the color populations up to a limiting magnitude of $H = 12.3$, the categorization incompleteness was factored into the efficiency function η along with the estimated incompleteness of the MPC catalog. See Wong et al. (2014) for a complete description of the methodology used.

The magnitude distributions of the color populations were fit using the same techniques that we applied in the total magnitude distribution fits. The red population magnitude distribution is best-fit by a broken power law with $\alpha_1^R = 0.84^{+0.22}_{-0.16}$, $\alpha_2^R = 0.33^{+0.04}_{-0.03}$, $H_0^R = 7.30^{+0.30}_{-0.26}$, and $H_b^R = 8.82^{+0.35}_{-0.44}$. The less-red population has a magnitude distribution more consistent with a single power law: $\Sigma(\alpha_1, H_0|H) = 10^{\alpha_1(H-H_0)}$; here we computed the following best-fit parameters: $\alpha_1^{LR} = 0.61^{+0.07}_{-0.06}$ and $H_0^{LR} = 8.18^{+0.31}_{-0.29}$. Figure 3.8 shows the cumulative magnitude distributions for the less-red and red populations, scaled to correct for incompleteness, along with the best-fit curves. The error bars indicate the 95% confidence bounds derived from the incompleteness correction. The best-fit slopes calculated above for the L4 color populations are consistent within the errors to the corresponding values in Wong et al. (2014) derived from the color analysis of both L4 and L5 Trojans.

To determine whether the previously-studied bimodality in color among the brighter Trojans carries through to the fainter Trojans from our Subaru observations, we constructed a histogram of the $g-i$ color distribution for all Trojans contained in the SDSS-MOC4 catalog and compared it to the histogram of $g-i$ colors for Trojans detected in our Subaru survey. As discussed in Section 3.2, the bulk distribution of colors is not expected to be affected by detection incompleteness due to bad seeing, and we include all Trojans brighter than $H = 18$. The two histograms are plotted in Figure 3.9. The bimodality in the color histogram of brighter SDSS-MOC4 objects is evident. We fit a two-peaked Gaussian to the color distribution of brighter SDSS-MOC4 Trojans and found that the less-red and red populations have mean $g-i$ colors of $\mu_1 = 0.73$ and $\mu_2 = 0.86$, respectively.

On the other hand, while there is some asymmetry in the color distribution of faint Trojans detected by our Subaru survey, there is no robust bimodality. This can be mostly attributed to the large contribution of asteroid rotation to the variance in the color measurements, the magnitude of which is comparable to the difference between the mean red and less-red colors (see Section 3.2). As such, it is not possible to categorize individual Trojans from our Subaru observations into the less-red and

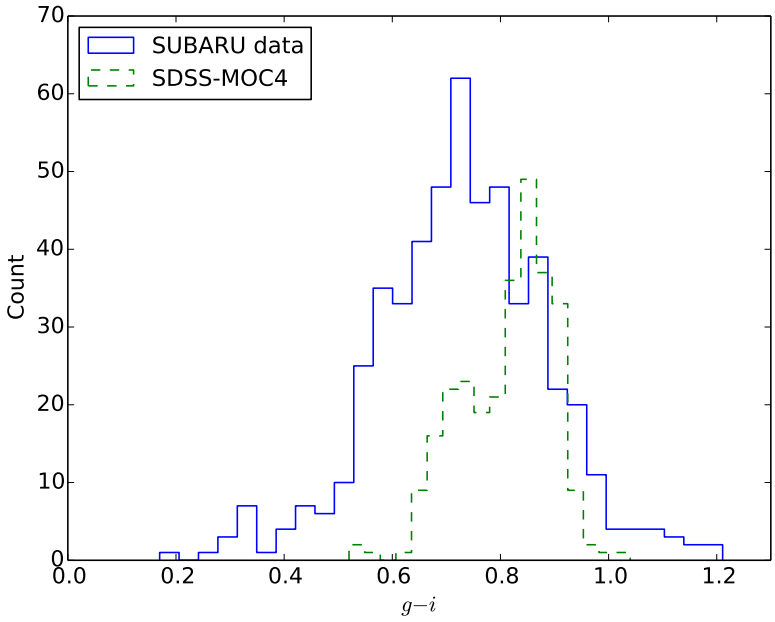

Figure 3.9: Histogram of the $g - i$ color distribution for Trojans contained in the SDSS-MOC4 catalog brighter than $H = 12.3$ (green) and fainter Trojans detected in our Subaru survey (blue). There is clear bimodality in the distribution of brighter objects in the SDSS-MOC4 catalog, while the distribution of faint Trojan colors does not display a clear bimodality. This is likely due to the large relative uncertainties associated with the measurement of faint Trojan colors due to asteroid rotation.

red populations based on their colors and construct magnitude distributions of the color populations, as was done in Wong et al. (2014) for the brighter SDSS-MOC4 Trojans.

Instead, we considered bulk properties of the distribution. In particular, we calculated the mean $g - i$ color as a function of H magnitude for the combined set of SDSS-MOC4 Trojans and faint Trojans from our Subaru observations in order to assess whether the resulting trend is consistent with extrapolation of the best-fit color magnitude distributions obtained previously for the brighter objects (i.e., curves in Figure 3.8). Here, we assumed that the mean colors of the two color populations are invariant across all magnitudes. The mean $g - i$ color and uncertainty in the mean for the data were computed in 1 mag bins and are plotted in Figure 3.10 in blue. We see that the mean color is consistent with a monotonically-decreasing trend with increasing magnitude, or equivalently, decreasing size. To derive the extrapolated mean color values from the best-fit color magnitude distributions, we

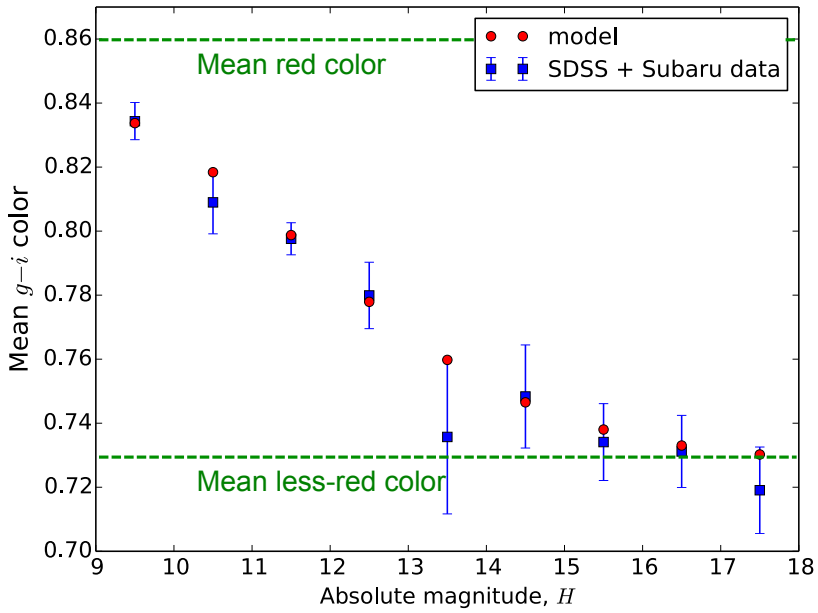

Figure 3.10: Mean $g-i$ colors and corresponding uncertainties for the combined set of Trojans detected in our Subaru survey and L4 Trojans listed in SDSS-MOC4 (blue squares with error bars). Red dots denote the predicted mean $g-i$ color values computed from extrapolation of the best-fit less-red and red population magnitude distributions, assuming mean less-red and red colors of 0.73 and 0.86, respectively. The mean less-red and red $g-i$ colors are indicated by dashed green lines. The monotonic decrease in mean $g-i$ color indicates an increasing fraction of less-red Trojans with decreasing size. The agreement between the extrapolated values and the measured ones suggests that the best-fit color-magnitude distributions derived from bright catalogued Trojans likely extend throughout the magnitude range studied by our Subaru survey.

calculated the expected mean color at each bin magnitude as a weighted mean $c'(H) = (\mu_1 \times \Sigma^{LR}(H) + \mu_2 \times \Sigma^{R}(H))/(\Sigma^{LR}(H) + \Sigma^{R}(H))$, where $\mu_{1,2}$ are the mean $g-i$ colors of the less-red and red populations, respectively, as derived previously from fitting the color distribution of SDSS-MOC4 Trojans. The functions $\Sigma^{LR}(H)$ and $\Sigma^{R}(H)$ are the best-fit differential magnitude distributions for the less-red and red populations presented earlier. The resulting model mean color values are denoted in Figure 3.10 by red dots.

The extrapolated mean colors show very good agreement with the mean colors derived from the data. This suggests that the best-fit magnitude distributions for the less-red and red color populations shown in Figure 3.8 continue past the limiting

magnitude of the MPC data analysis ($H = 12.3$) and likely extend throughout most of the magnitude range covered by our Subaru observations. We conclude that the fraction of less-red objects in the overall L4 Trojan population increases steadily with increasing magnitude (decreasing size), and that L4 Trojans fainter than $H \sim 16$, or equivalently, smaller than ~4 km in diameter, are almost entirely composed of less-red objects.

3.4 Discussion

The analysis of faint Trojans detected in our Subaru survey offers the most complete picture of the L4 Trojan population to date, refining the known absolute magnitude distribution over the entire range from $H = 7.2$ to $H = 16.4$ and providing the distribution of Trojan colors down to kilometer-sized objects. The most notable features in the total magnitude distribution (Figure 3.7) are the two slope transitions at $H \approx 8.5$ and $H \approx 15.0$. Such breaks in the power-law shape are common features in the magnitude distributions of small body populations throughout the Solar System and are generally attributed to collisional evolution (see, for example, the review by Durda et al. 1998). Previous studies of the Trojans' collisional history sought to explain the observed bright-end break at $H \approx 8.5$ using collisional modeling (e.g. Wong et al. 2014; Marzari et al. 1997; de Elía & Brunini 2007) and found that, given the very low intrinsic collisional probability of the Trojan clouds, the bright-end slope transition is best reproduced by assuming that a break was present at the time when the Trojans were emplaced in their current location. In other words, the collisional activity among the large Trojans over the past ~4 Gyr is likely not sufficient to have produced the bright-end break at $H \approx 8.5$ starting from a single power-law slope. We propose that it is the faint-end break at $H \approx 15.0$ that represents the transition to the part of the Trojan population that has reached collisional equilibrium since emplacement; objects brighter than the faint-end break have not reached collisional equilibrium and therefore largely reflect the primordial magnitude distribution of the Trojans at the time of capture by Jupiter.

Turning to the color distributions, we recall that the magnitude distribution fits we obtained for the less-red (LR) and red (R) color populations through $H = 12.3$ (see Figure 3.8) show highly distinct slopes for objects fainter than the bright-end break ($0.33^{+0.04}_{-0.03}$ for the R population, and $0.61^{+0.07}_{-0.06}$ for the LR population). This indicates that the fraction of LR objects in the overall population increases with increasing magnitude. In Section 3.3, we found that this general trend continues throughout the magnitude range covered in our Subaru survey. As was done in Wong et al. (2014)

based on the color-magnitude analysis of L4 and L5 Trojans listed in the Minor Planet Center catalog, we posit that the LR vs. R magnitude distribution slope discrepancy can be explained if R objects convert to LR objects upon collision. Such a process would naturally account for the relative flattening the R population's magnitude distribution slope and the simultaneous steepening of LR population's magnitude distribution slope.

The R-to-LR conversion model assessed here suggests that the LR and R Trojans have similar interior compositions, with the difference in color confined to the exposed surface layer. Current models of solar system formation and evolution indicate that the Trojans may have been sourced from the same body of material as the KBOs, located in the region of the disk beyond the primordial orbit of Neptune (Morbidelli et al. 2005). Recent observational studies of KBOs have revealed that the Kuiper Belt is composed of several sub-populations, among which are the so-called "red" and "very red" small KBOs (Fraser et al. 2008; Peixinho et al. 2012). Brown et al. (2011) hypothesized that this color bimodality may be attributable to the wide range of heliocentric distances at which the KBOs formed. In this scenario, all of these objects were accreted from a mix of rock and volatile ices of roughly cometary composition. Immediately following the dissipation of the primordial disk, the surface ices on these bodies began sublimating from solar irradiation, with the retention of a particular volatile ice species on an object's surface being determined primarily by the temperature of the region where the object resided: Objects located at greater heliocentric distances would have retained that ice species on their surfaces, while those that formed at lesser heliocentric distances would have surfaces that were completely depleted in that ice species. Brown et al. (2011) proposed that the continued irradiation of volatile ices led to a significant darkening of the surface and the formation of a robust irradiation mantle, which served to protect ices in the interior from sublimating away. The precise effect of irradiation on the surface is likely dependent on the types of volatile ices retained on the surface. Therefore, the presence or absence of one particular volatile ice species may be the key factor in producing the observed color bimodality in the small KBOs. Specifically, objects that retained that volatile ice species on their surfaces formed a "very red" irradiation mantle, while those that lost that volatile ice species from their surfaces formed a "red" irradiation mantle.

Wong et al. (2014) suggested that the LR and R Jupiter Trojans may have been drawn from the same two sources as the "red" and "very red" KBOs, respectively.

Upon a catastrophic impact, the irradiation mantle on a Trojan's surface would disintegrate and any exposed volatile ices in the interior would sublimate away within a relatively short timescale, leaving behind collisional fragments composed primarily of water ice and rock. Without the differing collection of volatile ices on the surface to distinguish them, the fragments of LR objects and R objects would be spectroscopically identical to each other. Subsequent irradiation of these pristine fragments would raise the spectral slope slightly, but not to the same extent as would result if volatile ices were retained on the surface. All collisional fragments, regardless of the surface color of their progenitor bodies, would eventually attain the same surface color, which would be relatively less-red when compared to the color of R Trojans. As a consequence, collisional evolution of the Trojan population since emplacement would have gradually depleted the number of R Trojans while simultaneously enriching the number of LR Trojans.

To assess the hypotheses mentioned above, we ran a series of numerical simulations to model the collisional evolution of the L4 Trojan population since emplacement, following the methodology used in Wong et al. (2014). Given the low intrinsic collisional probability of Trojans, we defined the initial magnitude distribution as a broken power law of the form described in Equation (3.2) with a bright-end distribution identical to that of the currently-observed L4 population ($\alpha_1 = 0.91$, $H_0 = 7.22$, and $H_b = 8.46$). We varied the initial faint-end slope α_2^* across different trials. The initial population for each trial consisted of objects with absolute magnitudes in the range $H = 7 \rightarrow 30$, divided into 75 logarithmic diameter bins.

We constructed the initial color populations by taking constant fractions of the total initial population across all bins. The initial R-to-LR number ratio, k, ranged from 4 to 6, in increments of 0.5. The collisional evolution was carried out over 4 Gyr in 100000 time steps of length $\Delta t = 40000$. At each time step, the expected number of collisions $N_{\rm coll}$ between bodies belonging to any pair of bins is given by

$$N_{\rm coll} = \frac{1}{4}\langle P \rangle N_{\rm tar} N_{\rm imp} \Delta t (D_{\rm tar} + D_{\rm imp})^2, \tag{3.5}$$

where $N_{\rm tar}$ and $N_{\rm imp}$ are the number of objects in a target bin with diameter $D_{\rm tar}$ and an impactor bin with diameter $D_{\rm imp}$, respectively; $\langle P \rangle = 7.79 \times 10^{-18}$ yr^{-1} km^{-2} is the intrinsic collision probability for Trojan-Trojan collisions calculated by Dell'Oro et al. (1998) for L_4 Trojans. For objects with diameter $D_{\rm tar}$, there exists a minimum impactor diameter $D_{\rm min}$ necessary for a shattering collision. $D_{\rm min}$ is defined as

(Bottke et al. 2005)

$$D_{\min} = \left(\frac{2Q_D^*}{V_{\rm imp}^2}\right)^{1/3} D_{\rm tar}, \tag{3.6}$$

where $V_{\rm imp} = 4.66$ km s^{-1} is the L_4 impact velocity calculated by Dell'Oro et al. (1998), and Q_D^* is the collisional strength of target. In our algorithm, we utilized a size-dependent strength scaling law based off one used by Durda et al. (1998) in their treatment of collisions among small main-belt asteroids:

$$Q_D^* = c \cdot 10 \cdot (155.9D^{-0.24} + 150.0D^{0.5} + 0.5D^{2.0})\ \mathrm{J\,kg^{-1}}. \tag{3.7}$$

Here, we included a normalization parameter c to adjust the overall scaling of the strength; c varied in increments of 0.5 from 1 to 10 in our test trials. The strength scaling model used here has a transition from a gravity-dominated regime for large objects to a strength-dominated regime for smaller objects. For large Trojans, the collisional strength increases rapidly with increasing size, since the impact energy required to completely shatter a large object is primarily determined by the escape velocity of collisional fragments. At smaller sizes (below about 1 km in diameter), the intrinsic material strength of the target becomes the dominant factor; here, smaller objects tend to have fewer cracks and defects than larger objects, and therefore the collisional strength increases with decreasing size.

Our model computed the collisional evolution of the two color populations separately. At each time step, the simulation considered the number of collisions between objects of the same color, as well as collisions involving objects of different colors. The conversion of red objects to less-red fragments through shattering was modeled by placing all collisional fragments into less-red bins, regardless of the color of the target or the impactor. After running simulations for various values of the parameters (α_2^*, k, c), we found that a large number of test runs yielded final total and color magnitude distributions that were consistent with the best-fit distributions of catalogued Trojans presented in Section 3.3. To determine which run best reproduced the observed distributions, we compared the simulation results directly with the best-fit distribution curves and minimized the chi-squared statistic. Here, χ^2 was computed as the sum of χ^2 values for the total, LR, and R magnitude distributions. The test run that resulted in the best agreement with the data has an initial total distribution with faint-end slope $\alpha_2^* = 0.44$, a strength scaling parameter $c = 1.0$, and an initial R-to-LR number ratio $k = 5.5$. Plots comparing the final simulated distributions from this test run to the best-fit distribution curves are shown

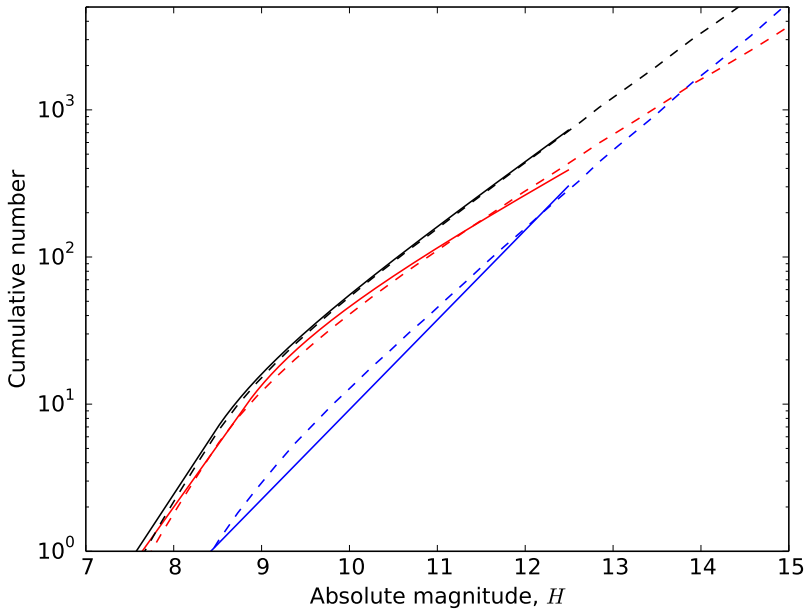

Figure 3.11: Comparison between the results from the best test run of our collisional simulation (dotted lines) and the observed L4 Trojan magnitude distributions (solid lines). The initial total magnitude distribution for the best test run is a broken power law with $\alpha_1 = 0.91$, $\alpha_2^* = 0.44$, $H_0 = 7.22$, $H_b = 8.46$, an initial R-to-LR number ratio $k = 5.5$ and a strength normalization factor $c = 1.0$. Black, red, and blue colors indicate the magnitude distribution of the total, red, and less-red populations, respectively. The consistency of the model results and the best-fit distributions demonstrates that the proposed conversion of R objects to LR fragments upon collision is capable of explaining the different shapes of the LR and R magnitude distributions.

in Figure 3.11. It is important to note that the simulated total magnitude distribution from the collisional model is not sensitive to the R-to-LR conversion, and the ability of our simulations to reproduce the observed total magnitude distribution holds regardless of any assumptions made about the nature of the color populations.

The similarity between the best initial test distribution and the current total magnitude distribution reaffirms the conclusion of previous studies that collisions have not played a major role in shaping the magnitude distribution of large Trojans since emplacement. Meanwhile, the R-to-LR collisional conversion model yields simulated final color magnitude distributions that match the best-fit color magnitude distributions of catalogued Trojans well. Furthermore, we computed the expected trend in mean $g - i$ color from the simulated color magnitude distributions through the mag-

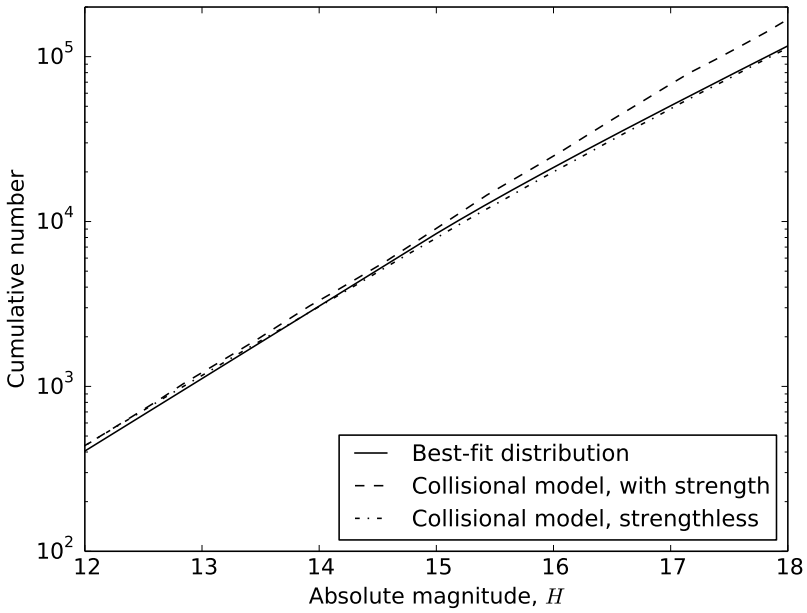

Figure 3.12: Comparison of the best-fit cumulative magnitude distribution curve from the survey data (solid line) with the final predicted distribution from two collisional simulation runs: (1) test run assuming bodies with collisional strength given by Equation (3.7) (dashed line) and (2) test run assuming strengthless bodies with collisional strength scaling given by Equation (3.8) (dot-dash line). The better agreement of the latter suggests that Trojans have very low material strength, similar to comets.

nitude region spanning the Subaru Trojan data and found that the trend is consistent with the measured mean $g - i$ colors from the data (as shown in Figure 3.10).

To determine whether the collisional model can reproduce the faint-end break at $H \approx 15.0$, we compared the simulated final magnitude distribution from the best test run with the observed magnitude distribution of faint Trojans from our Subaru data (Figure 3.12). All of the simulation test runs predict a break at around $H = 14 - 15$; however, the slope that the simulated distributions roll over to is almost identical to the slope ahead of the break. In the case of the best test run, the faint-end rollover in the simulated final magnitude distribution is barely discernible. In terms of collisional equilibrium, this means that the predicted equilibrium slope is around $\alpha_{\rm eq} \sim 0.43$. Meanwhile, the actual faint-end slope derived from fitting the Subaru data is somewhat shallower ($\alpha_2 = 0.36^{+0.05}_{-0.09}$).

One possible explanation for this discrepancy is that the collisional strength of

Trojans may not be well-described by the strength model defined in Equation (3.7). To explore this possibility, we considered the case where Trojans have negligible material strength and are loosely-held conglomerates of rock and ice similar to comets. We modified the collisional strength scaling relation to incorporate only the effect of self-gravity by removing the transition to a strength-dominated regime that we included in the previous model. The new strength formula is given by

$$Q_D^* = c \cdot 5D^{2.0}\ \mathrm{J\,kg^{-1}}. \tag{3.8}$$

Rerunning the collisional simulations with this new collisional strength scaling, we established a new best test run for strengthless bodies with $\alpha_2^* = 0.45$, $k = 5.5$, and $c = 0.5$. The simulated color magnitude distributions in the strengthless case were found to be generally consistent with the ones produced in the original non-strengthless model and likewise predict the observed trend in mean $g - i$ color through $H \sim 18$. The simulated final magnitude distribution from this model in the vicinity of the faint-end break is shown in Figure 3.12. We can see that the predicted distribution for strengthless Trojans provides a better match to the data than the previous case of non-strengthless bodies. This indicates that Trojans may have very low material strength, which would make them more comparable to comets than to main belt asteroids and lend support to the hypothesis presented earlier that the Jupiter Trojans formed in the primordial trans-Neptunian region and were later scattered inward during a period of dynamical instability.

3.5 Conclusion

We detected 557 Trojans in a wide-field survey of the leading L4 cloud using the Suprime-Cam instrument on the Subaru Telescope. All objects were imaged in two filters, and the $g - i$ color was computed for each object. After removing objects imaged during bad seeing and establishing a limiting magnitude of $H = 16.4$, we computed the best-fit curves describing the overall magnitude distribution. In addition, we examined the distribution of $g - i$ colors for the faint objects detected by our survey and compared it to an extrapolated model based on the magnitude distributions of bright, catalogued objects in the less-red and red Trojan populations. The color-magnitude distribution analysis was supplemented by collisional simulations, from which we made predictions about the formation and evolution of the Trojan population. The main results are summarized below:

- The overall magnitude distribution of L4 Trojans is described by three power-law slopes: The distribution of the brightest objects follows a power law slope

of $\alpha_0 = 0.91^{+0.19}_{-0.16}$. At intermediate sizes, the magnitude distribution rolls over to a slope of $\alpha_1 \sim 0.44$. Finally, the faintest objects are characterized by an even shallower magnitude distribution slope of $\alpha_2 = 0.36^{+0.05}_{-0.09}$. These three regions are separated by rollovers in the magnitude distribution located at $H'_b = 8.46^{+0.49}_{-0.54}$ and $H_b = 14.93^{+0.73}_{-0.88}$, which correspond to objects with diameters of 135^{+38}_{-27} km and 7^{+3}_{-2} km, respectively.

- The faint-end break in the overall Trojan magnitude distribution at $H \sim 15$ is reproduced by our collisional simulations and indicates the transition between objects that have not experienced significant collisional evolution and objects that have achieved collisional equilibrium.

- The shallow faint-end slope ($\alpha_2 = 0.36^{+0.05}_{-0.09}$) is consistent with Trojans having very low material strength, similar to comets.

- The mean $g - i$ color of Trojans follows a general decreasing trend with increasing magnitude, or equivalently, decreasing size. At faint magnitudes, this trend is consistent with the extrapolation of magnitude distribution fits computed for bright objects in the less-red and red populations. Less-red objects dominate among objects smaller than ∼5 km in diameter.

- The discrepant best-fit slopes of the color-magnitude distributions for objects smaller than ∼50 km and the monotonically-decreasing trend in mean $g - i$ color with decreasing size are consistent with the conversion of red objects to less-red fragments upon collision.

References

Bernstein, G. M., Trilling, D. E., Allen, R. L., & Brown, M. E. (2004). "The size distribution of trans-Neptunian bodies". *AJ*, 128, 1364.

Bertin, E. (2006). "Automatic Astrometric and Photometric Calibration with SCAMP". In: *Astronomical Data Analysis Software and Systems XV (ASP Conf. Ser. 351)*. Eds. Gabriel, C., Arviset, C., Ponz, D., & Enrique, S. (San Francisco, CA: ASP), 112.

Bertin, E. & Arnouts, S. (1996). "SExtractor: Software for source extraction". *A&AS*, 117, 393.

Bottke, W. F., Durda, D. D., Nervorný, D., et al. (2005). "The fossilized size distribution of the main asteroid belt". *Icarus*, 175, 111.

Brown, M. E., Schaller, E. L., & Fraser, W. C. (2011). "A hypothesis for the color diversity of the Kuiper belt". *ApJ*, 739, L60.

de Elía, G. C. & Brunini, A. (2007). "Collisional and dynamical evolution of the L_4 Trojan asteroids". *A&A*, 475, 375.

Dell'Oro, A., Marzari, F., Paolicchi, P., Dotto, E., & Vanzani, V. (1998). "Trojan collision probability: A statistical approach". *A&A*, 339, 272.

Dotto, E., Fornasier, S., Barucci, M. A., et al. (2006). "The surface composition of Jupiter Trojans: Visible and near-infrared survey of dynamical families". *Icarus*, 183, 420.

Durda, D. D., Greenberg, R., & Jedicke, R. (1998). "Collisional models and scaling laws: A new interpretation of the shape of the main-belt asteroid size distribution". *Icarus*, 135, 431.

Emery, J. P., Burr, D. M., & Cruikshank, D. P. (2011). "Near-infrared spectroscopy of Trojan asteroids: Evidence for two compositional groups". *AJ*, 141, 25.

Fernández, Y. R., Jewitt, D., & Ziffer, J. E. (2009). "Albedos of small Jovian Trojans". *AJ*, 138, 240.

Foreman-Mackey, D., Hogg, D. W., Lang, D., & Goodman, J. (2013). "emcee: The MCMC Hammer". *pre-print*. arXiv:1202.3665.

Fornasier, S., Dotto, E., Hainaut, O., et al. (2007). "Visible spectroscopic and photometric survey of Jupiter Trojans: Final results on dynamical families". *Icarus*, 190, 622.

Fraser, W. C., Kavelaars, J. J., Holman, M. J., et al. (2008). "The Kuiper belt luminosity from $m_R = 21$ to 26". *Icarus*, 195, 827.

Grav, T., Mainzer, A. K., Bauer, J. M., Masiero, J. R., & Nugent, C. R. (2012). "WISE/NEOWISE observations of the Jovian Trojan population: Taxonomy". *ApJ*, 759, 49.

Jewitt, D. C., Trujillo, C. A., & Luu, J. X. (2000). "Population and size distribution of small Jovian Trojan asteroids". *AJ*, 120, 1140.

Marzari, F., Frinella, P., Davis, D. R., Scholl, H., & Campo Bagatin, A. (1997). "Collision evolution of Trojan asteroids". *Icarus*, 125, 39.

Marzari, F. & Scholl, H. (1998). "Capture of Trojans by a growing proto-Jupiter". *Icarus*, 131, 41.

Melita, M. D., Licandro, J., Jones, D. C., & Williams, I. P. (2008). "Physical properties and orbital stability of the Trojan asteroids". *Icarus*, 195, 686.

Miyazaki, S., Komiyama, Y., Sekiguchi, M., & Okamura, S. (2002). "Subaru Prime Focus Camera – Suprime-Cam". *Publ. Astron. Soc. Japan*, 54, 833.

Morbidelli, A., Levison, H. F., Tsiganis, K., & Gomes, R. (2005). "Chaotic capture of Jupiter's Trojan asteroids in the early Solar System". *Nature*, 435, 462.

Nakamura, T. & Yoshida, F. (2008). "A new surface density model of Jovian Trojans around triangular libration points". *Publ. Astron. Soc. Japan*, 60, 293.

Nesvorný, D. & Morbidelli, A. (2012). "Statistical study of the early Solar System's instability with four, five, and six giant planets". *AJ*, 144, 117.

Peixinho, N., Delsanti, A., Guilbert-Lepoutre, A., Gafeira, R., & Lacerda, P. (2012). "The bimodal colors of Centaurs and small Kuiper Belt objects". *A&A*, 546, A86.

Pravec, P., Harris, A. W., & Michałowski, T. (2002). "Asteroid Rotations". In: *Asteroids III*. Eds. Bottke, W. F., Cellino, A., Paolicchi, P., & Binzel, R. P. (Tucson, AZ: University of Arizona Press), 113.

Roig, F., Ribeiro, A. O., & Gil-Hutton, R. (2008). "Taxonomy of asteroid families among the Jupiter Trojans: comparison between spectroscopic data and the Sloan Digital Sky Survey colors". *A&A*, 483, 911.

Szabó, Gy. M., Ivezić, Ž., Jurić, M., & Lupton, R. (2007). "The properties of Jovian Trojan asteroids listed in SDSS Moving Object Catalogue 3". *Mon. Not. R. Astron. Soc.* 377, 1393.

Tsiganis, K., Gomes, R., Morbidelli, A., & Levison, H. F. (2005). "Origin of the orbital architecture of the giant planets of the Solar System". *Nature*, 435, 459.

Wong, I., Brown, M. E., & Emery, J. P. (2014). "The differing magnitude distributions of the two Jupiter Trojan color populations". *AJ*, 148, 112.

Yang, B. & Jewitt, D. (2007). "Spectroscopic search for water ice on Jovian Trojan asteroids". *AJ*, 134, 223.

Yoshida, F. & Nakamura, T. (2005). "Size distribution of faint Jovian L4 Trojan asteroids". *AJ*, 130, 2900.

Yoshida, F. & Nakamura, T. (2008). "A comparative study of size distributions for small L4 and L5 Jovian Trojans". *Publ. Astron. Soc. Japan*, 60, 297.

Chapter 4

A HYPOTHESIS FOR THE COLOR BIMODALITY OF JUPITER TROJANS

Wong, I. & Brown, M. E. (2016). "A hypothesis for the color bimodality of Jupiter Trojans". *AJ*, 152, 90.

ABSTRACT

One of the most enigmatic and hitherto unexplained properties of Jupiter Trojans is their bimodal color distribution. This bimodality is indicative of two sub-populations within the Trojans, which have distinct size distributions. In this paper, we present a simple, plausible hypothesis for the origin and evolution of the two Trojan color sub-populations. In the framework of dynamical instability models of early solar system evolution, which suggest a common primordial progenitor population for both Trojans and Kuiper belt objects, we use observational constraints to assert that the color bimodalities evident in both minor body populations developed within the primordial population prior to the onset of instability. We show that, beginning with an initial composition of rock and ices, location-dependent volatile loss through sublimation in this primordial population could have led to sharp changes in the surface composition with heliocentric distance. We propose that the depletion or retention of H_2S ice on the surface of these objects was the key factor in creating an initial color bimodality. Objects that retained H_2S on their surfaces developed characteristically redder colors upon irradiation than those that did not. After the bodies from the primordial population were scattered and emplaced into their current positions, they preserved this primordial color bimodality to the present day. We explore predictions of the volatile loss model — in particular, the effect of collisions within the Trojan population on the size distributions of the two sub-populations — and propose further experimental and observational tests of our hypothesis.

4.1 Introduction

In the past decade, Jupiter Trojans have been the subject of increasing scientific interest, and understanding their origin and surface properties promises to unlock many of the fundamental aspects of solar system formation and evolution. These minor bodies share Jupiter's orbit around the Sun at 5.2 AU and reside in two clusters at the stable L4 and L5 Lagrangian points. One of the most important discoveries about the physical properties of Trojans is the existence of two sub-populations — the less-red (LR) and red (R) Trojans — whose members differ categorically with respect to several photometric and spectroscopic properties. Bimodality has been reported in visible and near-infrared colors (Szabó et al. 2007; Roig et al. 2008; Emery et al. 2011), as well as in longer wavelength reflectance (Grav et al. 2012). The two sub-populations are present in both the L4 and L5 swarms. Meanwhile, members of the only robustly attested collisional family within the Trojans — the Eurybates family at L4 (Brož & Rozehnal 2011) — all belong to the less-red sub-population (Fornasier et al. 2007), an observation that has important implications for the interplay between self-collisions and the surface properties of these objects.

While recent spectroscopic study in the near-infrared has detected water ice on the surfaces of some large Trojans, along with weaker absorption features possibly attributable to organics (Brown 2016), the overall surface compositions of Trojans remain poorly constrained. In particular, the color bimodality has no current explanation. Although some theories have been forwarded to produce the range of Trojan colors through ongoing processes such as surface gardening and/or various irradiation mechanisms (e.g., Melita et al. 2008), none of these theories predict a bimodality in color, instead yielding a single broad color distribution that is inconsistent with observations. On the basis of the differing spectral properties of LR and R Trojans, Emery et al. (2011) suggested that perhaps one of the two sub-populations formed in the Main Belt asteroid region, while the other formed in the outer Solar System before being captured by Jupiter.

Recent theories of solar system evolution, however, suggest that after an early dynamical instability between giant planets, the Jupiter Trojan region was filled exclusively with objects that formed at large heliocentric distances within an extended planetesimal disk situated beyond the primordial orbits of the ice giants (Morbidelli et al. 2005; Roig & Nesvorný 2015). In the context of these dynamical instability models, both LR and R Trojans must have originated from the same primordial population. To date, no hypothesis has been proposed to explain the existence of

two distinct sub-populations from a single source region.

Support for the idea of a shared formation environment for the Trojans and Kuiper Belt objects (KBOs) comes from the observation that the size distributions of Trojans and hot (i.e., dynamically excited) KBOs are consistent with each other (Fraser et al. 2014). In addition, the total Trojan size distribution for objects smaller than ∼100 km is consistent with collisional equilibrium (e.g., Marzari et al. 1997). Unexpectedly, however, the size distributions of the individual LR and R Trojan sub-populations are highly distinct; specifically, the power-law slopes of the magnitude distributions for objects smaller than ∼100 km in diameter are discrepant, revealing a monotonic increase in the relative number of LR Trojans with decreasing size (Wong et al. 2014; Wong & Brown 2015).

Such distinct size distributions are difficult to reconcile with the hypothesis that the Trojans share a single source population. However, Wong et al. (2014) demonstrated that, starting from an initial state where both sub-populations had identical magnitude distributions, a process wherein the collisional fragments of both R and LR Trojans become LR objects would naturally account for the relative depletion of R Trojans and the simultaneous enrichment of LR Trojans with decreasing size, as well as the collisional equilibrium of the overall population. While this explanation did not appeal to specific chemical or physical processes for the color conversion, the consistency between simulated and observed magnitude distributions suggests that R-to-LR conversion may provide a promising angle from which to address the question of the Trojans' color bimodality and the different LR and R size distributions.

In this paper, we propose a simple, chemically plausible hypothesis, developed within the framework of current dynamical instability models, to explain the origin of the color bimodality within the Trojans and the differing size distributions of the two color sub-populations. Central to our hypothesis is location-dependent volatile loss, which established sharp changes in *surface* composition and, thus, color across the primordial trans-Neptunian planetesimal disk prior to the onset of dynamical instability. In particular, we suggest that the loss or retention of H_2S due to sublimation resulted in two types of surface chemistry among objects in the primordial disk, subsequently leading to different characteristic colors upon irradiation. In Section 4.2, we briefly summarize the present understanding of both Trojan and KBO colors, which serves to motivate and constrain our hypothesis. The location-dependent volatile loss model is detailed in Section 4.3, and finally,

the predictions of our hypothesis with respect to surface colors, collisions, and size distributions are discussed in Section 4.4.

4.2 Colors of Trojans and KBOs

Recent dynamical instability models of the early Solar System posit a single primordial body of planetesimals from which the current Jupiter Trojans and KBOs are sourced. Therefore, the observed colors of both Trojans and KBOs are important in forming the foundational premise for the hypothesis developed in this paper, as well as establishing the range of phenomena that the hypothesis strives to explain.

Analyses of the visible spectral slopes of Trojans derived from Sloan Digital Sky Survey photometry reveal a color distribution with two peaks, corresponding to the LR and R sub-populations (Roig et al. 2008; Wong et al. 2014). The spectral slope distribution of Trojans brighter than $H = 12.3$ is shown in the bottom panel of Figure 4.1; the LR sub-population has colors centered around 5×10^{-5} Å^{-1}, while the R sub-population has a mean color of $\sim 10 \times 10^{-5}$ Å^{-1}. Aside from their differences in spectral properties, both LR and R Trojans have notably uniform low albedos averaging around 4% (e.g., Grav et al. 2012).

The color distribution of hot KBOs in the same size range as Trojans ($7.0 < H < 12.3$), compiled from spectral slopes listed in the MBOSS database (Hainaut et al. 2012), is shown in the top panel of Figure 4.1. In the middle panel, we also present the catalogued spectral slope data for similarly-sized Centaurs, which are former KBOs that have been scattered onto short-lived giant planet-crossing orbits. Many color measurements of KBOs and Centaurs in the literature have large uncertainties, and we have chosen to only include those measurements with uncertainties smaller than the bin size ($\sim 3 \times 10^{-5}$ Å^{-1}). In addition, we have omitted objects with inclinations less then 5° in order to remove the bulk of the cold classical KBOs. The cold classical KBOs are a population of low-inclination objects beyond 41 AU with physical properties that are markedly distinct from those observed across the rest of the Kuiper Belt (see, for example, the review by Brown 2012) and may have experienced a different formation and evolutionary history than the rest of the KBO population (e.g., Batygin et al. 2011). Given the possibility that the cold classical KBOs do not share the same progenitor population as the remainder of the KBOs and the Trojans, we do not consider them in the present work.

The color distributions of both KBOs and Centaurs have a notable peak at around 10×10^{-5} Å^{-1}, with spectral slopes extending to much higher values. An overabundance

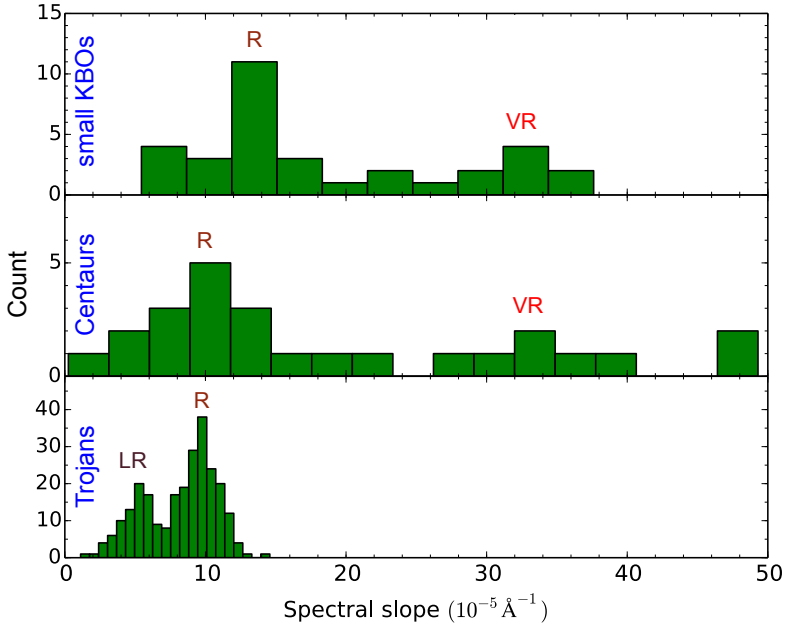

Figure 4.1: Histograms of the measured spectral slope values of small KBOs (top panel), Centaurs (middle panel), and Trojans (bottom panel). The small KBO and Centaur color distributions include only objects fainter than $H = 7$ and spectral slope uncertainties smaller than the bin size. Cold classical KBOs have been filtered out by omitting all KBOs with inclinations less than 5°. Color bimodalities are evident in all three minor body populations; they are labeled with their corresponding relative colors: less-red (LR), red (R), and very red (VR).

of spectral slopes higher than 30×10^{-5} Å^{-1} is discernible, suggesting an underlying bimodality in the KBO and Centaur color distributions. The bimodal nature of the Centaur color distributions has been thoroughly discussed in the literature (e.g., Peixinho et al. 2003; Barucci et al. 2005; Perna et al. 2010), and recent work has suggested a similar bimodality for small KBOs, i.e., KBOs in the same size range as that of the known Centaurs (e.g., Fraser & Brown 2012; Peixinho et al. 2012; Lacerda et al. 2014). It is therefore plausible that both (non cold classical) small KBOs and Centaurs are composed of two color sub-populations, hereafter referred to as the red (R) and very red (VR) KBOs and Centaurs. The color terminology has been chosen to reflect the relative colors of the various sub-populations, as shown in Figure 4.1. One important difference between the KBOs/Centaurs and Trojans is the albedo distribution. Both R KBOs and R Centaurs have very low albedos that are comparable with the Trojans (averaging around 4 – 6%), while VR KBOs and Centaurs are noticeably brighter, with mean albedos in range 11 – 12% (e.g.,

Stansberry et al. 2006; Fraser et al. 2014).

Importantly, no correlation between color and any dynamical or orbital parameter has been found in either the Trojans (Fornasier et al. 2007; Melita et al. 2008; Emery et al. 2011) or the KBOs (e.g., Morbidelli & Brown 2004; Doressoundiram et al. 2008). This indicates that the observed color bimodalities cannot be attributed to the local conditions at different locations within the Trojan and Kuiper Belt regions. The lack of correspondence between color and present-day environment points toward the color bimodality being primordial (i.e., already present when the Trojans and KBOs were emplaced in their current locations).

4.3 Volatile loss model

Within the dynamical instability model, the observation that Trojans, Centaurs, and small KBOs all appear to have a bimodal color distribution that is not attributable to any aspect of the populations' current orbital/dynamical architecture suggests that the color bimodality developed early on within the primordial trans-Neptunian planetesimal disk. Large solid bodies that formed in this region moved through the disk as they accreted mass, thereby incorporating materials from diverse regions (e.g., Kenyon et al. 2008). As a result, chemical gradients that existed in the disk initially were averaged over in the macroscopic bodies, whose bulk compositions would then reflect a mix of materials found throughout the disk. In light of this, a possible explanation for a color bimodality within the primordial disk (as opposed to a smooth gradient) is a physical process that results in sharp divisions in the surface chemistry of objects, regardless of any variations in the bulk composition across the primordial planetesimal disk.

In our hypothesis, we follow previous work on the surface colors of KBOs (Brown et al. 2011) by positing that the sublimation of volatile ices can yield sharp changes in the surface chemistry of objects as a function of formation location. Objects that formed in the primordial planetesimal disk were accreted out of a mix of rocky material and ice, including many volatile ices. We take this as the initial composition of objects in our model. Objects closer in to the Sun had higher surface temperatures and correspondingly higher volatile loss rates, and after some time, their surfaces would become depleted in the more volatile species. Meanwhile, objects that formed farther away would have retained the more volatile molecules on their surfaces.

We update the results of Brown et al. (2011) in two important ways. First, the objects that we consider here have diameters less than 250 km; this limit roughly

corresponds to the size of the largest Trojan (624 Hektor). Due to their relatively small size, these objects would not have sustained a bound atmosphere that could act as a buffer against volatile loss. Quantitatively, this means that the value of the Jeans parameter (i.e., ratio of the escape velocity to the thermal energy of a gas molecule in an atmosphere) is much less than unity for all Trojans, assuming any plausible atmospheric composition and across all temperatures in the middle and outer Solar System. Second, we correct numerical errors in the Brown et al. (2011) vapor pressures. We quantitatively model volatile loss via direct sublimation from a surface into vacuum. For a volatile ice species i with molecular mass m_i, the rate of mass loss per unit surface area is directly related to the vapor pressure p_i by the relation (e.g., Wallis & MacPherson 1981)

$$\dot{m}_i = p_i \sqrt{\frac{m_i}{2\pi k T}}, \tag{4.1}$$

where k is the Boltzmann constant, and T is the blackbody temperature of the surface in equilibrium with incident solar irradiation, assuming reradiation across the entire surface: $T \equiv \left(S_0(1-A)/4\sigma a^2\right)^{1/4}$. Here, σ is the Stefan-Boltzmann constant, A is the albedo, a is the heliocentric distance in AU, and $S_0 = 958$ W/m^2 is the solar irradiance at 1 AU, assumed at this early stage of solar system evolution to be 70% of its current value (Gough 1981). We use vapor pressures for each ice species as computed by Fray & Schmitt (2009).

While the typical albedo of these objects after surface radiation processing is very low, as reflected by present-day observations, it is expected that these icy bodies were initially brighter. With a surface composition composed of primarily water ice and rocky material (see below), the initial albedo would likely have exceeded 0.5. Through irradiation, the surface was continuously altered, reddening and darkening as described in Section 4.4. Meanwhile, the active collisional environment of the early Solar System produced a steady gardening of the surface, exposing brighter pristine and unirradiated material from the interior. Therefore, in our modeling, we chose arbitrary intermediate values between the current albedo and the expected initial albedo. For the results shown in this paper, we have assumed $A = 0.2$; changes to the assumed albedo by factors of $2-3$ in either direction do not substantially affect the general conclusions of the model.

The time t_i needed to deplete a surface layer with thickness x of a particular volatile ice species is given by

$$t_i = \frac{\rho \eta \beta_i x}{\dot{m}_i}, \tag{4.2}$$

where ρ is the bulk density of the object, η is the fraction of the object's mass that is ice, and β_i is the abundance of the volatile ice i relative to water ice. The rate of sublimation is a steep exponential function of temperature, and therefore, most model parameters have little impact on the final result.

Spectroscopic studies of Trojans have revealed features indicative of both water ice (Brown 2016) and fine-grained silicates (Emery et al. 2006) on the surface. For the calculations presented here, we have assumed $\rho = 1.0$ g/cm^3, which is comparable to the measured Trojan densities in the literature (e.g., $0.8^{+0.2}_{-0.1}$ g/cm^3 for 617 Patroclus; Marchis et al. 2006). This low density suggests a significant ice fraction, as well as high porosity. In this paper, we present results for the case of $\eta = 0.5$ to represent an ice-to-rock ratio of unity. We note that using $\eta = 1$ instead, corresponding to a 100% ice fraction, does not have a noticeable impact on the results.

Objects that formed in the primordial trans-Neptunian disk would have accreted with a roughly cometary composition, with rocky material and a wide variety of volatile ices. Published spectra of Trojans have hitherto not revealed any incontrovertible features except for some water ice absorption; meanwhile, obtaining high quality spectra of similarly sized Centarus and KBOs is difficult. Instead, we can use the detailed measured ice compositions of short-period comets as a proxy for the volatile component of these primordial planetesimals from the outer Solar System. In our model, we consider all volatile ice species with average measured abundances relative to water greater than 0.5% as reported from comet comae measurements (Bockelée-Morvan et al. 2004) — CH_3OH, NH_3, CO_2, H_2S, C_2H_6, CO, and CH_4. We set all initial relative volatile ice abundances to $\beta_i = 0.01$. We note in passing that many of these volatile ices, or the irradiation products thereof, have been detected on some of the larger KBOs (see Brown 2012; Barucci et al. 2008 and references therein), so they are expected to have accreted onto the smaller primordial bodies in this region as well.

The thickness parameter x must reflect the amount of depletion needed in order to effect a change in the surface chemistry and its response to irradiation. While the final color of an object depends only on the chemistry of the topmost layers, in an early solar system environment characterized by frequent collisions, gardening and minor impacts constantly excavated the surface, exposing interior material to irradiation. Meanwhile, even kilometer-sized short-period comets have measurable amounts of highly volatile ices such as CO, indicating that volatile ices in the interior of these objects (deeper than ~1 km) are protected from sublimation.

The thickness of the surface layer that must be depleted is equal to the depth to which material is excavated through collisional activity. We estimate this by extrapolating the results from collisional modeling of the current Kuiper Belt to the expected conditions within the primordial trans-Neptunian disk. Durda et al. (1998) computed collision rates and the effect of minor impacts on the surface of present-day KBOs and demonstrated that the cumulative fraction of the surface area of 2 to 200 km diameter objects cratered by impactors of radius greater than 4 m ranges from a few to a few tens of percent over ∼4 Gyr. For reasonable assumptions of the surface material properties, they show that such impacts are expected to excavate down to a depth of at least 40 − 50 m.

The number of objects in the primordial trans-Neptunian region prior to the onset of dynamical instability is expected to have exceeded the current KBO population by roughly two orders of magnitude (e.g., Tsiganis et al. 2005). Therefore, we expect that, in the period before the disruption of the primordial trans-Neptunian planetesimal disk (see below), all objects in the observable size range for Trojans would have had their entire surface reworked through collisions. Many of the cratering events would have been caused by impactors significantly larger than tens of meters in diameter, so a significant fraction of the impacts would have exposed material to a depth of many hundreds of meters or more. In this paper, we have taken $x = 100$ m to be the thickness of the surface layer that is affected by these impacts.

The relevant timescale for our model is the irradiation timescale, i.e., the time required for incident radiation to change in the properties of the surficial material. Experiments on volatile ices have demonstrated that the effects of irradiation depend primarily on the total energy deposited and saturate after a certain energy threshold is reached. In the context of surface colors, only the top ∼1 μm of the surface material is sampled by visible and near-infrared observations. Hudson et al. (2008) estimated that the radiation dose at ∼1 μm depth for objects at 20 AU (roughly the center of the primordial disk in canonical simulations of dynamical instability models) is 1000 − 10000 eV/16 amu over the lifetime of the Solar System. Using the saturation doses for volatile ice irradiation reported by Brunetto et al. (2006) (100 − 300 eV/16 amu), we arrive at estimates of the irradiation timescale between 50 Myr and 1 Gyr. In this paper, we set the irradiation timescale at 100 Myr; values differing by an order of magnitude in either direction do not yield qualitatively different conclusions.

The canonical version of current dynamical instability models aligns the onset of instability with the Late Heavy Bombardment, which occurred ~650 Myr after the formation of the Solar System (Gomes et al. 2006). Comparing this estimated disk lifetime to our choice of irradiation timescale, we find that irradiation processing is expected to have proceeded to saturation prior to the scattering of the primordial disk.

Figure 4.2 shows the time needed to deplete the top 100 m of an object of various volatile ice species, as a function of heliocentric distance. The curves denote sublimation lines: objects that formed closer than a line would have surfaces depleted of the corresponding volatile ice species, while objects that formed farther would have retained it. Simulations of early solar system evolution predict an initially compact planetary configuration, with a planetesimal disk beyond the orbit of the outermost ice giant extending from 15 AU to about 30 AU, indicated in the figure by the green band (Tsiganis et al. 2005; Levison et al. 2008). CH_3OH, NH_3, and to a certain extent CO_2 are involatile throughout the entire primordial disk. (We note that the suggestion in Brown et al. (2011) that CH_3OH had a sublimation line within the primordial planetesimal disk was mainly a result of a numerical error in their vapor pressures.) Objects in the inner part of the disk have surfaces depleted in H_2S after an elapsed time comparable to the irradiation timescale of 100 Myr, while objects in the outer part retain H_2S. The farthest most objects also retain C_2H_6. The sublimation lines for CO and CH_4 are located at much larger heliocentric distances, out of the range shown in Figure 4.2.

4.4 Surface colors

For a wide range of assumptions, volatile loss in the primordial planetesimal disk would have occurred as shown in Figure 4.2. Given the sublimation-driven surface chemistry developed by the model in the previous section, we now consider the effects of radiation processing on the surface properties and examine the predictions of our hypothesis with respect to the surface colors of Trojans and KBOs.

Surface radiation processing

Objects throughout the primordial disk retained methanol, ammonia, and carbon dioxide ices on their surfaces. While no laboratory experiments have studied the effects of irradiation on analogous surfaces, Brunetto et al. (2006) demonstrated that the irradiation of single-component methanol ice yields a darkened and moderately-reddened irradiation crust composed of organic residue, with spectral slopes in

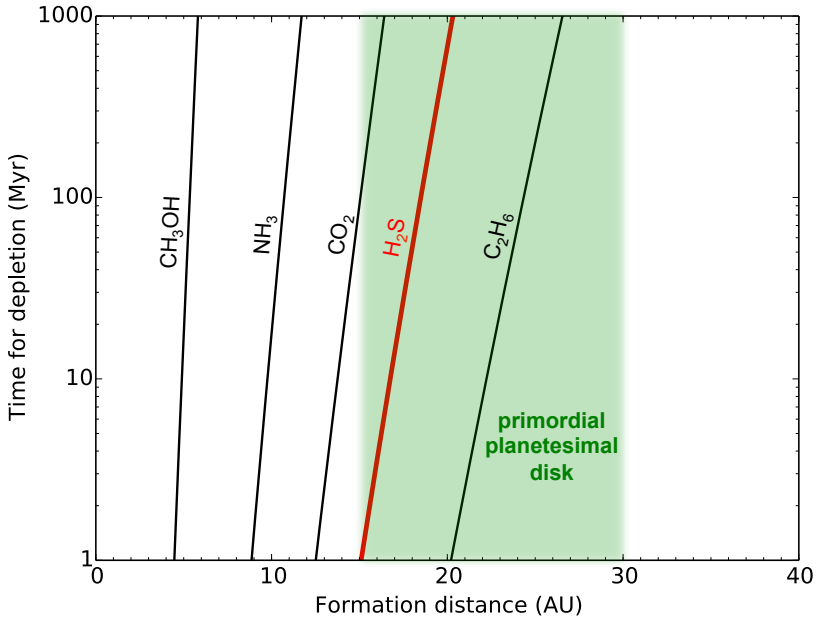

Figure 4.2: Sublimation lines in the early Solar System, as a function of formation distance. Objects located to the left of a line have the respective volatile ice species depleted from a 100 m layer at the surface after the corresponding elapsed time on the y-axis, while objects located to the right of a line have retained the respective volatile ice species on the surface. The approximate location of the pre-instability primordial planetesimal disk is depicted by the green band. Notably, the H_2S sublimation line (in red) passes through the region of the primordial disk.

the visible through the near-infrared comparable to values measured for many R KBOs and Centaurs. We therefore propose that the presence of methanol ice on the surface is the primary factor that led to surface colors characteristic of R objects upon irradiation. It is interesting to note that methanol is the only involatile molecule other than water that has been identified in the spectrum of either a centaur (Cruikshank et al. 1998) or a KBO (Barucci et al. 2006; Barucci et al. 2011; Brown 2012).

Objects farther out in the primordial disk additionally retained H_2S on their surfaces. Irradiation studies of sulfur-bearing ices have found that among the stable irradiation products are long-chained sulfur molecules (e.g., Moore 1984; Cassidy et al. 2010), which produce a dark residue and have been interpreted, for example, as the cause of the darkened, intensely red deposits found on Io (Carlson et al. 2007). Within the framework of our hypothesis, we propose that the retention of H_2S on the surface of objects in the outer primordial disk contributed to a significant additional

reddening, leading to the VR colors. The only remaining sublimation line in the region of the primordial planetesimal disk is C_2H_6. Experiments on mixtures of water ice and ethane ice yield similar irradiation products as mixtures with methanol or carbon dioxide ice (e.g., complex hydrocarbons Moore & Hudson 1998; Hudson et al. 2009), so it is not expected that the addition of ethane ice on the surface would entail any notable alterations in the surface color.

We have forwarded a speculative explanation for the development of a primordial color bimodality within the primordial planetesimal disk, with the depletion vs. retention of H_2S ice on the surface as the main distinguishing factor between R and VR objects, respectively. This process is outlined in panels a and b of Figure 4.3. We note that while the overall darkening of primordial disk objects upon irradiation is predicted by the hypothesis, the different albedos of R and VR KBOs and Centaurs (see Section 4.2) remains unexplained here, since experimental data of analogous surfaces do not exist so as to allow any comparison between cases with and without H_2S.

Emplacement

The next step in the evolution of the primordial disk is the period of dynamical instability, during which a portion of the objects was scattered outward to populate the present-day Kuiper Belt. Given that the color alteration caused by irradiation is likely to have proceeded to saturation within the primordial disk (see Section 4.3), we expect that the colors of the irradiation mantles on KBOs have remained unchanged in the roughly 4 Gyr that has elapsed since these objects were emplaced in their current orbits beyond 30 AU. The average surface temperature on KBOs that scatter inward to become Centaurs do not markedly increase beyond those that were experienced early on in the primordial disk, so their surfaces are not expected to evolve significantly, thus providing an explanation of the statistically identical color distribution of KBOs and Centaurs (Section 4.2).

According to dynamical instability models, a portion of the primordial disk was scattered inward and later captured by Jupiter to become the present-day Trojans (Morbidelli et al. 2005; Roig & Nesvorný 2015). We recall from Figure 4.1 that the LR and R Trojan color modes are situated at relatively more neutral colors than the two color modes in the KBOs and Centaurs. The conditions at 5.2 AU are characterized by higher surface temperatures and more intense irradiation than the conditions in the primordial planetesimal disk and may have altered the chemistry

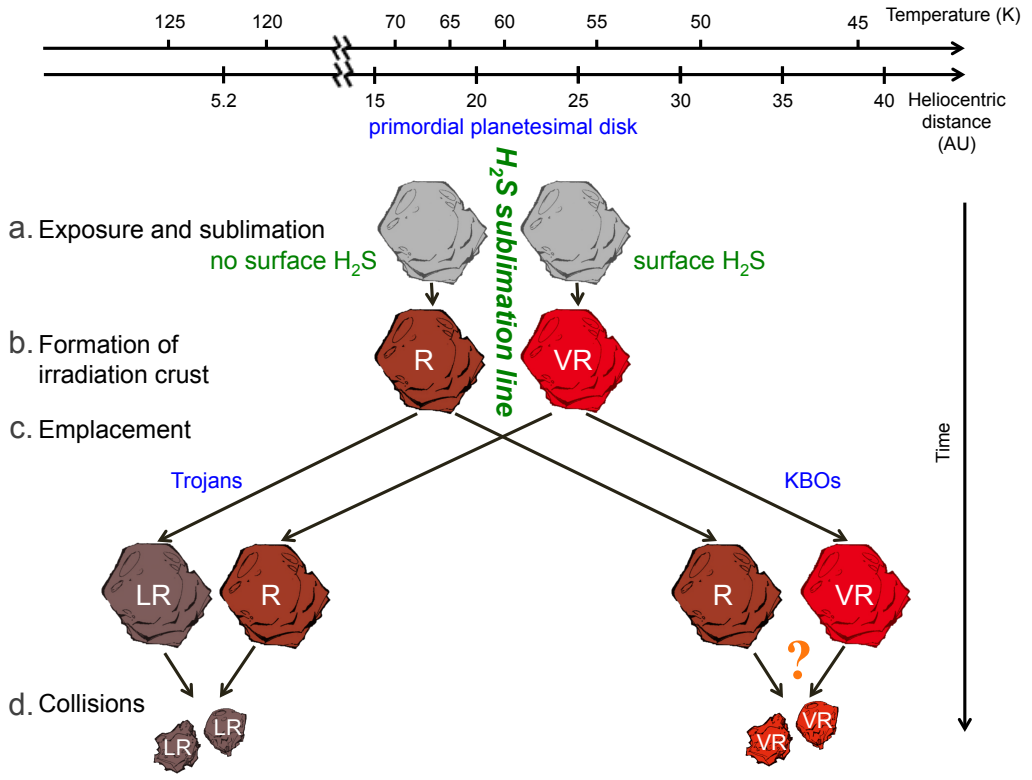

Figure 4.3: Pictoral representation of the hypothesis presented in this paper and the major predictions thereof. Panel a depicts the initial state of bodies within a primordial planetesimal disk extending from 15 AU to roughly 30 AU at the moment when the nebular gas dispersed and the objects were first exposed to sunlight. Each body was composed of a pristine mix of rocky material and ices; volatile ice sublimation began. Panel b illustrates the development of the primordial R and VR colors: Objects that formed inside of the H_2S sublimation line were depleted in H_2S after ~100 Myr and formed a dark, reddish irradiation crust (due primarily to retained methanol). Meanwhile, objects that formed farther out beyond the H_2S sublimation line retained H_2S on their surfaces and thus developed a much redder coloration. The emplacement of Trojans and KBOs during the Nice model dynamical instability is denoted in panel c. We expect that the primordial R and VR objects became R and VR KBOs and Centaurs, respectively, while the Trojans experienced surface color evolution, maintaining the initial color bimodality but resulting in relatively less red colors. Panel d describes the result of collisions in the current Trojan and KBO populations: The surfaces of Trojan collisional fragments of Trojans become depleted in all volatile ice species, thereby becoming LR objects. Although no observational evidence exists at present, we propose that the collisional fragments of small KBOs likely retain H_2S on their surfaces, eventually developing into VR objects.

and physical properties of the irradiation mantle. Experiments simulating the effect of long-term irradiation on complex refractory organic residues (similar to the final irradiation products in methanol ice studies) have shown that at high radiation doses and temperatures, carbonization of the surface begins, which produces an overall neutralizing and darkening effect on the surface (e.g., Moroz et al. 2004). This process could explain the alteration in surface colors of Trojans upon emplacement, predicting that the primordial R and VR objects become LR and R Trojans, respectively. Panel c in Figure 4.3 illustrates the emplacement process of both Trojans and KBOs.

Collisions

Lastly, we use our hypothesis to speculate on the result of mutual collisions within the Trojan and KBO populations since emplacement. When two Trojans are involved in a shattering collision, the thin irradiation crust on the surface of both objects is destroyed. The surface composition of the resultant fragments thus corresponds to the interior composition of Trojans, i.e., a mixture of water ice and rocky material, along with volatile ices that were shielded from sublimation at depth. At the current Trojan surface temperature of 120 – 125 K, all the volatile ice species on the surface rapidly sublimate away, leaving behind only water ice and the rocky component. (Recall that the sublimation lines in Figure 4.2 are assuming 70% of current solar flux. The present methanol sublimation line is located ~3 AU farther from the Sun, well away from the Trojan region.) Without either CH_3OH or H_2S present on the surface, subsequent irradiation would not produce the characteristic R and VR colors that developed in the more distant primordial disk, and the resulting colors would be relatively less-red. Starting from an initially neutral surface, with likely higher albedo than the uncollided Trojans, space weathering processes would probably proceed in a similar fashion to scenarios reported for other middle solar system bodies, e.g., darkening and reddening of the spectrum via nanophase iron on silicate grains (e.g., Bennett et al. 2013).

The previous discussion provides the chemical basis for the R-to-LR conversion argument proposed in Wong et al. (2014) and described in the Introduction. The collisional probability is inversely proportional to object size, which leads to an increase in the fraction of objects that are collisional fragments with decreasing size. All of the collisional fragments in the Trojan population are depleted in CH_3OH and H_2S, so regardless of whether the parent bodies are R and LR Trojans, the resulting fragments become LR objects. Therefore, the observed increase in

LR-to-R number ratio with decreasing size is a natural outcome of the hypothesis outlined in this paper. The effect of collisions on Trojan colors is illustrated in panel d of Figure 4.3.

An interesting prediction of our hypothesis is that the fragments from shattering collisions may constitute a third color sub-population of neutral objects. The only robustly attested collisional family in the Trojans, the Eurybates family, appears to be unique in having members that are exceptionally neutral (e.g., Fornasier et al. 2007), in line with the prediction of our hypothesis. One might imagine that the eventual colors of Trojan collisional fragments, with surfaces completely depleted of volatile ices, may be distinct from the colors of uncollided LR Trojans, which arose from the evolution of primordial R (or possibly VR) objects emplaced during the dynamical instability. Further measurements of the colors and albedos of collisional fragments and smaller Trojans in general promise to provide a powerful observational test for the details of the R-to-LR conversion model.

The relatively low intrinsic collisional probability of Trojans means that shattering impacts on objects larger than a few tens of km in diameter are rare. More common are sub-catastrophic, cratering collisions, which garden the surface and can potentially excavate primordial, neutral-colored, unirradiated material from the interior. The collisional probability and impact velocities within the Trojan swarms are comparable to those found in the main belt (e.g., Marzari et al. 1997), which in turn have been shown to yield a similar level of collisional activity as in the current Kuiper Belt (Durda et al. 1998). Since the thickness of the surface layers that was altered by irradiation prior to emplacement is on the order of $x = 100$ m, impacts would need to excavate through a depth greater than x in order to expose pristine interior material. Using the results from Durda et al. (1998), we can expect that the cumulative surface fraction of Trojans that has been excavated past a depth of $\sim$100 m is at most a few tens of percent. We therefore conclude that the current level of collisional activity is insufficient to yield significant resurfacing and exposure of primordial material. The minor gardening within the Trojan population may contribute, as a secondary effect, to the dispersion of colors within each of the LR and R sub-populations.

At present, color measurements in the Kuiper Belt have not yet probed to the sizes of collisional fragments. Nevertheless, within the framework of our hypothesis, it is possible to speculate on the consequences of mutual collisions between small planetesimals within the Kuiper Belt. Upon shattering, the fragments from such

a KBO collision would expose the interior composition of the objects — water ice, rocky material, and all the volatile ice species that were present during the initial accretion. Unlike in the case of Trojans, the KBOs are currently in a colder environment. Crucially, throughout the entire Kuiper Belt ($a > 30$ AU), our volatile loss model predicts that H_2S is involatile. Therefore, all KBO collisional fragments would retain H_2S on their surfaces. We expect that after an initial state with pristine unirradiated ice on the surface, with likely higher albedo and a relatively neutral color, the total received photon and solar wind flux on the surfaces of these collisional fragments will turn them VR. In essence, these collisional fragments should evolve in an analogous way to the H_2S-retaining planetesimals in the primordial trans-Neptunian region, as discussed in Section 4.3. We note that the fragments from the only known KBO collisional family to date — the Haumea family — came from the already volatile-depleted icy mantle of a large differentiated dwarf planet (Brown et al. 2007), so they do not follow this proposed pattern.

4.5 Conclusion

We have proposed a simple hypothesis for the two color sub-populations within the Trojans. The main feature of our proposal is location-dependent sublimation of volatile ices within a primordial planetesimal disk in the outer Solar System, which divided objects in this region into two groups — those that retained H_2S on their surfaces, and those that did not. As a result of irradiation chemistry on these initially pristine icy surfaces, these two groups developed different involatile surface colors, thereby imprinting an initial color bimodality into the population. The retention of H_2S on the surface acted as a significant reddening agent upon irradiation, leading to characteristically redder colors than in the face of H_2S-depleted surfaces. Following a period of dynamical instability, the objects in this primordial disk were scattered throughout the middle and outer Solar System, carrying the primordial color bimodality with them as they populated the Trojan region and the current Kuiper Belt. Our hypothesis thus offers a chemically and dynamically plausible explanation for the color bimodality of both Trojans and KBOs, as summarized in Figure 4.3. In addition, our model predicts that all collisional fragments in the Trojan swarms are compositionally identical and become relatively less-red upon irradiation, regardless of whether the parent body is a LR or a R object. Therefore, our hypothesis accounts for the relative depletion of R objects with decreasing size and offers a self-consistent explanation for the discrepancy between the observed LR and R Trojan size distributions.

Although it is supported by observational constraints and some experimental studies, the hypothesis advanced here is necessarily speculative. The most fruitful pathway for follow-up study would be systematic laboratory experiments that analyze the effects of irradiation on the color and reflectivity of surfaces analogous to the ones described in our hypothesis — water ice-dominated mixtures of methanol, ammonia, and carbon dioxide ice, with or without the addition of H_2S ice. Crucially, these experiments must simulate the changing environments of Trojans and KBOs as they evolve within the primordial planetesimal disk and then are emplaced in their respective current locations. The main results that must be obtained in the experimental context for our hypothesis to be true are as follows: (1) Irradiation of ice mixtures with methanol, ammonia, and carbon dioxide, but without H_2S, leads to reduction of albedo and a surface residue that has a color comparable to those seen on R KBOs and Centaurs. (2) Irradiation of ice mixtures with the addition of H_2S leads to reduction of albedo and a significantly redder irradiation mantle than in the absence of H_2S. (3) Intensified irradiation and higher temperatures alter the surface colors to those characteristic of Trojans. While some of these results are supported by laboratory data in the literature, only experimental verification using a uniform setup and conditions appropriate to the various minor body populations will allow us to confirm or refute the hypothesis for the color bimodality of Trojans presented here.

References

Barucci, M. A., Alvarez-Candal, A., Merlin, F., & Belskaya, I. N. (2011). "New insights on ices in Centaur and Transneptunian populations". *Icarus*, 214, 297.

Barucci, M. A., Belskaya, I. N., Fulchignoni, M., & Birlan, M. (2005). "Taxonomy of Centaurs and trans-Neptunian objects". *AJ*, 130, 1291.

Barucci, M. A., Brown, M. E., Emery, J. P., & Merlin, F. (2008). "Composition and Surface Properties of Transneptunian Objects and Centaurs". In: *The Solar System Beyond Neptune*. Eds. Barucci, M. A., Boehnhardt, H., Cruikshank, D. P., Morbidelli, A., & Dotson, R. (Tucson, AZ: University of Arizona Press), 143.

Barucci, M. A., Merlin, F., Dotto, E., & Doressoundiram, A. (2006). "TNO surface ices. Observations of the TNO 55638 (2002 VE_{95})". *A&A*, 455, 725.

Batygin, K., Brown, M. E., & Fraser, W. C. (2011). "Retention of a primordial cold classical Kuiper Belt in an instability-driven model of solar system formation". *ApJ*, 738, 13.

Bennett, C. J., Pirim, C., & Orlando, T. M. (2013). "Space-weathering of solar system bodies: A laboratory perspective". *Chem. Rev.* 113, 9086.

Bockelée-Morvan, D., Crovisier, J., Mumma, M. J., & Weaver, H. A. (2004). "The Composition of Cometary Volatiles". In: *Comets II*. Eds. Festou, M. C., Keller, H. U., & Weaver, H. A. (Tucson, AZ: University of Arizona Press), 391.

Brown, M. E. (2012). "The compositions of Kuiper Belt objects". *Annual Rev. of Earth and Planetary Sci.* 40, 467.

Brown, M. E. (2016). "The $3-4$ μm spectra of Jupiter Trojans asteroids". *AJ*, 152, 159.

Brown, M. E., Barkume, K. M., Ragozzine, D., & Schaller, E. L. (2007). "A collisional family of icy objects in the Kuiper belt". *Nature*, 446, 294.

Brown, M. E., Schaller, E. L., & Fraser, W. C. (2011). "A hypothesis for the color diversity of the Kuiper belt". *ApJ*, 739, L60.

Brož, M. & Rozehnal, J. (2011). "Eurybates – the only asteroid family among Trojans?" *Mon. Not. R. Astron. Soc.* 414, 565.

Brunetto, R., Barucci, M. A., Dotto, E., & Strazzulla, G. (2006). "Ion irradiation of frozen methanol, methane, and benzene: Linking to the colors of Centaurs and trans-Neptunian objects". *ApJ*, 644, 646.

Carlson, R. W., Kargel, J. S., Douté, S., Soderblom, L. A., & Brad Dalton, J. (2007). "Io's Surface Composition". In: *Io After Galileo*. Eds. Lopes, R. M. C. & Spencer, J. R. (Chichester, UK: Praxis Publishing Ltd), 194.

Cassidy, T., Coll, P., Raulin, F., & Carlson, R. W. (2010). "Radiolysis and photolysis of icy satellite surfaces: Experiments and theory". *Space Sci. Rev.* 153, 299.

Cruikshank, D. P., Roush, T. L., Bartholomew, M. J., & Geballe, T. R. (1998). "The composition of Centaur 5145 Pholus". *Icarus*, 135, 389.

Doressoundiram, A., Boehnhardt, H., Tegler, S. C., & Trujillo, C. (2008). "Color Properties and Trends of the Transneptunian Objects". In: *The Solar System Beyond Neptune*. Eds. Barucci, M. A., Boehnhardt, H., Cruikshank, D. P., Morbidelli, A., & Dotson, R. (Tucson, AZ: University of Arizona Press), 91.

Durda, D. D., Greenberg, R., & Jedicke, R. (1998). "Collisional models and scaling laws: A new interpretation of the shape of the main-belt asteroid size distribution". *Icarus*, 135, 431.

Emery, J. P., Burr, D. M., & Cruikshank, D. P. (2011). "Near-infrared spectroscopy of Trojan asteroids: Evidence for two compositional groups". *AJ*, 141, 25.

Emery, J. P., Cruikshank, D. P., & Van Cleve, J. (2006). "Thermal emission spectroscopy ($5.2-38$ μm) of three Trojan asteroids with the Spitzer Space Telescope: Detection of fine-grained silicates". *Icarus*, 182, 496.

Fornasier, S., Dotto, E., Hainaut, O., et al. (2007). "Visible spectroscopic and photometric survey of Jupiter Trojans: Final results on dynamical families". *Icarus*, 190, 622.

Fraser, W. C. & Brown, M. E. (2012). "The Hubble Wide Field Camera 3 test of surfaces in the outer Solar System: The compositional classes of the Kuiper Belts". *ApJ*, 749, 33.

Fraser, W. C., Brown, M. E., Morbidelli, A., Parker, A., & Batygin, K. (2014). "The absolute magnitude distribution of Kuiper Belt objects". *ApJ*, 782, 100.

Fray, N. & Schmitt, B. (2009). "Sublimation of ices of astrophysical interest: A bibliographic review". *Planet. Space Sci.* 57, 2053.

Gomes, R., Levison, H. F., Tsiganis, K., & Morbidelli, A. (2006). "Origin of the cataclysmic Late Heavy Bombardment period of the terrestrial planets". *A&A*, 455, 725.

Gough, D. O. (1981). "Solar interior structure and luminosity variations". *Sol. Phys.* 74, 21.

Grav, T., Mainzer, A. K., Bauer, J. M., Masiero, J. R., & Nugent, C. R. (2012). "WISE/NEOWISE observations of the Jovian Trojan population: Taxonomy". *ApJ*, 759, 49.

Hainaut, O. R., Boehnhardt, H., & Protopapa, S. (2012). "Colours of minor bodies in the outer solar system. II. A statistical analysis revisited". *A&A*, 546, A115.

Hudson, R. L., Moore, M. H., & Raines, L. L. (2009). "Ethane ices in the outer Solar System: Spectroscopy and chemistry". *Icarus*, 203, 677.

Hudson, R. L., Palumbo, M. E., Strazzula, G., & Moore, M. H. (2008). "Laboratory studies of the chemistry of Transneptunian object surface materials". In: *The Solar System Beyond Neptune*. Eds. Barucci, M. A., Boehnhardt, H., Cruikshank, D. P., Morbidelli, A., & Dotson, R. (Tucson, AZ: University of Arizona Press), 507.

Kenyon, S. J., Bromley, B. C., O'Brien, D. P., & Davis, D. R. (2008). "Formation and collisional evolution of Kuiper Belt objects". In: *The Solar System Beyond Neptune*. Eds. Barucci, M. A., Boehnhardt, H., Cruikshank, D. P., Morbidelli, A., & Dotson, R. (Tucson, AZ: University of Arizona Press), 293.

Lacerda, P., Fornasier, S., Lellouch, E., & Kiss, C. (2014). "The albedo-color diversity of Transneptunian objects". *ApJ*, 793, L2.

Levison, H. F., Morbidelli, A., Van Laerhoven, C., & Gomes, R. (2008). "Origin of the structure of the Kuiper belt during a dynamical instability in the orbits of Uranus and Neptune". *Icarus*, 196, 258.

Marchis, F., Hestroffer, D., Descamps, P., & Berthier, J. (2006). "A low density of 0.8 g cm^{-3} for the Trojan binary asteroid 617 Patroclus". *Nature*, 439, 565.

Marzari, F., Frinella, P., Davis, D. R., Scholl, H., & Campo Bagatin, A. (1997). "Collision evolution of Trojan asteroids". *Icarus*, 125, 39.

Melita, M. D., Licandro, J., Jones, D. C., & Williams, I. P. (2008). "Physical properties and orbital stability of the Trojan asteroids". *Icarus*, 195, 686.

Moore, M. H. (1984). "Studies of proton-irradiated SO_2 at low temperatures: Implications for Io". *Icarus*, 59, 114.

Moore, M. H. & Hudson, R. L. (1998). "Infrared study of ion-irradiated water-ice mixtures with hydrocarbons relevant to comets". *Icarus*, 135, 518.

Morbidelli, A. & Brown, M. E. (2004). "The Kuiper Belt and the Primordial Evolution of the Solar System". In: *Comets II*. Eds. Festou, M. C., Keller, H. U., & Weaver, H. A. (Tucson, AZ: University of Arizona Press), 175.

Morbidelli, A., Levison, H. F., Tsiganis, K., & Gomes, R. (2005). "Chaotic capture of Jupiter's Trojan asteroids in the early Solar System". *Nature*, 435, 462.

Moroz, L., Baratta, G., Strazzulla, G., Starukhina, L., & Dotto, E. (2004). "Optical alteration of complex organics induced by ion irradiation: 1. Laboratory experiments suggest unusual space weathering trend". *Icarus*, 170, 214.

Peixinho, N., Delsanti, A., Guilbert-Lepoutre, A., Gafeira, R., & Lacerda, P. (2012). "The bimodal colors of Centaurs and small Kuiper Belt objects". *A&A*, 546, A86.

Peixinho, N., Doressoundiram, A., Delsanti, A., & Boehnhardt, H. (2003). "Reopening the TNOs color controversy: Centaurs bimodality and TNOs unimodality". *A&A*, 410, L29.

Perna, D., Barucci, M. A., Fornasier, S., & DeMeo, F. E. (2010). "Colors and taxonomy of Centaurs and trans-Neptunian objects". *A&A*, 510, A53.

Roig, F. & Nesvorný, D. (2015). "The evolution of asteroids in the jumping-Jupiter migration model". *AJ*, 150, 186.

Roig, F., Ribeiro, A. O., & Gil-Hutton, R. (2008). "Taxonomy of asteroid families among the Jupiter Trojans: comparison between spectroscopic data and the Sloan Digital Sky Survey colors". *A&A*, 483, 911.

Stansberry, J. A., Grundy, W. M., & Margot, J. L. (2006). "The albedo, size, and density of binary Kuiper Belt object (47171) 1999 TC_{36}". *ApJ*, 643, 556.

Szabó, Gy. M., Ivezić, Ž., Jurić, M., & Lupton, R. (2007). "The properties of Jovian Trojan asteroids listed in SDSS Moving Object Catalogue 3". *Mon. Not. R. Astron. Soc.* 377, 1393.

Tsiganis, K., Gomes, R., Morbidelli, A., & Levison, H. F. (2005). "Origin of the orbital architecture of the giant planets of the Solar System". *Nature*, 435, 459.

Wallis, M. K. & MacPherson, A. K. (1981). "On the outgassing and jet thrust of snowball comets". *A&A*, 98, 45.

Wong, I. & Brown, M. E. (2015). "The color-magnitude distribution of small Jupiter Trojans". *AJ*, 150, 174.

Wong, I., Brown, M. E., & Emery, J. P. (2014). "The differing magnitude distributions of the two Jupiter Trojan color populations". *AJ*, 148, 112.

Chapter 5

THE COLOR-MAGNITUDE DISTRIBUTION OF HILDA ASTEROIDS: COMPARISON WITH JUPITER TROJANS

Wong, I. & Brown, M. E. (2017). "The color-magnitude distribution of Hilda asteroids: Comparison with Jupiter Trojans". *AJ*, 153, 69.

ABSTRACT

Current models of solar system evolution posit that the asteroid populations in resonance with Jupiter are comprised of objects scattered inward from the outer Solar System during a period of dynamical instability. In this paper, we present a new analysis of the absolute magnitude and optical color distribution of Hilda asteroids, which lie in the 3:2 mean motion resonance with Jupiter, with the goal of comparing the bulk properties with previously published results from an analogous study of Jupiter Trojans. We report an updated power law fit of the Hilda magnitude distribution through $H = 14$. Using photometric data listed in the Sloan Moving Object Catalog, we confirm the previously-reported strong bimodality in visible spectral slope distribution, indicative of two sub-populations with differing surface compositions. When considering collisional families separately, we find that collisional fragments follow a unimodal color distribution with spectral slope values consistent with the bluer of the two sub-populations. The color distributions of Hildas and Trojans are comparable and consistent with a scenario in which the color bimodality in both populations developed prior to emplacement into their present-day locations. We propose that the shallower magnitude distribution of the Hildas is a result of an initially much larger Hilda population, which was subsequently depleted as smaller bodies were preferentially ejected from the narrow 3:2 resonance via collisions. Altogether, these observations provide a strong case supporting a common origin for Hildas and Trojans as predicted by current dynamical instability theories of solar system evolution.

5.1 Introduction

Over the past few decades, the classical picture of solar system formation and evolution, in which planets formed and smoothly migrated to their present-day locations within the protoplanetary disk, has been beset by significant challenges. The unexpectedly high eccentricities and inclinations of the giant planets, the dynamically excited orbital distribution of the Kuiper Belt, and the irregular satellites of Jupiter and Saturn are among an increasing body of observations that point toward a chaotic restructuring of the solar system orbital architecture after the dispersal of the protoplanetary disk.

Current theories of solar system evolution describe a scenario in which Jupiter and Saturn crossed a mean-motion resonance, setting off a period of dynamical instability throughout the middle and outer Solar System (e.g., Morbidelli et al. 2005). Simulations have shown that the primordial minor body populations in resonance with Jupiter (Hildas and Jupiter Trojans) were first emptied during this turbulent episode and then replaced almost exclusively with planetesimals scattered inward from the region beyond the ice giants (Gomes et al. 2006; Roig & Nesvorný 2015). The major implication of these models is that Kuiper Belt objects, Trojans, and Hildas all originated within a single progenitor population in the outer Solar System and should therefore be largely identical. By comparing the observable properties of Hildas and Trojans, one can evaluate their similarities and/or differences and thereby empirically test current dynamical instability models.

Recent progress in our understanding of Hildas and Trojans has already uncovered many notable similarities. Objects in both populations share the general characteristics of flat, featureless optical and near-infrared spectra with reddish colors (e.g., Dahlgren & Lagerkvist 1995; Dotto et al. 2006; Fornasier et al. 2007; Marsset et al. 2014) and similar, very low albedos (e.g., Fernández et al. 2003; Fernández et al. 2009; Ryan & Woodward 2011). In addition, both Hildas and Trojans are notable in having a bimodal color distribution. Analyses of spectral slopes derived from photometry contained in the Sloan Digital Sky Survey Moving Object Catalog (SDSS-MOC) for both Hildas (Gil-Hutton & Brunini 2008) and Trojans (e.g., Roig et al. 2008; Wong et al. 2014) demonstrate a clear bifurcation in the optical color distribution and indicate the presence of two classes of objects within the Hildas and Trojans. The bimodality in optical color is supported by bimodality in the infrared reflectivity distribution measured by WISE and NEOWISE for both Hildas (Grav et al. 2012b) and Trojans (Grav et al. 2012a).

The most direct way of comparing two populations is by studying their bulk properties, namely, the absolute magnitude distribution and the color distribution. For a population with a narrow range of albedos, such as the Hildas and Trojans, the magnitude distribution is a good proxy for the size distribution and contains information about both the formation environment and the subsequent collisional evolution of the population. The color distribution reveals the diversity of surface types and also provides constraints on models of the composition and origin of objects within the population.

In Wong et al. (2014), we carried out an in-depth study of the color-magnitude distribution of Trojans. In this paper, we present an analogous study for Hildas, in order to obtain a point of reference for comparing the two populations. We report fits to the total Hilda magnitude distribution and provide a detailed analysis of the updated color distribution, as derived from the newest fourth release of the Sloan Moving Object Catalog (SDSS-MOC4). Special attention is given to exploring the properties of individual collisional families. The results of our Hilda analysis are compared with our previously published Trojan results and discussed in relation to collisional evolution, surface composition, and dynamical considerations within the framework of recent dynamical instability models of solar system evolution

5.2 Data and analysis

In this section, we present our analysis of the absolute magnitude and optical color distributions of the Hilda asteroids. The methods used are mostly identical to those described in detail in our previously published analysis of Jupiter Trojans (see Wong et al. 2014 and references therein).

In selecting for Hilda asteroids, we have applied the following constraints in orbital parameter space, which are used by the IAU Minor Planet Center (MPC) in their definition of Hildas: $3.7 \leq a \leq 4.1$ AU, $e \leq 0.3$, and $i \leq 20^{\circ}$. Querying the MPC database with these criteria results in a total count of 3801 Hildas (as of October 2016). Using a less stringent criterion (e.g., extending the maximum values of (a, e, i) to $(4.2 \text{ AU}, 0.4, 30^{\circ})$, as in Grav et al. 2012b) does not appreciably increase the overall number of Hildas and does not significantly affect the results of our analysis.

Studying the color-magnitude distribution of Hilda collisional families is of particular relevance in our understanding of the composition and evolution of the population as a whole. There exist two major collisional families within the Hildas: the Hilda

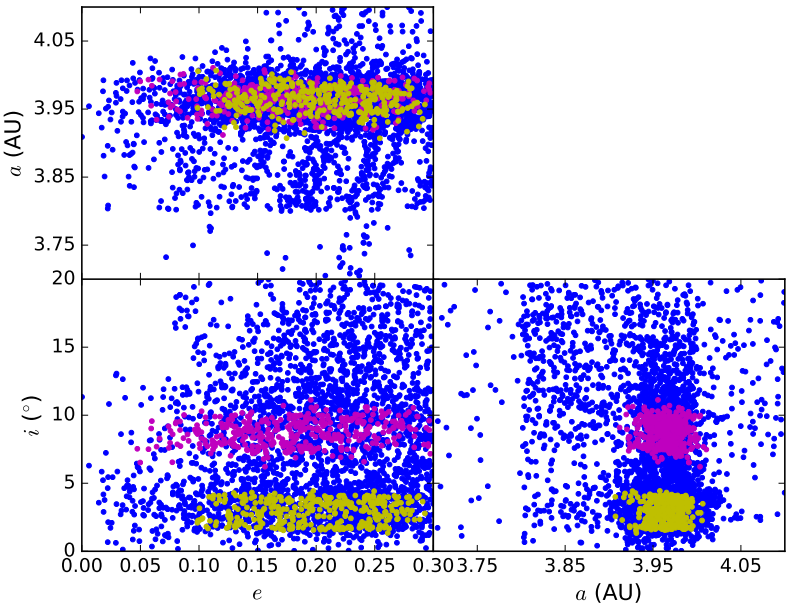

Figure 5.1: Distribution of the 3801 objects in our Hilda dataset, plotted in the space of semi-major axis (a), eccentricity (e), and inclination (i). Objects belonging to the Hilda and Schubart collisional families are denoted by magenta and yellow dots, respectively; background Hildas are denoted by blue dots.

and Schubart families. We have created lists of family members using the tabulated results in Nesvorný & Morbidelli (2012), which identify 385 members of the Hilda family and 350 members of the Schubart family. The distribution of Hildas in (a, e, i) space is illustrated in Figure 5.1, with the location of the two collisional families highlighted.

Magnitude distributions

For each object, we set the absolute magnitude to the value listed in the Asteroid Orbital Elements Databse. The cumulative absolute magnitude distribution of the total Hilda population is shown in Figure 5.2. The magnitude distribution has the characteristic shape seen in many minor body populations, with a steeper slope at large sizes transitioning to a shallower slope at intermediate sizes.

The gentle rollover at $H \sim 16$ reflects the onset of incompleteness in the Hilda dataset. In our analysis of Trojans, we determined the completeness limit of the MPC Trojan dataset to be $H \sim 11.3$ and were able to correct the shape of the magnitude distribution for incompleteness at fainter magnitudes by utilizing the deeper SDSS-

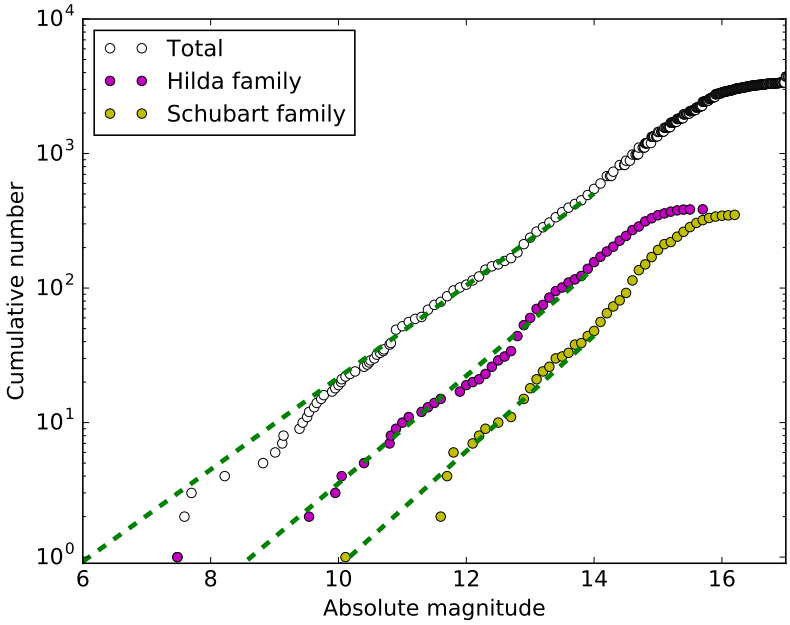

Figure 5.2: Cumulative absolute magnitude distributions of the total Hilda population (white), as well as the Hilda and Schubart collisional families individually (magenta and yellow, respectively). The best-fit power law curves describing the distributions are overplotted (dashed green lines).

MOC4 dataset, which we calculated to be complete for Trojans through $H = 12.3$. In the case of Hildas, however, the onset of incompleteness in the SDSS-MOC4 dataset occurs at a brighter magnitude ($H \sim 14$) than the MPC dataset, and as such, we are unable to correct for incompleteness in the total magnitude distribution. In this paper, we have chosen a conservative upper limit for our analysis at $H = 14$. Varying this limit by 0.5 mag in either direction does not significantly affect the distribution fits.

We fit the total differential magnitude distribution, $\Sigma(H)$, to a single power law of the form

$$\Sigma(\alpha_1, H_0|H) = 10^{\alpha(H-H_0)}, \tag{5.1}$$

where α is the slope of the distribution, and H_0 is the threshold magnitude used to properly normalize the distribution to fit the data.

The best-fit parameter values and 1σ uncertainties were computed using a Markov Chain Monte Carlo (MCMC) ensemble sampler. For the total magnitude distribution, the best-fit parameter values are $\alpha = 0.34^{+0.02}_{-0.01}$ and $H_0 = 6.42 \pm 0.29$. We

also experimented with fitting the total magnitude distribution with a four-parameter broken power law (e.g., Wong et al. 2014; Wong & Brown 2015); however, the addition of a second power law slope is strongly disfavored by the Bayesian Information Criterion (ΔBIC = 8.4; BIC$\equiv -2\log(L) + k\log(n)$, where L is the likelihood of the best-fit solution, k is the number of free parameters, and n is the number of data points).

We also fit the magnitude distributions of the Hilda and Schubart collisional families, which are plotted in Figure 5.2. The best-fit parameters are $\alpha = 0.40^{+0.04}_{-0.03}$ and $H_0 = 8.77^{+0.36}_{-0.37}$ for the Hilda family, and $\alpha = 0.43^{+0.07}_{-0.03}$ and $H_0 = 10.23^{+0.39}_{-0.50}$ for the Schubart family. The slopes of the Hilda and Schubart collisional family magnitude distributions are steeper than the overall population (at the 1.7σ and 2.5σ levels, respectively), and are consistent with the range of power law slopes derived from numerical simulations of asteroid fragmentation (e.g., α =0.44–0.54 in Jutzi et al. 2010).

For each power law fit, we sampled the best-fit distribution to create a model magnitude distribution of the same size as the respective population within the magnitude range under consideration ($H < 14$). We carried out a two-sample Anderson-Darling test, which evaluates the null hypothesis that the model distribution and the data are drawn from the same underlying distribution. In all cases, we could not reject the null hypothesis at a confidence level greater than 50%, demonstrating that the model distribution fits are a statistically good match to the data.

Color distribution and sub-populations

The SDSS-MOC4 lists photometric measurements of minor bodies in the *u, g, r, i, z* bands. We queried the database for Hildas and identified 275 objects that were observed by the Sloan survey. Following the methods of Roig et al. (2008) and Wong et al. (2014), we corrected the listed apparent magnitudes for solar colors and derived relative reflectance fluxes (normalized to 1 in *r* band), discarding observations in which any of the band fluxes had a relative error greater than 10%. For each observation, the spectral slope S was computed from an error-weighted linear least-squares fit to the fluxes in the *g, r, i, z* bands. The *u* band flux was not used in fitting since the flux at those wavelengths typically deviates significantly from the linear trend in the spectrum at longer wavelengths (Roig et al. 2008). For objects with multiple observations, we calculated the weighted average spectral slope.

The spectral slope distribution of Hildas is shown in Figure 5.3, where a clear

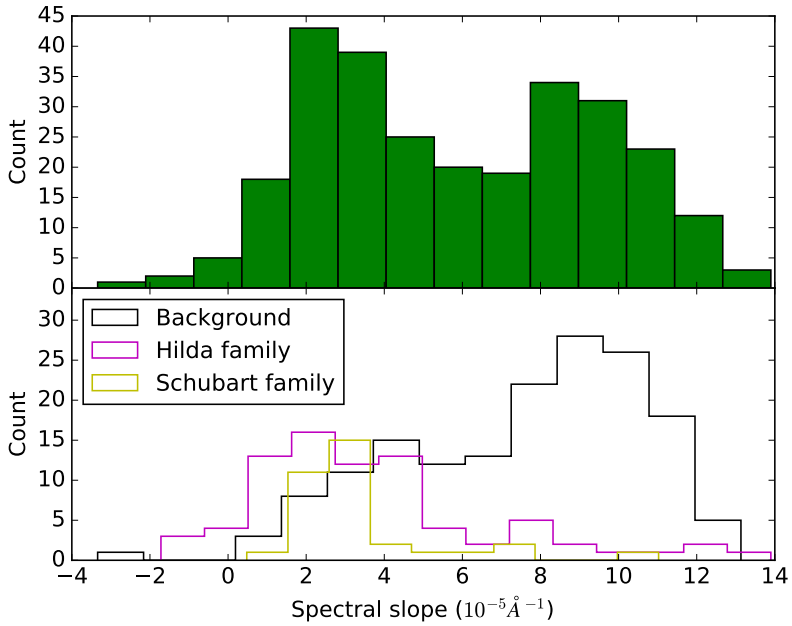

Figure 5.3: Top panel: the overall spectral slope distribution of Hildas, as derived from SDSS-MOC4 photometry, demonstrating a robust color bimodality that divides the population into less-red and red objects. Bottom panel: the spectral slope distributions for Hilda and Schubart family members, as well as background non-family members. Note that the background color distribution is bimodal, while the individual collisional family color distributions are both unimodal.

bimodality is evident, as was first reported in Gil-Hutton & Brunini (2008). The earlier study used the previous, third release of the Moving Object Catalog (SDSS-MOC3) and identified 122 Hildas in the dataset. The latest release more than doubled the number of Hildas with photometric measurements. To quantitatively assess the significance of the bimodality, we fit single and double Gaussian models to the color distribution and found that the two-peaked model is very strongly favored (ΔBIC = 45.1). Notably, we found that the bimodality in the color distribution is discernible throughout the entire magnitude range covered by the Sloan observations, which counters the observation in Gil-Hutton & Brunini (2008) of an apparent lack of low spectral slope objects in the range $10 < H < 12$.

The bimodality in the color distribution indicates that the Hilda population is composed of two types of objects, with characteristically different surface colors. Following the terminology in Wong et al. (2014), we refer to these as the less-red (LR) and red (R) Hildas. We did not detect any significant correlations between

spectral slope and any orbital parameter, which demonstrates that LR and R Hildas are well-mixed within the overall population.

We also studied the color distribution of Hilda and Schubart family members. The bottom panel of Figure 5.3 shows the color distribution of the two families along with the color distribution of non-family Hildas (i.e., background objects). The key observation here is that the color distribution of family members is unimodal and centered at relatively low spectral slope values consistent with the LR sub-population, whereas the background population (and the Hilda population overall) is bimodal in color. Examining the distribution of background objects with low spectral slope values in orbital parameter space, we do not find any notable correlation with the location of known family members; therefore, we do not expect significant contamination of collisional family members within the background population. Conversely, the handful of high spectral slope family members are likely interlopers and not formally collisional fragments.

These results may indicate that the progenitor bodies of the Hilda and Schubart families were LR objects. Alternatively, the unimodal color distribution of collisional fragments may demonstrate the pristine interior material of Hilda asteroids, upon irradiation and space weathering, evolve to take on a less-red color, regardless of the color of the progenitor body. The latter possibility has important implications for the our understanding of the origin of the color bimodality, as we discuss in the next section.

In order to classify individual objects as LR or R Hildas, we fit the spectral slope distribution of background Hildas with a double Gaussian and obtained the mean colors of the LR and R sub-populations — 4.0×10^{-5} Å^{-1} and 9.3×10^{-5} Å^{-1}, respectively. We chose to remove family members in our calculation of mean colors since the surface composition of fragments may be systematically different than the surfaces of uncollided Hildas and would therefore not accurately reflect the initial color distribution. Using an analogous methodology to the one described in Wong et al. (2014), we categorized all Hildas (including collisional fragments) with $S \leq 4.0 \times 10^{-5}$ Å^{-1} as LR and all Hildas with $S \geq 9.3 \times 10^{-5}$ Å^{-1} as R, resulting in a sample of 107 LR and 63 R Hildas. The cumulative absolute magnitude distributions of the LR and R sub-populations are shown in Figure 5.4.

Both distributions are characterized by wavy shapes that are not well-described by a single or double power law; we do not present distribution fits for the individual color sub-population magnitude distributions in this paper. Nevertheless, we compared

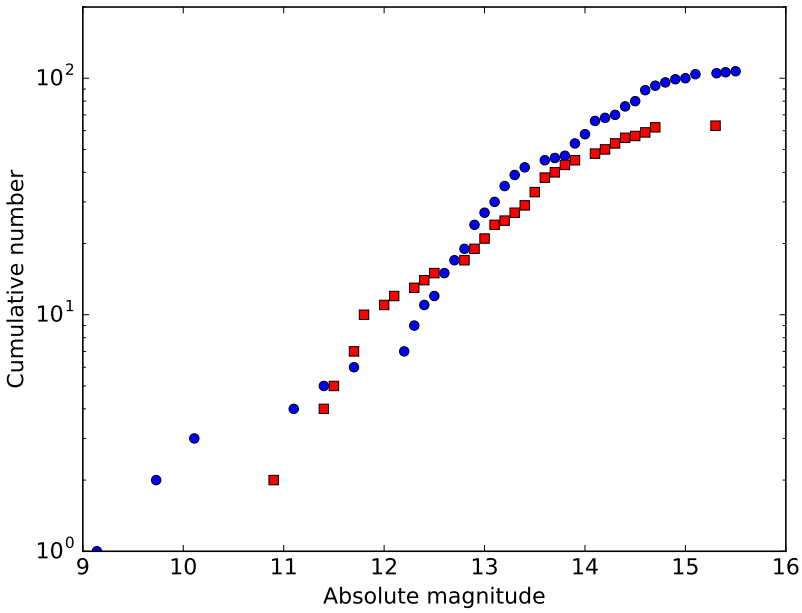

Figure 5.4: The cumulative magnitude distributions of the LR and R sub-populations, where objects (including family members) have been categorized into the sub-populations by spectral slope. The distributions are statistically distinct from each other at the 98% confidence level. Both distributions have a characteristically wavy shape that is not consistent with a single or double power law curve.

the LR and R magnitude distributions using the two-sample Anderson-Darling test. We reject the null hypothesis that the LR and R magnitude distributions are sampled from a single underlying distribution at the 0.8% significance level. In other words, the two color magnitude distributions are statistically distinct at the 99.2% confidence level.

5.3 Discussion

Having carried out an analysis of the color-magnitude distribution of Hildas analogous to the one presented for Trojans in Wong et al. (2014), we are now in a position to compare the two populations. Recent dynamical instability models of solar system evolution describe a common progenitor population of minor bodies in the primordial trans-Neptunian region from which both Hildas and Trojans are sourced. It follows that, if the current paradigm of solar system evolution is correct, there should be notable similarities between the observable properties of the two populations.

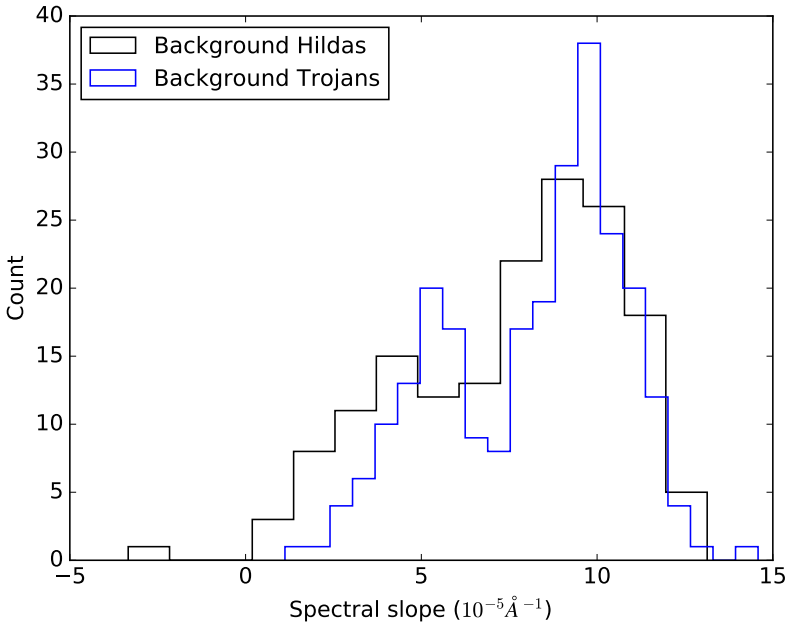

Figure 5.5: Comparison of the Hilda and Trojan color distributions, with family members removed. For Hildas, all objects brighter than $H = 14$ are shown, while for Trojans, all objects brighter than $H = 12.3$ are shown; these are the established completeness limits of the corresponding analyses (see Wong et al. 2014 for the discussion of Trojans). Both distributions show a clear bifurcation in color, corresponding to the LR and R sub-populations present in both populations, with comparable mean colors. The R-to-LR number ratio in both Hilda and Trojan background populations are also similar.

The most salient similarity between Hildas and Trojans is their bimodal color distributions. Figure 5.5 shows the spectral slope distributions for Hildas and Trojans. Since fragments from a major collision introduce a significant number bias in the color distribution of a population relative to the initial pre-collision state, we have removed the Hilda and Schubart family members in order to compare the background populations only. Running the normal mixture model test on the background Hilda and Trojan color distributions (Section 5.2), we find that a two-peaked model is very strongly favored over a single-peaked model in both cases (ΔBIC values of 16.7 and 39.1, respectively). From the figure, we can see that the characteristic mean colors of the LR and R Hildas and Trojans are comparable. The mean colors of the Trojan LR and R sub-populations are 5.3×10^{-5} Å^{-1} and 9.6×10^{-5} Å^{-1}, respectively, as compared to the somewhat bluer mean colors of the Hilda LR and R sub-populations (4.0×10^{-5} Å^{-1} and 9.3×10^{-5} Å^{-1}, respectively).

In addition, the number ratio of R-to-LR objects is similar for the Hildas and Trojans. In Wong et al. (2014), we categorized 47 background Trojans as LR and 104 as R, while in the present work, we obtained a categorized sample of 28 LR and 56 R objects out of the background Hilda population. For both non-family Hildas and Trojans, the R-to-LR number ratio is roughly 2-to-1.

The origin of the color bimodality in the Trojans and Hildas has long remained unexplained. Earlier explanations concerning the color bimodality in Trojans suggested that the LR and R populations may have been sourced from different regions of the solar nebula, with one population originating in the middle Solar System and the other scattered in from the outer Solar System. However, within the framework of current dynamical instability models, such a scenario is not supported; instead, both LR and R Hildas and Trojans are predicted to have been emplaced from the same primordial collection of planetesimals in the outer Solar System.

In a hypothesis first proposed in Wong et al. (2014) and subsequently developed in full in Wong & Brown (2016), we posited that the color bimodality arose within the primordial trans-Neptunian planetesimal disk, i.e., the purported progenitor population of Trojans and Hildas. In short, objects in this region accumulated out of a mix of rocky material and ices of roughly cometary composition, including a significant volume of volatile ices such as ammonia and methanol. Under the action of solar irradiation, location-dependent volatile loss led to differential surface depletion of the various volatile ices: objects closer in experienced higher surface temperatures and faster rates of sublimation, leading to the depletion of the more volatile species from the surface layers, while objects farther out were colder and thereby retained some of the more volatile species.

In the volatile loss model we developed, it was shown that H_2S would have been a key distinguishing factor, dividing the trans-Neptunian planetesimal population into two groups, with the closer objects depleted in H_2S on their surfaces and farther objects retaining H_2S. Irradiation of the volatile ice rich surfaces would have reddened and darkened the surfaces of all objects in the region, as has been demonstrated in various laboratory experiments (e.g., Brunetto et al. 2006); however, irradiation of objects that retained H_2S on their surfaces would have produced sulfur-bearing molecules in the irradiated mantle, which is expected to provide a significant additional reddening (e.g., as in the polar deposits on Io; Carlson et al. 2007). As a result, we posited that the H_2S-retaining objects would have attained characteristically redder surface colors than the H_2S-depleted objects. The subsequent scattering of the trans-Neptunian

planetesimal disk and the emplacement of Hildas and Trojans into their present-day locations would have preserved this primordial color bifurcation.

This hypothesis for the observed color bimodality has an important implication that explains another point of similarity between Hildas and Trojans — the observation that all collisional family members are LR. As shown in Section 5.2, both the Hilda and Schubart families are composed of exclusively LR objects; analyzed spectra of objects from the only robustly attested major collisional family in the Trojans — the Eurybates family (Brož & Rozehnal 2011) — reveal a similar pattern in which the family members have a unimodal color distribution centered at relatively low spectral slopes (Fornasier et al. 2007). Regardless of the original surface color of the parent bodies, our color bimodality hypothesis offers a natural explanation for the observed trend. Upon a shattering impact, the fragments are composed of the pristine interior material of the parent bodies, namely, rocky material, water ice, and any remaining volatile ices trapped in the subsurface. At the much higher temperatures of the Hilda and Trojan regions, the volatile ices sublimate instantaneously from the surfaces of the family members. Consequently, irradiation of these volatile-depleted surfaces would not lead to reddening of the same extent as in the case where volatile ices are retained (in particular, H_2S), resulting in LR surface colors.

Moving on to the magnitude distributions, we compare the total cumulative magnitude distributions for Hildas and Trojans in Figure 5.6. The general shape of the distributions is the same. In Wong et al. (2014), we modeled the collisional evolution of Trojans using the intrinsic collisional probabilities and impact velocities derived from previously published numerical simulations. We found that current level of collisional activity is insufficient to have produced the observed break in the magnitude distribution at $H \sim 9$ starting from a single power law initial magnitude distribution (see also Marzari et al. 1997); instead, the break is likely to be a consequence of the much more intense collisional environment in the early trans-Neptunian planetesimal region from which the Trojans and Hildas originated. From our modeling, we showed that the collisional evolution of the Trojans, assuming current rates, would only have resulted in a slight flattening of the power law slope at intermediate sizes.

A major difference between the Hilda and Trojan magnitude distributions is that the former is significantly shallower at all sizes. In particular, the power law slopes at intermediate sizes — 0.46 ± 0.01 (Wong et al. 2014) and $0.34^{+0.02}_{-0.01}$ (Section 5.2) for the Trojans and Hildas, respectively — are discrepant at the 5.4σ level. In the

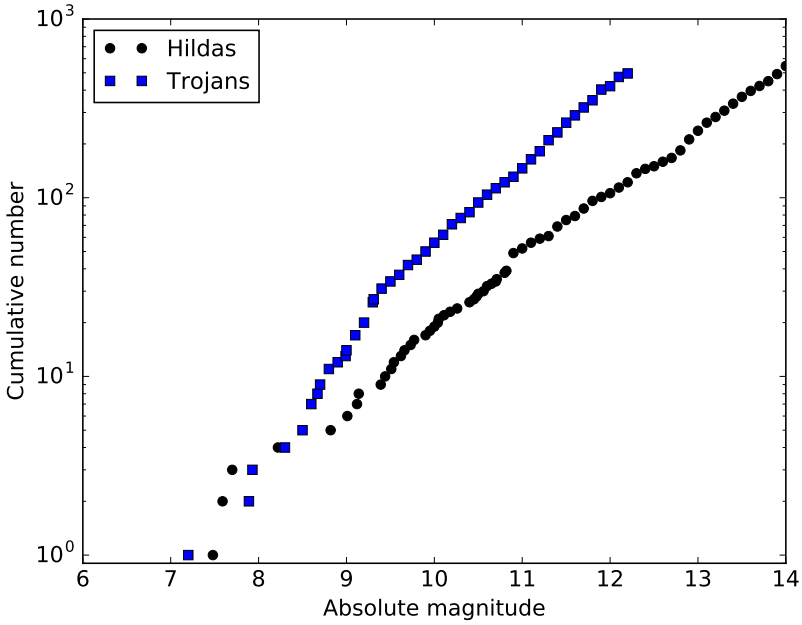

Figure 5.6: Comparison of the total cumulative magnitude distributions of Hildas (black dots) and Trojans (blue squares). The Trojan distribution has been corrected for incompleteness, following the methods of Wong et al. (2014). The Hilda magnitude distribution is notably shallower throughout the entire magnitude range of the data.

context of collisional evolution and assuming that both Hildas and Trojans were derived from the same progenitor population and therefore were emplaced with similar initial size distributions, the shallower Hilda magnitude distribution would be indicative of a more active collisional environment. However, estimates of both the current intrinsic collisional probability and impact velocities are significantly lower for the Hildas than for the Trojans (Davis et al. 2002 and references therein). This inconsistency presents a challenge to the idea of a common origin for the Hildas and Trojans as proposed by current dynamical instability models.

One possible explanation is apparent when considering the number of major collisional families in the Hildas and Trojans. Despite its lower current rate of collisional activity, the Hilda population contains two major collisional families, with the Hilda family containing the largest object (153 Hilda, $H = 7.48$) in the entire population. Meanwhile, the Trojan population has only one major family, the Eurybates family, with its largest object (3548 Eurybates, $H = 9.7$) being significantly smaller than 153 Hilda. All else being equal, the frequency of shattering collisions decreases

sharply with increasing target size, due to the decrease in the number of impactors capable of fragmenting the target body. Assuming that the characteristic impact velocity of a resonant population does not change appreciably with time, one way of increasing the collisional probability for large targets is by increasing the number of impactors.

Therefore, the presence of two major collisional families in the Hildas suggests that perhaps the number of objects emplaced into the 3:2 resonance initially was much higher, creating a significantly more active early collisional environment, but was gradually depleted as collisional activity pushed fragments out of the resonance and out of the Hilda population. The 3:2 mean motion resonance with Jupiter has a narrow 0.1 AU-wide stable zone centered at 3.96 AU, surrounded on both sides by a dynamically chaotic boundary region with very short characteristic diffusion times (Ferraz-Mello et al. 1998). In Figure 5.1, the location of the stable zone is evident in the sharp decrease in object density outside of the central region.

Following a scenario that has been described by several earlier works (e.g., Gil-Hutton & Brunini 2008), if a collisional fragment is ejected from the central stable region, it is removed from the resonance on a relatively short timescale, thereby depleting the magnitude distribution. The relative ejection velocity required for a fragment to pass out of the center of the resonance is around $\Delta V \sim 0.16$ km/s (Davis et al. 2002). Based on the results of numerical models simulating the fragmentation of asteroidal bodies and given the characteristic impact velocity in the Hilda population (Davis et al. 2002), a significant fraction of collisional fragments is expected to have a sufficient ejection velocity to exit the resonance (Jutzi et al. 2010). These same simulations demonstrate that the smallest fragments tend to be imparted the highest ejection velocity.

Since the smaller bodies experience more frequent collisions and are also more likely to be ejected from the stable zone, the initial Hilda magnitude distribution would have become depleted most severely at faint magnitudes, consistent with the relatively shallow Hilda distribution when compared with the Trojan distribution. Eventually, as the total number of Hildas fell due to the removal of objects from resonance, the intrinsic collisional probability decreased to the present-day value.

Relating back to the important implication of our color bimodality hypothesis that collisional fragments are LR, a higher initial level of collisional activity also explains the distinct shapes of the LR and R Hilda magnitude distributions (Figure 5.4). Collisions enrich the LR population exclusively and lead to a relative steepening in

the shape of the LR magnitude distribution with time. The overall R-to-LR number should decrease with decreasing size, since collisions are much more frequent for smaller targets. In the Trojan population, the cumulative LR magnitude distribution was shown in Wong & Brown (2015) to overtake the R magnitude distribution at $H \sim 15$. While the initial R-to-LR ratio of the Hildas was similar to that of the Trojans, as demonstrated by our earlier comparison of the background, uncollided color distribution (Figure 5.5), we see that the LR sub-population becomes more numerous than the R sub-population at a larger size ($H \sim 13$), due to the significant enrichment of the LR sub-population by Hilda and Schubart family members.

All in all, the comparison of the magnitude and color distributions of Hildas and Trojans reveals several notable similarities, with the discrepancies in the present-day magnitude distribution shapes addressed by a dynamically plausible explanation. In turn, the body of observational data analyzed in this work presents a convincing case that the Hildas and Trojans originated from the same progenitor population prior to being emplaced in their current locations, as is predicted by current dynamical instability models of solar system evolution.

5.4 Conclusion

In this paper, we analyzed the absolute magnitude and optical color distributions of the Hilda asteroids. We computed a power law fit to the magnitude distribution through $H = 14$ and found a slope of $\alpha = 0.34^{+0.02}_{-0.01}$. Using photometric measurements contained in SDSS-MOC4, we calculated the spectral slope of 275 Hildas and confirmed the robust bimodality in color reported in Gil-Hutton & Brunini (2008). This bimodality demonstrates that the Hilda population is composed of two groups of objects: less-red and red Hildas. We classified individual objects into the two color sub-populations and presented the individual color magnitude distributions, which were shown to be highly distinct from each other. We also analyzed the Hilda and Schubart collisional families separately and found that the families are composed of LR objects only.

Our comparison of the Hilda and Trojan color distributions revealed that both are bimodal, with similar characteristic LR and R colors. Furthermore, the R-to-LR number ratios among non-family Hildas and Trojans are consistent with each other; likewise, both populations display the same trend in which collisional family members are exclusively LR. Within the framework of dynamical instability models, our analysis of the Hilda and Trojan color distributions supports our previously

published hypothesis that the color bimodality seen in both populations developed prior to emplacement in their current-day locations, with the difference in color primarily arising due to the retention vs. depletion of H_2S ice on the surfaces of planetesimals within the primordial trans-Neptunian disk.

Comparing the Hilda and Trojan total magnitude distributions, we showed that the Hilda distribution is significantly shallower than the Trojan distribution, despite being much less collisionally active at the present time. Upon consideration of the number of major collisional families in each population, we proposed an explanation for the discrepancy in magnitude distributions by positing that the Hilda population upon emplacement was significantly larger than the current population. This hypothesis naturally explains the higher apparent level of collisional evolution in the Hilda magnitude distributions (evidenced by the shallower power law slope at intermediate sizes), since small collisional fragments are readily ejected from the narrow stable zone of the 3:2 resonance and removed from the population.

We conclude that the bulk properties of Hildas and Trojans lend strong support to the idea of a shared progenitor population — a major step in validating one of the main predictions of current dynamical instability models of solar system evolution. In further validation of these models, our photometric survey observations of small dynamically excited Kuiper Belt objects (KBOs) in the same size range as Hilda and Trojan asteroids reveal that these KBOs are likewise bimodal in optical color (Wong & Brown 2017). We also show that the two color classes among the small KBOs have magnitude distributions that are statistically indistinguishable from the magnitude distributions of LR and R Trojans. Taken together, these studies provide the first body of observational evidence linking the properties of KBOs, Hildas, and Trojans.

The question of the composition of Hildas, Trojans, and similarly sized KBOs remains unresolved and could provide a complementary probe into the similarities and/or differences between the respective asteroid populations. Intensive spectroscopic observations of Hildas and Trojans using current and near-future instruments promise to provide improved constraints on the surface composition of these bodies, which will help solidify our understanding of their origin.

References

Brož, M. & Rozehnal, J. (2011). "Eurybates – the only asteroid family among Trojans?" *Mon. Not. R. Astron. Soc.* 414, 565.

Brunetto, R., Barucci, M. A., Dotto, E., & Strazzulla, G. (2006). "Ion irradiation of frozen methanol, methane, and benzene: Linking to the colors of Centaurs and trans-Neptunian objects". *ApJ*, 644, 646.

Carlson, R. W., Kargel, J. S., Douté, S., Soderblom, L. A., & Brad Dalton, J. (2007). "Io's Surface Composition". In: *Io After Galileo*. Eds. Lopes, R. M. C. & Spencer, J. R. (Chichester, UK: Praxis Publishing Ltd), 194.

Dahlgren, M. & Lagerkvist, C.-I. (1995). "A study of Hilda asteroids. I. CCD spectroscopy of Hilda asteroids". *A&A*, 302, 907.

Davis, D. R., Durda, D. D., Marzari, F., Bagatin, A. C., & Gil-Hutton, R. (2002). "Collisional Evolution of Small-Body Populations". In: *Asteroids III*. Eds. Bottke J., W. F., Cellino, A., Paolicchi, P., & Binzel, R. P. (Tucson, AZ: University of Arizona Press), 545.

Dotto, E., Fornasier, S., Barucci, M. A., et al. (2006). "The surface composition of Jupiter Trojans: Visible and near-infrared survey of dynamical families". *Icarus*, 183, 420.

Fernández, Y. R., Jewitt, D., & Ziffer, J. E. (2009). "Albedos of small Jovian Trojans". *AJ*, 138, 240.

Fernández, Y. R., Sheppard, S. S., & Jewitt, D. C. (2003). "The albedo distribution of Jovian Trojan asteroids". *AJ*, 126, 1563.

Ferraz-Mello, S., Nesvorný, D., & Michtchenko, T. A. (1998). "Chaos, Diffusion, Escape and Permanence of Resonant Asteroids in Gaps and Groups". In: *Solar System Formation and Evolution*. Eds. Lazzaro, D., Vieira Martins, R., Ferraz-Mello, S., & Fernandez, J. (San Francisco, CA: ASP), 65.

Fornasier, S., Dotto, E., Hainaut, O., et al. (2007). "Visible spectroscopic and photometric survey of Jupiter Trojans: Final results on dynamical families". *Icarus*, 190, 622.

Gil-Hutton, R. & Brunini, A. (2008). "Surface composition of Hilda asteroids from the analysis of the Sloan Digital Sky Survey colors". *Icarus*, 193, 567.

Gomes, R., Levison, H. F., Tsiganis, K., & Morbidelli, A. (2006). "Origin of the cataclysmic Late Heavy Bombardment period of the terrestrial planets". *A&A*, 455, 725.

Grav, T., Mainzer, A. K., Bauer, J. M., Masiero, J. R., & Nugent, C. R. (2012a). "WISE/NEOWISE observations of the Jovian Trojan population: Taxonomy". *ApJ*, 759, 49.

Grav, T., Mainzer, A. K., Bauer, J., & Masiero, J. (2012b). "WISE/NEOWISE observations of the Hilda population: Preliminary results". *ApJ*, 744, 197.

Jutzi, M., Michel, P., Benz, W., & Richardson, D. C. (2010). "Fragment properties at the catastrophic disruption threshold: The effect of the parent body's internal structure". *Icarus*, 207, 54.

Marsset, M., Vernazza, P., Gourgeot, F., & Dumas, C. (2014). "Similar origin for low- and high-albedo Jovian Trojans and Hilda asteroids". *A&A*, 568, L7.

Marzari, F., Frinella, P., Davis, D. R., Scholl, H., & Campo Bagatin, A. (1997). "Collision evolution of Trojan asteroids". *Icarus*, 125, 39.

Morbidelli, A., Levison, H. F., Tsiganis, K., & Gomes, R. (2005). "Chaotic capture of Jupiter's Trojan asteroids in the early Solar System". *Nature*, 435, 462.

Nesvorný, D. & Morbidelli, A. (2012). "Statistical study of the early Solar System's instability with four, five, and six giant planets". *AJ*, 144, 117.

Roig, F. & Nesvorný, D. (2015). "The evolution of asteroids in the jumping-Jupiter migration model". *AJ*, 150, 186.

Roig, F., Ribeiro, A. O., & Gil-Hutton, R. (2008). "Taxonomy of asteroid families among the Jupiter Trojans: comparison between spectroscopic data and the Sloan Digital Sky Survey colors". *A&A*, 483, 911.

Ryan, E. L. & Woodward, C. E. (2011). "Albedos of small Hilda group asteroids as revealed by Spitzer". *AJ*, 141, 186.

Wong, I. & Brown, M. E. (2015). "The color-magnitude distribution of small Jupiter Trojans". *AJ*, 150, 174.

Wong, I. & Brown, M. E. (2016). "A hypothesis for the color bimodality of Jupiter Trojans". *AJ*, 152, 90.

Wong, I. & Brown, M. E. (2017). "The color-magnitude distribution of Hilda asteroids: Comparison with Jupiter Trojans". *AJ*, 153, 69.

Wong, I., Brown, M. E., & Emery, J. P. (2014). "The differing magnitude distributions of the two Jupiter Trojan color populations". *AJ*, 148, 112.

Chapter 6

THE BIMODAL COLOR DISTRIBUTION OF SMALL KUIPER BELT OBJECTS

Wong, I. & Brown, M. E. (2017). "The bimodal color distribution of small Kuiper Belt objects". *AJ*, 153, 145.

ABSTRACT

We conducted a two-night photometric survey of small Kuiper Belt objects (KBOs) near opposition using the wide-field Hyper Suprime-Cam instrument on the 8.2 m Subaru Telescope. The survey covered about 90 $\deg^2$ of sky, with each field imaged in the g and i bands. We detected 356 KBOs, ranging in absolute magnitude from 6.5 to 10.4. Filtering for high-inclination objects within the hot KBO population, we show that the $g - i$ color distribution is strongly bimodal, indicative of two color classes — the red and very red subpopulations. After categorizing objects into the two subpopulations by color, we present the first dedicated analysis of the magnitude distributions of the individual color subpopulations and demonstrate that the two distributions are roughly identical in shape throughout the entire size range covered by our survey. Comparing the color distribution of small hot KBOs with that of Centaurs, we find that they have similar bimodal shapes, thereby providing strong confirmation of previous explanations for the attested bimodality of Centaurs. We also show that the magnitude distributions of the two KBO color subpopulations and the two color subpopulations observed in the Jupiter Trojans are statistically indistinguishable. Finally, we discuss a hypothesis describing the origin of the KBO color bimodality based on our survey results.

6.1 Introduction

Obtaining a better understanding of the composition of Kuiper Belt objects (KBOs) has become a major field of interest in planetary science, with important implications for formation and evolution theories of the solar system. Over the past decade, a concerted observational effort has produced a significant increase in the number of known objects and revealed the dynamical complexity of the Kuiper Belt region.

However, even with recent advances in telescope capabilities, the great heliocentric distances of these bodies continue to be an obstacle for detailed characterization of their surfaces. At present, only the largest KBOs are amenable to spectroscopic study with sufficient signal-to-noise to distinguish absorption features of chemical species.

While spectroscopic observations of large KBOs have revealed a wide range of absorbing species (such as ammonia, methanol, methane, and ethane; see, for example, review by Brown 2012), the surface compositions of these bodies are not expected to reflect directly on the primordial makeup of the protoplanetary disk in the trans-Neptunian region. These large objects, with diameters exceeding ~500 km, have sufficient mass to be gravitationally circularized and are likely internally differentiated. As a result, their surfaces have been shaped by secondary processes (including the possible retention of tenuous and/or ephemeral atmospheres) and may differ significantly from their bulk composition. To obtain a more representative picture of the bulk composition of KBOs, we must study smaller objects, whose surfaces are more representative of the primordial planetesimals in the trans-Neptunian region.

Broadband photometry has served as a powerful tool for understanding the surface properties of smaller KBOs. An analysis of the range of colors within the overall KBO population and trends in the color distribution with relation to the various dynamical classes within the Kuiper Belt region provides a descriptive picture of the compositional diversity of the formation environment and how the Kuiper Belt evolved to its current state. To date, hundreds of KBO colors have been measured, revealing the general properties of low albedos and reddish colors across the intermediate and small size ranges, extending down through objects with diameters of 50 km and less (Hainaut et al. 2012). Several studies have suggested a color bimodality among objects in the dynamically-excited (i.e., hot) KBO population (e.g., Fraser & Brown 2012; Peixinho et al. 2012; Lacerda et al. 2014). A bimodal color distribution would have major implications for the formation of these bodies, indicating two types of surface compositions and perhaps two different formation environments. However, since most of the color measurements in the literature have been obtained through targeted observations, the observational biases are difficult to quantify, and as such, the underlying color distribution of hot KBOs remains poorly constrained.

Photometric observations of Centaurs, which are former members of the hot KBO population that have been scattered onto giant planet crossing orbits, provide a

complementary look at the color distribution of these outer solar system objects. Their smaller heliocentric distances allow greater ease in obtaining precise color measurements. Recent analyses of Centaurs demonstrate a robust bimodality in the optical color distribution extending through the entire observed size range — from the largest Centaur, 10199 Chariklo (∼250 km), down through ∼10 – 20 km sized objects — dividing the Centaur population into two color classes (e.g., Peixinho et al. 2003; Barucci et al. 2005; Perna et al. 2010).

Some have argued that, based on the putative color bimodality of similarly-sized hot KBOs, the two color classes in the Centaurs correspond to the two color classes observed in the Kuiper Belt (Fraser & Brown 2012; Peixinho et al. 2012; Peixinho et al. 2015). Others have posited that the bimodality in the Centaur color distribution could have arisen from divergent orbital histories of these objects as they were scattered inward into their present-day eccentric orbits: objects that spent a larger fraction of the time at small heliocentric distances would have experienced on average higher temperatures and space weathering, which may have altered their surfaces (Melita et al. 2008). Without a fuller understanding of the underlying color distribution of KBOs in this size range, the origin of the Centaur color bimodality has remained an open question.

We present the results of the first systematic photometric survey of small KBOs, conducted using the Hyper Suprime-Cam instrument at the Subaru Telescope.This instrument has the largest field of view of any camera on an 8–10 m class telescope currently in operation, making it the ideal tool for surveying small Kuiper Belt objects. By imaging fields in two bandpasses, we were able to simultaneously detect KBOs (on average 7 per field) and measure their colors to efficiently achieve a uniform survey dataset. Filtering our dataset to study the hot KBO population specifically, we report a robust bimodality in the color distribution. The paper is organized as follows: The observing strategy and data processing methods of our survey are described in Section 6.2. In Section 6.3, we analyze the color distribution of hot KBOs and categorize objects into the two color classes in order to study their magnitude distributions individually. Finally, in Section 6.4, we discuss the survey results in the context of previous analyses of Centaurs and Jupiter Trojans and present a hypothesis of the origin of the color bimodality.

6.2 Observations

We carried out observations of the Kuiper Belt near opposition using the Hyper Suprime-Cam instrument (HSC) on the 8.2 m Subaru Telescope at Mauna Kea, Hawaii during the nights of UT 2014 September 23 and 2015 March 19. The HSC is a wide-field prime focus camera that consists of a mosaic of 104 2048×4096 pixel CCD detectors and covers a 90′ diameter field of view with a pixel scale of 0.17″ (Miyazaki et al. 2002). We obtained four 180 s exposures in each of our observing fields — twice in the g filter ($\lambda_{\rm eff}$ = 480.9 nm) and twice in the i filter ($\lambda_{\rm eff}$ = 770.9 nm). Fields were imaged in groups following the band sequence $i - i - g - g$ or $g - g - i - i$ in order to minimize the number of filter changes. The average observational arc for each field is 230 minutes, with the four exposures in each field spaced roughly evenly at 1 hour intervals. The time interval between exposures did not vary significantly from field to field or between the two nights of observation. Figure 6.1 shows the on-sky positions of the 52 observed fields, with a total surveyed area of 92 deg^2. Full details of our observations and computed orbital, magnitude, and color information are provided in a supplemental table.

We processed the images and detected moving objects using methods similar to those described in detail in our previous Subaru/Suprime-Cam survey of small Jupiter Trojans (Wong & Brown 2015). After bias-subtracting and flat-fielding the images, we calculated the astrometric solution for each chip by first creating a pixel position catalog of all the bright sources using Version 2.11 of SExtractor (Bertin & Arnouts 1996) and then feeding the catalog into Version 1.7.0 of SCAMP (Bertin 2006) to compute the astrometric projection parameters. The typical residual RMS value between the on-sky positions of detected stars in an image and matched reference stars is much less than 0.5″; the typical RMS of the position offset between matched stars across images taken in the same observing field is less than 0.05″.

After passing the distortion-corrected images through SExtractor again, with the detection threshold set at 1.5 times the background standard deviation, we systematically searched for transients, i.e., sets of four source detections (one in each of the four images in an observing field) that do not reoccur in the same location. We carried out orbital fits for all transients using the methods described in Bernstein et al. (2004). A transient was classified as a moving object candidate if the corresponding χ^2 value from the orbit fit was less than 15. We considered only transients consistent with apparent sky motion less than 10″/hr; this cutoff was chosen with the intent of detecting some closer-in Centaurs, in addition to KBOs.

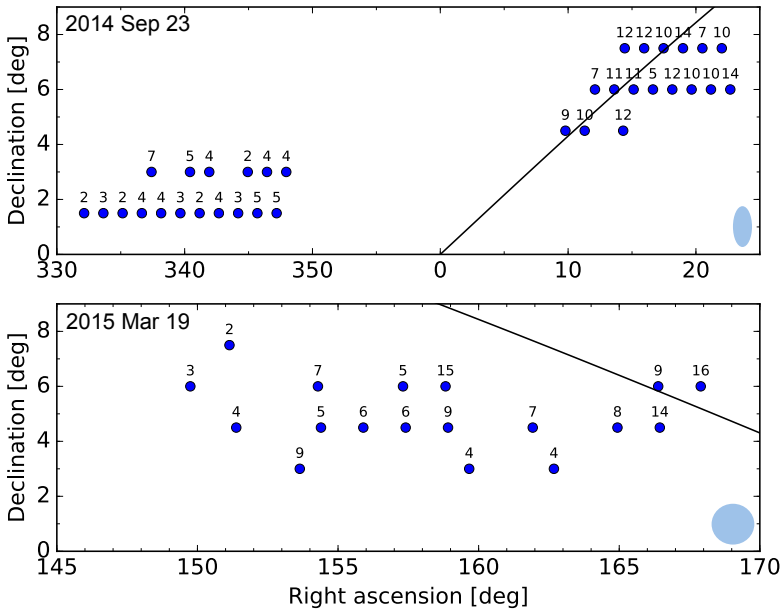

Figure 6.1: Locations of the 52 Subaru Hyper Suprime-Cam fields observed as part of our two-night Kuiper Belt color survey (blue points). The position of the ecliptic on each night is indicated by the solid black line. The number of objects detected in each field is given by the number above the corresponding point. The shaded ellipse shown in the lower right corner of each panel represents the field of view of each exposure, to scale.

We visually verified every moving object candidate, rejecting all non-asteroidal moving object candidates, as well as asteroids that passed through regions of the chip that would likely yield unreliable and uncorrectable magnitude measurements (e.g., diffraction spikes, chip artifacts). Our survey detected a total of 372 validated objects. Of these objects, 18 passed in front of background stars, coincided with a cosmic ray hit, or passed close to the edge of a chip in one out of the four exposures. For these objects, we removed the problematic detections from consideration in computing heliocentric distances and measuring magnitudes. The distribution of heliocentric distances (computed in our orbital fits) for all 372 objects is shown in Figure 6.2. The median uncertainty in the calculated heliocentric distances is 3.5 AU.

We considered all 356 objects with heliocentric distances larger than the orbital semi-major axis of Neptune (roughly 30 AU) to be KBOs, with the remaining 16 closer-in objects identified as Centaurs. The separation between KBOs and Centaurs

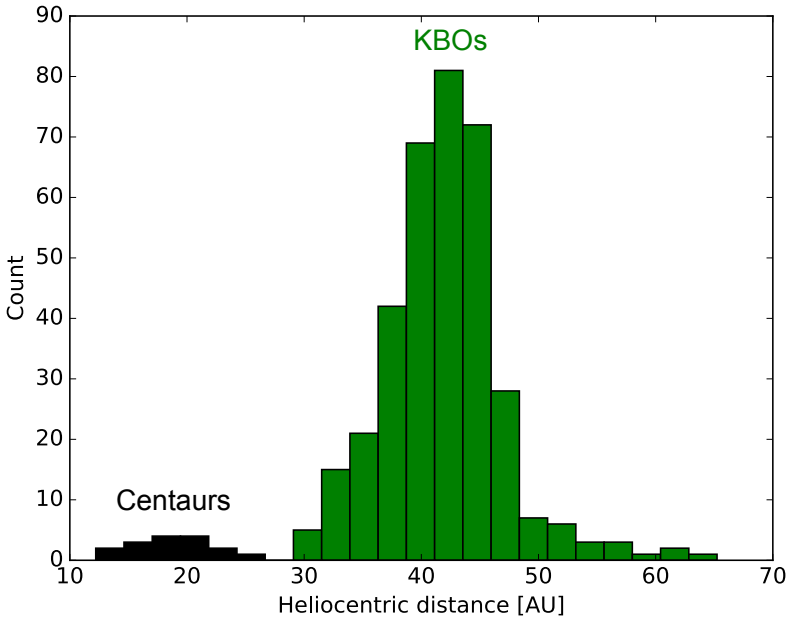

Figure 6.2: Distribution of heliocentric distance for the 372 asteroids detected in our survey. Objects with heliocentric distances greater than 30 AU are classified as KBOs, while the closer-in objects are Centaurs. The typical uncertainty of our heliocentric distance estimates is 3.5 AU.

is evident in the plot of heliocentric distances. In our analysis, we also sought to filter out possible contamination from cold classical KBOs, which are characterized by photometric properties, orbital properties, and a size distribution that are distinct from the rest of the Kuiper Belt (see, for example, the review by Brown 2012 and references therein).

Since cold classical KBOs have low orbital inclinations, we wanted to remove from consideration all objects with inclinations less than 5° (as was done in, for example, Bernstein et al. 2004). Due to our survey's short observational arcs, the uncertainties in calculated inclinations are quite large, averaging around 10°. To select for hot KBOs, we filter for objects observed at ecliptic latitudes greater than 5° and/or objects with measured inclinations greater than 5° at the 1σ level (i.e., $i - \Delta i > 5°$). The resulting final set of hot KBOs contains 136 objects and serves as the operational KBO dataset for our analysis. In the following, we will refer to this dataset as simply the survey KBOs.

We measured the flux of each object through a fixed circular aperture with a diameter of 5 pixels, which roughly corresponds to the average seeing on the nights of

our observations. The apparent magnitude m of an object in an image is $m = m_0 - 2.5\log_{10}(f) = m_0 + m_s$, where f is the measured flux, m_0 is the zero-point magnitude of the image, and the survey magnitude has been defined as $m_s \equiv -2.5\log_{10}(f)$. For each exposure, following the methods of Wong & Brown (2015), we calculated the zero-point magnitude of each chip by matching all non-saturated sources detected by SExtractor to reference stars in the Sloan Digital Sky Survey Data Release 9 (SDSS DR9) catalog and carrying out a linear fit with slope set to unity through the points (m_s, m). When calibrating images in the HSC g and i filters, we used SDSS g-band and i-band star magnitudes, respectively. The resulting apparent magnitudes are therefore benchmarked to the SDSS photometric system. We computed the corresponding uncertainties in the apparent magnitude using standard error propagation techniques.

We compared the positions of the KBOs detected by our survey with those of previously discovered KBOs listed in the Minor Planet Center catalog for the nights of our observations. Ten objects were matched to known KBOs (see Supplemental Table).

6.3 Data analysis

KBO color distribution

From the apparent g and i magnitudes obtained through our photometric calibration (generally two in each band, unless masked due to a problematic detection in one exposure), we computed error-weighted mean g and i magnitudes for each object, from which we subsequently derived the $g - i$ color. The uncertainty in color σ_{g-i} is given by the quadrature sum of the individual g and i mean magnitude errors.

Asteroid rotation during the approximately 4 hour observational arc of each detected object can entail an additional contribution to the color uncertainty. We followed the methods of Wong & Brown (2015) and utilized the repeated observations in each band to empirically determine the rotational contribution to the color uncertainty. The standard deviation of differences between two consecutive g-band magnitude measurements contains a contribution from the photometric uncertainties of the individual magnitude measurements alone (given by the quadrature sum of the individual magnitude uncertainties), as well as any additional contribution from magnitude modulation of the object due to rotation. When comparing the standard deviation of g-band magnitude differences (binned by 0.5 mag intervals) with the corresponding photometric error contribution, we found that the values were com-

parable; in other words, the photometric error contribution does not systematically underestimate the standard deviation values. The same conclusion was reached for i-band. Therefore, we find that asteroid rotation does not have an appreciable effect on the color measurements overall.

Only two KBOs detected by our survey and matched with known objects have previous color measurements — 2000 QN251 and 2005 SC278. Both of these KBOs were observed and analyzed by Sheppard (2012), who reported $g - i$ colors of 1.21 ± 0.07 and 1.51 ± 0.04, respectively. The colors that we measured are 1.73 ± 0.05 and 1.40 ± 0.03, respectively. While the colors measured for 2005 SC278 are comparable, our measured color for 2000 QN251 is much redder than the earlier measurement.

2000 QN251 is one of the brightest objects detected by our survey, with calculated g, g, i, i magnitudes of 24.3, 24.4, 22.6, 22.6, respectively. All four images had comparable seeing, and our computed absolute magnitude (derived from interpolation of g- and i-band magnitudes) matches the value listed by the Minor Planet Center. Our reported magnitude values preclude any rotational modulation in apparent magnitude between consecutive images taken in the same band. We suggest that the discrepancy between the measured colors in our work and Sheppard (2012) may be due to inconsistent observing conditions during the previous observation or a different observing cadence, which may have led to a rotational contribution to the Sheppard (2012) color measurement. We note that neither 2000 QN251 nor 2005 SC278 is a hot KBO, so they are not included in the color-magnitude analysis in this paper.

The distribution of colors $g-i$ for all the hot KBOs detected by our survey is shown in Figure 6.3 with the unfilled histogram. The bimodality of the distribution is clearly discernible, with two color modes centered at around $g - i = 0.9$ and $g - i = 1.3$. Moreover, the bimodality is present throughout the entire magnitude range covered by our survey ($H = 6.5 - 10.4$). This color distribution is indicative of two sub-populations within the small hot KBO population whose members have characteristically different surface colors. Hereafter, we refer to these sub-populations as the red (R) and very red (VR) KBOs.

To carry out a more detailed analysis of the individual sub-populations, we first filter our survey KBO dataset by removing the low signal-to-noise objects. The photometric errors of the detected objects become large with decreasing apparent brightness; the color uncertainties are also increased for objects located in images

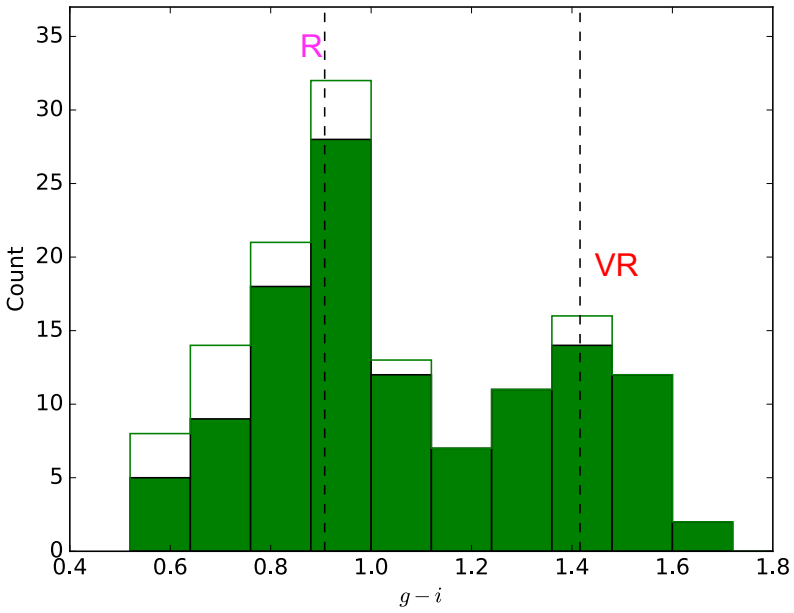

Figure 6.3: Histogram of $g-i$ colors for hot KBOs detected in our survey: the unfilled graph shows the distribution of all 136 objects in the dataset, while the filled graph shows the distribution of only the 118 objects with color uncertainties $\sigma_{g-i} \leq 0.15$. A robust bimodality is evident in both distributions, dividing the objects into two sub-populations — red (R) and very red (VR). The vertical dashed lines indicate the computed mean colors of the R and VR sub-populations — $\overline{(g-i)}_R = 0.91$ and $\overline{(g-i)}_{VR} = 1.42$.

that were obtained when the seeing was poor. A sizeable fraction of the objects in the survey KBO dataset have color uncertainties that are comparable to the difference between the two color modes. These large uncertainties contribute additional scatter to the color distribution and prevent clear categorization of those objects as R or VR. For the results presented below, we constructed a filtered KBO dataset by only considering the 118 objects with $\sigma_{g-i} \leq 0.15$.

The color distribution of objects in the filtered KBO dataset is shown by the solid histogram in Figure 6.3. To quantitively determine the mean colors of the R and VR sub-populations, we followed the technique employed in our past studies of bimodal asteroid populations (Wong et al. 2014; Wong & Brown 2015) and fit the filtered KBO color distribution to a two-peaked Gaussian probability function. A standard log-probability minimization yielded the mean R and VR colors: $\overline{(g-i)}_R = 0.91$ and $\overline{(g-i)}_{VR} = 1.42$. The standard deviation of the two color modes are $\sigma_{g-i,R} = 0.12$

and $\sigma_{g-i,VR} = 0.09$, respectively.

This normal mixture model fitting also allows us to determine the significance of the bimodality. We computed the Bayesian Information Criterion (BIC) for both unimodal and bimodal distribution fits to the KBO color distribution. The BIC is defined as BIC $\equiv -2\log(L) + k\log(n)$, where L is the likelihood of the best-fit solution, k is the number of free parameters, and n is the number of data points. The difference in BIC between the unimodal and bimodal fits is ΔBIC= 23.0, which shows that the bimodal interpretation is very strongly favored (ΔBIC> 5 indicates a strong preference for the model with smaller BIC).

Having established the mean colors, we can now sort individual objects into the R and VR sub-populations based on their measured colors. We classified all objects in the filtered KBO dataset with $g - i \leq \overline{(g-i)}_R + \sigma_{g-i,R} = 1.03$ as R and all objects with $g - i \geq \overline{(g-i)}_{VR} - \sigma_{g-i,VR} = 1.31$ as VR. While our previous studies used the mean colors as the cutoff locations for classifying objects into sub-populations, limiting the filtered KBO dataset to just objects with $\sigma_{g-i} \leq 0.15$ enabled us to extend our categorization into the region between the two mean colors. As a result, we categorized 63 objects as R and 30 objects as VR.

Magnitude distributions

Our moving object detection procedure returned the right ascension and declination of all objects in each of the four exposures taken at the corresponding fields. From here, we converted to geocentric ecliptic coordinates to obtain the ecliptic longitude λ and latitude β of every object. Having computed the heliocentric distance d through our orbit fitting routine (Section 6.2), we calculated the geocentric distance Δ of each object using standard coordinate transformations:

$$\Delta = r_S \cos(\beta)\cos(\lambda - \lambda_S) + \sqrt{r_S^2\left[\cos^2(\beta)\cos^2(\lambda - \lambda_S) - 1\right] + d^2}, \tag{6.1}$$

where r_S and λ_S are the geocentric distance and geocentric ecliptic longitude of the Sun at the time of each observation. We first interpolated the fluxes in g-band and i-band to derive the V-band apparent magnitude, v, for each object, following the spectral slope computation described in Section 6.4. Next, we converted the apparent v magnitudes to absolute H magnitudes via

$$H = v - 2.5\log_{10}(d^2\Delta^2). \tag{6.2}$$

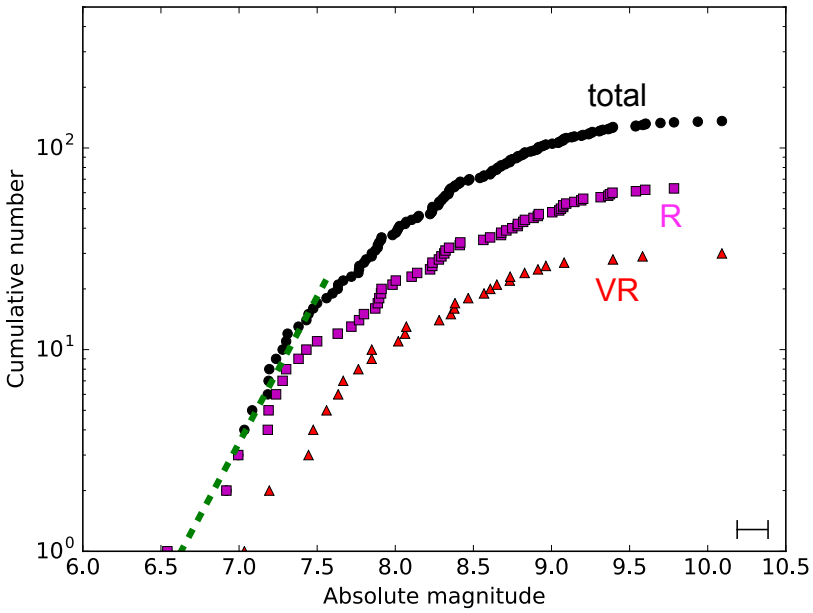

Figure 6.4: Absolute H magnitude distributions of the total survey hot KBO dataset (black points), as well as the categorized R and VR sub-populations (magenta squares and red triangles, respectively). The error bar in the lower right represents the typical magnitude uncertainty: 0.2 mag. The two color-magnitude distributions have very similar shapes throughout the entire magnitude range. The dashed green line indicates the best-fit power law distribution to the total magnitude distribution through $H_{\rm max} = 7.5$, which has a power law slope of $\alpha = 1.45$.

For the identified KBOs in our dataset with previously obtained visible-band or multi-band photometry, our calculated absolute magnitudes agree the Minor Planet Center magnitudes to within 0.3 mag.

Figure 6.4 shows the cumulative absolute magnitude distribution $N(H)$ of all objects in our survey KBO dataset (black points). The gentle rollover starting at $H \sim 8.0$ indicates the onset of detection incompleteness in our survey. The magnitude distribution of KBOs has been the subject of intensive study over the last decade, with numerous dedicated surveys having been undertaken to explore the shape of the distribution through $H = 11-12$. Many recent published works in the literature present incompleteness-corrected KBO magnitude distributions extending well beyond the completeness limit of our photometric survey (e.g., Fraser et al. 2008; Shankman et al. 2016).

For the sake of comparison with previous studies of the hot KBO population, we

chose a conservative threshold magnitude of $H_{\rm max} = 7.5$ and fit the differential magnitude distribution, $\Sigma(H) = dN(H)/dH$, of our survey KBOs through $H_{\rm max}$ with a single power law distribution of the form $\Sigma(\alpha, H_0|H) = 10^{\alpha(H-H_0)}$, where α is the power law slope, and H_0 is the normalization magnitude for which $\Sigma(H_0) = 1$. Following the methods described in Wong & Brown (2015), we used a Markov Chain Monte Carlo algorithm to estimate the best-fit parameters and corresponding 1σ uncertainties, which yielded $\alpha = 1.45^{+0.40}_{-0.37}$. This value is steeper than the slope of $0.87^{+0.07}_{-0.2}$ reported by Fraser et al. (2008) for the same magnitude range, though still consistent at the 1.5σ level.

Our analysis of the $g - i$ color distribution and the classification of individual hot KBOs as R or VR allow us carry out the first study of the individual magnitude distributions of the R and VR color sub-populations. The cumulative absolute magnitude distributions of the categorized R and VR KBOs are shown in Figure 6.4. It is immediately apparent that the R and VR magnitude distributions have nearly identical shapes throughout the enter magnitude range covered by our survey. The similarity between the R and VR magnitude distributions has important implications regarding the origin of the color bimodality, which we discuss in the next section.

Although not all KBOs in our filtered sample were classified as R or VR due to their intermediate measured colors, this incompleteness in categorization is magnitude-independent and therefore has no effect on the relative shapes of the color-magnitude distributions. Meanwhile, non-uniform seeing and differing g- and i-band signal-to-noise can cause survey biases. Among the objects in our filtered sample, the majority had the worst seeing during g-band observations (see supplemental table). Overall, when the seeing during g-band and i-band observations were comparable, the signal-to-noise is slightly lower in g-band. Both of these trends establish g as the limiting band for detection. For a KBO with a given absolute magnitude near the detection limit, R objects are roughly 0.1 mag brighter in g-band than VR objects.

Thus, we conclude that our survey has a bias toward R objects. We note, however, that this bias only affects the faintest objects in our sample. Therefore, the relative shape of the R and VR magnitude distributions and the R-to-VR number ratio among the brightest objects should not be influenced by the bias.

We used mean R and VR geometric albedos from the literature ($p_{v,R} = 0.06$ and $p_{v,VR} = 0.12$, respectively, as computed in Fraser et al. 2008) to convert absolute magnitudes to approximate diameters via the relation $D = 1329 \times 10^{-H/5}/\sqrt{p_v}$ km. To obtain our first estimate of the R-to-VR number ratio r, we considered only

categorized KBOs larger than 100 km in diameter, corresponding to threshold absolute magnitudes of $H = 8.7$ and $H = 7.9$ for R and VR objects, respectively. In this range, we detected 36 R and 10 VR objects, corresponding to $r = 3.6$. Since our method for classifying of objects into sub-populations relied on the results of a double Gaussian fit, the number ratio we calculate can be affected by deviations in the measured color distribution from a true two-peaked Gaussian shape (e.g., slight asymmetries relative to mean R and VR colors).

As a second estimate of the R-to-VR number ratio, we calculated the error-weighted mean color of all 46 objects in our filtered KBO sample larger than 100 km — $\overline{g-i} = 1.04$. We modeled the mean color as a mixture of R and VR objects with typical colors $\overline{(g-i)}_R = 0.91$ and $\overline{(g-i)}_{VR} = 1.42$, respectively: $\overline{g-i} = q \times \overline{(g-i)}_R + (1-q) \times \overline{(g-i)}_{VR}$, where q is the R object fraction and is related to r via $r = q/(1-q)$. Through this procedure, we obtained $r = 3.0$. Acknowledging the sensitivity of the computed number ratio to the particular method of calculation, we give the general conclusion that the R hot KBO sub-population is roughly three to four times the size of the VR sub-population.

6.4 Discussion

Our two-day HSC survey represents the most systematic photometric survey of small KBOs to date, greatly increasing the number of measured KBO colors for objects fainter than $H \sim 7$. We demonstrated incontrovertibly for the first time the robust bimodality in optical color among small KBOs in the hot population. The classification of objects into the R and VR sub-populations also enabled the first look at the individual color-magnitude distributions. Building on the analysis presented in the previous section, we are now in a position to compare the small hot KBOs to other populations and discuss the origin of the attested color bimodality.

Comparison with Centaurs

Constraining for relatively high signal-to-noise objects via the condition $\sigma_{g-i} \leq 0.15$, we obtained a filtered KBO set of 118 objects (Section 6.3). Applying the same constraint to the 16 Centaurs detected by our survey yields 15 objects.

In order to combine our data with previously published color measurements of Centaurs and hot KBOs compiled in the literature, we must convert our $g-i$ colors to spectral slopes S. We followed the prescription described in detail in Wong et al. (2014) and first converted the measured apparent magnitudes to flux, normalizing to unity in g band: $F_g = 1$, $F_i = 10^{0.4((g-i)-0.55)}$, where we have removed the solar

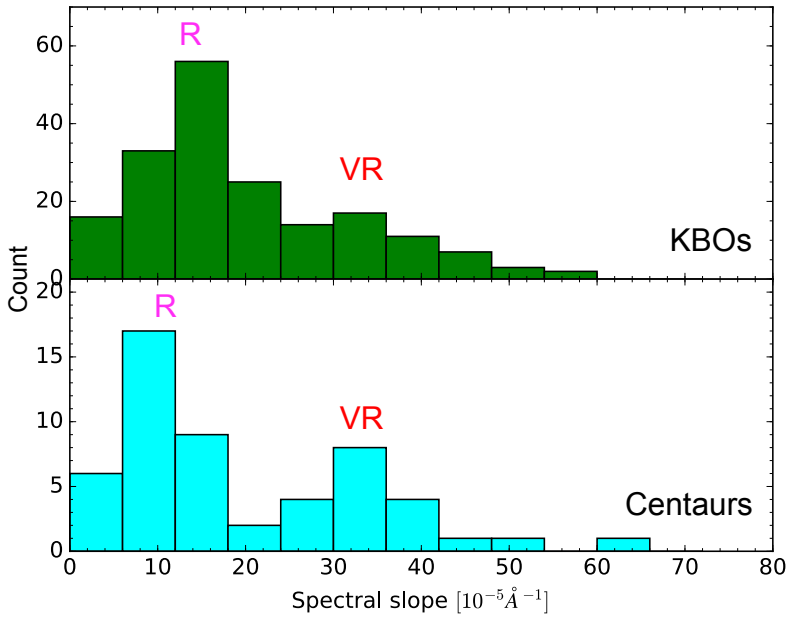

Figure 6.5: Top panel: spectral slope distribution of 200 hot KBOs, incorporating objects in the filtered KBO dataset from our survey as well as objects contained in the Peixinho et al. (2015) database spanning the same magnitude range. Bottom panel: same as top panel, but for 53 Centaurs detected by our survey or listed in the Peixinho et al. (2015) database (with $H \geq 7$). All of these spectral slope values have uncertainties less than 10×10^{-5} Å^{-1}. Both spectral slope distributions are bimodal, with the R and VR modes in each population located at similar spectral slope values.

$g - i$ color (Ivezić et al. 2001). The associated relative flux uncertainties were computed using the second-order method of Roig et al. (2008): $\Delta F_g/F_g = \sqrt{2}\sigma_g$, $\Delta F_i/F_i = 0.9210\sigma_{g-i}(1+0.4605\sigma_{g-i})$. We then calculated the spectral slope S using standard linear regression.

We queried the database of objects analyzed in Peixinho et al. (2015) for hot KBOs (inclinations greater than or equal to 5°; Section 6.2) and Centaurs, both with the condition $H \geq 7$, finding 82 and 38 objects, respectively. Combining these objects with our survey data, we constructed a total spectral slope dataset for 200 hot KBOs and 53 Centaurs. The corresponding spectral slope distributions are shown in Figure 6.5.

We note that the transformation from $g - i$ color to S is not linear, with the distance between spectral slope values corresponding to evenly spaced $g-i$ color values being

amplified as the color becomes redder. As a result, the shape of the VR mode in the spectral slope distribution is broad and noticeably asymmetric, as opposed to the shape of the analogous peak in the $g - i$ color distribution (Figure 6.3). This serves to reduce the saliency of the bimodality in the spectral slope distribution. However, even with this effect, the bimodality in spectral slope among the hot KBOs is still discernible.

The bimodality in spectral slope among the Centaurs is well-attested by numerous previous studies (e.g., Peixinho et al. 2003; Barucci et al. 2005; Perna et al. 2010). The comparison of Centaurs with hot KBOs demonstrates that not only is the hot KBO spectral slope distribution also bimodal, the two color modes closely correspond in location to the two color modes in the Centaur spectral slope distribution. In other words, the R and VR Centaurs (often referred to as gray/neutral and red in the literature) have the same colors as R and VR hot KBOs.

From this observation, we can conclusively resolve the issue of the color bimodality of Centaurs in this magnitude range (which includes all known Centaurs except Chariklo and Chiron) —- before being scattered inward onto their current comet-like orbits, R and VR Centaurs were members of the R and VR hot KBO subpopulations, respectively, as previously suggested by Fraser & Brown (2012) and Peixinho et al. (2012).

Comparison with larger hot KBOs

We also place the color data of small KBOs from our survey in the context of the wider hot KBO population as a whole. Figure 6.6 shows the color-magnitude distribution of all hot KBO and Centaurs with spectral slope errors less than 10×10^{-5} Å^{-1}. The plot illustrates how our survey data extends the known body of high quality KBO color measurements into the size region that had previously only been adequately studied using Centaur colors as proxy.

For both hot KBOs and Centaurs, a bimodality in color is evident at all magnitudes among objects fainter than $H \sim 7$, as was discussed in Section 6.4. The Subaru hot KBO data nearly triple the number of high signal-to-noise KBO color measurements between $H = 7$ and $H = 9$ contained in the Peixinho et al. (2015) database and are instrumental in solidifying the observation of bimodality in that size range, which was previously hinted at using far fewer data points (Fraser & Brown 2012; Peixinho et al. 2012; Peixinho et al. 2015).

Notably, however, the colors of larger, brighter hot KBOs show a more uniform

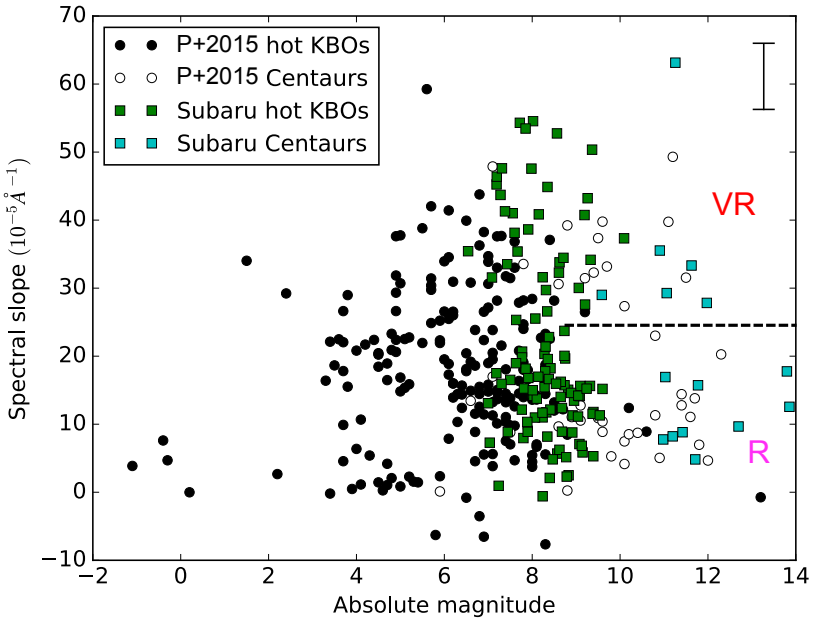

Figure 6.6: Color-magnitude plot for hot KBOs and Centaurs combining data tabulated in Peixinho et al. (2015) (dots) and the results of our Subaru survey (squares). Only spectral slope measurements with uncertainties less than 10×10^{-5} Å^{-1} are included; error bars on data points are omitted for the sake of clarity, with the size of the maximum uncertainty indicated by the example error bar in the upper right. Bimodality in color is discernible among all objects fainter than $H \sim 7$. The horizontal dashed line indicates the approximate boundary between R and VR colors. Meanwhile, the larger hot KBOs display a uniform color distribution, with the exception of a small clustering of neutral colored objects in the range $H = 2 - 6$ that is dominated by Haumea collisional family members.

distribution, with many objects having spectral slope values intermediate between the two color types. The apparent clustering of near-neutral objects between $H = 2$ and $H = 6$ is primarily due to the presence of the Haumea collisional family. Previous studies have shown that, omitting the Haumea family members, no significant bimodality is present among objects brighter than $H \sim 6$ (Fraser & Brown 2012; Peixinho et al. 2012; Peixinho et al. 2015). In other words, only small hot KBOs are bimodal in color.

The threshold of $H \sim 6$ corresponds to a diameter of roughly $300 - 400$ km. Observations of these large- and intermediate-sized objects have revealed somewhat higher albedos than their smaller counterparts (Stansberry et al. 2006). This suggests that the larger KBOs have fundamentally different surface properties than the objects

covered by our survey. The discrepancy may be due to the effects of secondary processes since formation, such as the onset of cryovolcanism or differentiation, which would not have occurred in smaller bodies (see, for example, discussion in Fraser & Brown 2012).

Comparison with Jupiter Trojans

Recent theories of solar system evolution posit that a mean motion resonance crossing between Jupiter and Saturn roughly 600 Myr after the formation of the solar system led to significant alterations in the orbital architecture of the giant planets (Morbidelli et al. 2005; Gomes et al. 2006; Tsiganis et al. 2005). An important consequence of this dynamical restructuring is the scattering of the primordial body of planetesimals that were situated beyond the orbits of the ice giants. While the majority of the mass within this region was expelled from the solar system as the orbits of the ice giants expanded, a fraction of the planetesimals were scattered outward to become the present-day Kuiper Belt. The remainder was scattered inward and eventually captured into resonance with Jupiter to become the Trojan asteroids. Therefore, the current paradigm of solar system evolution predicts a common origin for Jupiter Trojans and KBOs.

Several authors have previously noted that the overall magnitude distributions of Trojans and hot KBOs brighter than $H \sim 8-9$ are similar (e.g., Fraser et al. 2008). In Wong et al. (2014), we reported a power law slope of 1.11 ± 0.20[1] for Trojans brighter than $H \sim 8$. In our present study, we obtained a best-fit magnitude distribution slope of $1.45^{+0.40}_{-0.37}$ for hot KBOs brighter than $H = 7.5$. The comparison demonstrates that the bright hot KBOs and Trojans of the same size have statistically indistinguishable magnitude distributions.

Similar to the KBOs, the Trojans display a robust optical color bimodality, albeit with the peaks of the modes centered at bluer colors ($g-i = 0.73$ and 0.86; Wong & Brown 2015). In Wong et al. (2014), we categorized Trojans into the two respective color sub-populations and analyzed the individual color-magnitude distributions. We showed that the two Trojan sub-populations have statistically indistinguishable magnitude distributions in the bright end ($H < 9$), just as the R and VR hot KBO sub-populations have nearly identical magnitude distribution shapes throughout the brightness range covered by our survey (Section 6.3).

[1] In Wong et al. (2014), the uncertainty in the slope was reported erroneously as 0.02, instead of the correct value 0.20.

Taken together, the analyses of Trojans and KBOs provide strong evidence to support one of the key predictions of current models of solar system evolution. Not only are the overall magnitude distributions of the hot KBOs and Trojans similar, but the individual constituent color sub-populations have comparable magnitude distributions. Therefore, we can posit that each of the two sub-populations in the Trojans and hot KBOs are sourced from a single progenitor body of planetesimals.

Origin of the color bimodality

The bimodal color distribution of hot KBOs is indicative of two different surface types, with distinct photometric properties. There are two classes of possible explanations for the origin of the observed color bimodality: (1) the R and VR KBOs formed in different regions of the protoplanetary disk and were sourced from material with different bulk compositions, and (2) the R and VR KBOs formed in the same region of the disk and out of the same material, but later developed distinct surface properties via some secondary evolutionary process.

The size distribution, or by proxy, the magnitude distribution, of a population contains information about both the accretion environment and the subsequent collisional evolution of the population. Therefore, the color-magnitude distributions we derived in our analysis are a crucial tool in helping us understand how the color bimodality developed.

In Figure 6.4, we showed that the R and VR hot KBO magnitude distributions are nearly identical in shape, which suggests that the two sub-populations have undergone a similar formation and evolutionary history and therefore likely formed out of the same body of material within the protoplanetary disk. This similarity in magnitude distribution shape contrasts with, for example, the strong discrepancy between the hot and cold KBO magnitude distributions (e.g., Fraser et al. 2008).

In Wong & Brown (2016), we proposed a simple hypothesis, that accounts for the development of a color bimodality within the primordial planetesimal disk beyond the orbits of the ice giants. Assuming the dynamical framework of the Nice model, the model describes a primordial body of material situated between 15 and roughly 30 AU, from which the modern hot KBO population is sourced (e.g., Morbidelli et al. 2005; Levison et al. 2008). After a residence time of roughly 600 Myr (Gomes et al. 2006), a period of chaotic dynamical evolution throughout the outer Solar System scattered a fraction of these objects into the current Kuiper Belt region (see discussion in previous subsection).

The hypothesis posits that all the bodies within the primordial trans-Neptunian disk accreted with a roughly cometary composition, i.e., rocky material and water ice, with a significant volume of other volatile ices such as carbon dioxide, methanol, ammonia, hydrogen sulfide, etc. During the accretion process, large objects migrated differentially through the disk (e.g., Kenyon et al. 2008), so that the overall disk was well-mixed compositionally, with a single characteristic size distribution. Once these bodies were exposed to insolation after the dispersal of the gas disk, sublimation-driven loss of volatiles from the outermost layers led to the development of distinct surface compositions throughout this region.

The loss rate of each individual volatile ice species is correlated with its vapor pressure, which in turn has a strong exponential dependance on temperature. As a result, each volatile ice species would have a sublimation line at a different location within the primordial disk: objects situated inward of the line became depleted in that species on their surfaces, while objects situated beyond the line retained that species on their surfaces.

From our modeling, we found that the sublimation line of hydrogen sulfide ice (H_2S) passed through the region of the primordial trans-Neptunian planetesimal disk. Therefore, objects within this single primordial population would have been divided into two groups: those that retained H_2S on their surfaces, and those that did not. Previous experimental work has shown that irradiation of volatile ices leads to a general redding of the optical spectral slope (e.g., Brunetto et al. 2006). We posited that the presence of H_2S on the surface of an object would contribute additional reddening relative to case where H_2S was absent. H_2S is known to induce a strong reddening of the surface upon irradiation, as has been observed in the H_2S frost deposits on Io (Carlson et al. 2007).

After the Nice model dynamical instability, some objects in the trans-Neptunian region were scattered outward, sharing a common size distribution by virtue of their common formation environment while inheriting the surface color bimodality that developed in the primordial planetesimal disk due to differential loss/retention of H_2S. Likewise, some objects were scattered inward to eventually settle into resonance with Jupiter, thereby explaining the observed color bimodality in the Trojans and the similarity in magnitude distributions between the color sub-populations of the Trojans and hot KBOs. In Wong & Brown (2016), we speculate that the bluer colors of the two Trojan sub-populations may be due to secondary processing of the irradiated surfaces following their emplacement into a higher-temperature

environment at 5.2 AU.

6.5 Conclusion

In this paper, we presented the results of a wide-field photometric survey of KBOs carried out using the Subaru/HSC instrument. Over the course of two nights of observation, we imaged 356 KBOs in the g and i filters, from which we obtained the $g - i$ colors. After constraining our dataset to the hot KBO population (objects with inclination greater than or equal to 5°) and filtering out low signal-to-noise detections, we examined the resulting color distribution of 118 objects and provided the first separate analysis of the magnitude distributions of the two attested sub-populations within the hot KBO population — the R and VR sub-populations. The main conclusions are summarized below:

- The optical color distribution of hot KBOs shows a robust bimodality across the entire magnitude range covered by our survey ($H > 6.5$). The two modes in the color distribution correspond to the R and the VR sub-populations and have mean colors of $\overline{(g-i)}_R = 0.91$ and $\overline{(g-i)}_{VR} = 1.42$, respectively.

- The absolute magnitude distributions of the R and VR sub-populations are nearly identical in shape throughout the magnitude range covered by our survey. The estimated R-to-VR number ratio is between 3-to-1 and 4-to-1.

- The color distributions of Centaurs and similarly-sized hot KBOs are comparable in shape. The locations of the R and VR color modes are similar for both populations and indicate that the R and VR Centaurs are sourced from the R and VR hot KBO sub-populations, respectively.

- Unlike their smaller counterparts, hot KBOs larger than $H \sim 6$ have a more uniform color distribution when excluding the neutral-colored members of the Haumea collisional family.

- The magnitude distributions of the R and VR hot KBOs are similar to the magnitude distributions of the two color sub-populations attested in the Jupiter Trojans, suggesting a common origin for the individual color sub-populations, as predicted by recent theories of solar system evolution.

- The similarity between the R and VR KBO magnitude distributions suggests that the two sub-populations share a single progenitor population and have undergone similar formation and evolutionary histories. We hypothesize that

the color bimodality arose due to location-dependent retention vs. loss of H_2S on the surfaces of these bodies in the early Solar System, prior to the onset of dynamical instability that emplaced them into their current location.

References

Barucci, M. A., Belskaya, I. N., Fulchignoni, M., & Birlan, M. (2005). "Taxonomy of Centaurs and trans-Neptunian objects". *AJ*, 130, 1291.

Bernstein, G. M., Trilling, D. E., Allen, R. L., & Brown, M. E. (2004). "The size distribution of trans-Neptunian bodies". *AJ*, 128, 1364.

Bertin, E. (2006). "Automatic Astrometric and Photometric Calibration with SCAMP". In: *Astronomical Data Analysis Software and Systems XV (ASP Conf. Ser. 351)*. Eds. Gabriel, C., Arviset, C., Ponz, D., & Enrique, S. (San Francisco, CA: ASP), 112.

Bertin, E. & Arnouts, S. (1996). "SExtractor: Software for source extraction". *A&AS*, 117, 393.

Brown, M. E. (2012). "The compositions of Kuiper Belt objects". *Annual Rev. of Earth and Planetary Sci.* 40, 467.

Brunetto, R., Barucci, M. A., Dotto, E., & Strazzulla, G. (2006). "Ion irradiation of frozen methanol, methane, and benzene: Linking to the colors of Centaurs and trans-Neptunian objects". *ApJ*, 644, 646.

Carlson, R. W., Kargel, J. S., Douté, S., Soderblom, L. A., & Brad Dalton, J. (2007). "Io's Surface Composition". In: *Io After Galileo*. Eds. Lopes, R. M. C. & Spencer, J. R. (Chichester, UK: Praxis Publishing Ltd), 194.

Fraser, W. C. & Brown, M. E. (2012). "The Hubble Wide Field Camera 3 test of surfaces in the outer Solar System: The compositional classes of the Kuiper Belts". *ApJ*, 749, 33.

Fraser, W. C., Kavelaars, J. J., Holman, M. J., et al. (2008). "The Kuiper belt luminosity from m_R = 21 to 26". *Icarus*, 195, 827.

Gomes, R., Levison, H. F., Tsiganis, K., & Morbidelli, A. (2006). "Origin of the cataclysmic Late Heavy Bombardment period of the terrestrial planets". *A&A*, 455, 725.

Hainaut, O. R., Boehnhardt, H., & Protopapa, S. (2012). "Colours of minor bodies in the outer solar system. II. A statistical analysis revisited". *A&A*, 546, A115.

Ivezić, Ž., Tabachnik, S., Rafikoc, R., & al., et (2001). "Solar System Objects Observed in the Sloan Digital Sky Survey Commissioning Data". *AJ*, 122, 2749.

Kenyon, S. J., Bromley, B. C., O'Brien, D. P., & Davis, D. R. (2008). "Formation and collisional evolution of Kuiper Belt objects". In: *The Solar System Beyond Neptune*. Eds. Barucci, M. A., Boehnhardt, H., Cruikshank, D. P., Morbidelli, A., & Dotson, R. (Tucson, AZ: University of Arizona Press), 293.

Lacerda, P., Fornasier, S., Lellouch, E., & Kiss, C. (2014). "The albedo-color diversity of Transneptunian objects". *ApJ*, 793, L2.

Levison, H. F., Morbidelli, A., Van Laerhoven, C., & Gomes, R. (2008). "Origin of the structure of the Kuiper belt during a dynamical instability in the orbits of Uranus and Neptune". *Icarus*, 196, 258.

Melita, M. D., Licandro, J., Jones, D. C., & Williams, I. P. (2008). "Physical properties and orbital stability of the Trojan asteroids". *Icarus*, 195, 686.

Miyazaki, S., Komiyama, Y., Sekiguchi, M., & Okamura, S. (2002). "Subaru Prime Focus Camera – Suprime-Cam". *Publ. Astron. Soc. Japan*, 54, 833.

Morbidelli, A., Levison, H. F., Tsiganis, K., & Gomes, R. (2005). "Chaotic capture of Jupiter's Trojan asteroids in the early Solar System". *Nature*, 435, 462.

Peixinho, N., Delsanti, A., & Doressoundiram, A. (2015). "Reanalyzing the visible colors of Centaurs and KBOs: what is there and what we might be missing". *A&A*, 577, A35.

Peixinho, N., Delsanti, A., Guilbert-Lepoutre, A., Gafeira, R., & Lacerda, P. (2012). "The bimodal colors of Centaurs and small Kuiper Belt objects". *A&A*, 546, A86.

Peixinho, N., Doressoundiram, A., Delsanti, A., & Boehnhardt, H. (2003). "Reopening the TNOs color controversy: Centaurs bimodality and TNOs unimodality". *A&A*, 410, L29.

Perna, D., Barucci, M. A., Fornasier, S., & DeMeo, F. E. (2010). "Colors and taxonomy of Centaurs and trans-Neptunian objects". *A&A*, 510, A53.

Roig, F., Ribeiro, A. O., & Gil-Hutton, R. (2008). "Taxonomy of asteroid families among the Jupiter Trojans: comparison between spectroscopic data and the Sloan Digital Sky Survey colors". *A&A*, 483, 911.

Shankman, C., Kavelaars, JJ., Gladman, B. J., & Alexandersen, M. (2016). "OSSOS. II. A sharp transition in the absolute magnitude distribution of the Kuiper Belt's scattering population". *AJ*, 151, 31.

Sheppard, S. S. (2012). "The color differences of Kuiper Belt objects in resonance with Neptune". *AJ*, 144, 169.

Stansberry, J. A., Grundy, W. M., & Margot, J. L. (2006). "The albedo, size, and density of binary Kuiper Belt object (47171) 1999 TC_{36}". *ApJ*, 643, 556.

Tsiganis, K., Gomes, R., Morbidelli, A., & Levison, H. F. (2005). "Origin of the orbital architecture of the giant planets of the Solar System". *Nature*, 435, 459.

Wong, I. & Brown, M. E. (2015). “The color-magnitude distribution of small Jupiter Trojans”. *AJ*, 150, 174.

Wong, I. & Brown, M. E. (2016). “A hypothesis for the color bimodality of Jupiter Trojans”. *AJ*, 152, 90.

Wong, I., Brown, M. E., & Emery, J. P. (2014). “The differing magnitude distributions of the two Jupiter Trojan color populations”. *AJ*, 148, 112.

Chapter 7

0.7 – 2.5 μm SPECTRA OF HILDA ASTEROIDS

Wong, I., Brown, M. E., & Emery, J. P. (2017). "0.7 – 2.5 μm spectra of Hilda asteroids". *AJ*, 154, 104.

ABSTRACT

The Hilda asteroids are primitive bodies in resonance with Jupiter whose origin and physical properties are not well understood. Current models posit that these asteroids formed in the outer Solar System and were scattered along with the Jupiter Trojans into their present-day positions during a chaotic episode of dynamical restructuring. In order to explore the surface composition of these enigmatic objects in comparison with an analogous study of Trojans (Emery et al. 2011), we present new near-infrared spectra (0.7–2.5 μm) of 25 Hilda asteroids. No discernible absorption features are apparent in the data. Synthesizing the bimodalities in optical color and infrared reflectivity reported in previous studies, we classify 26 of the 28 Hildas in our spectral sample into the so-called less-red and red sub-populations and find that the two sub-populations have distinct average spectral shapes. Combining our results with visible spectra, we find that Trojans and Hildas possess similar overall spectral shapes, suggesting that the two minor body populations share a common progenitor population. A more detailed examination reveals that while the red Trojans and Hildas have nearly identical spectra, less-red Hildas are systematically bluer in the visible and redder in the near-infrared than less-red Trojans, indicating a putative broad, shallow absorption feature between 0.5 and 1.0 μm. We argue that the less-red and red objects found in both Hildas and Trojans represent two distinct surface chemistries and attribute the small discrepancy between less-red Hildas and Trojans to the difference in surface temperatures between the two regions.

7.1 Introduction

The Hilda asteroids are a large population of minor bodies located in the 3:2 mean-motion resonance with Jupiter. These objects orbit within a relatively narrow range

of heliocentric distances around 4.0 AU, between the outer edge of the Main Belt (roughly 3.3 AU) and Jupiter's orbit (5.2 AU). and Early theories of solar system formation posited that the Hildas originated in the middle Solar System and were captured into their present-day orbits during a period of smooth migration (e.g., Franklin et al. 2004). However, recent advances in our understanding of solar system evolution have placed Hildas in a new light. Current models describe a scenario in which the gas giants crossed a mutual mean-motion resonance sometime after the era of planet formation, triggering chaotic alterations throughout the Solar System (e.g., Morbidelli et al. 2005). These models predict that a significant fraction of planetesimals that formed beyond the primordial orbits of the ice giants was scattered inward during the period of dynamical instability and now resides in the middle Solar System (Gomes et al. 2006).

In particular, simulations carried out within this dynamical framework have demonstrated that the present-day Hildas and Jupiter Trojan, both resonant asteroid populations in the vicinity of Jupiter, should be composed almost exclusively of objects from the outer Solar System (Roig & Nesvorný 2015). Such a scenario also points toward a common progenitor population for the Kuiper Belt objects, Trojans, and Hildas, presenting the enticing possibility that studying the surface properties of the more readily accessible Hildas could give insight into the composition of all three populations. The compositional characterization of Hildas and comparison with the properties of Trojans serve as a powerful observational test for probing the veracity of current dynamical instability models.

At present, the composition of Hildas, and indeed that of all other middle and outer solar system minor bodies, remains a subject of much speculation. The general compositional outline for these asteroids posits a mixture of water ice, anhydrous silicates, and organics (e.g., Vilas et al. 1994; Emery & Brown 2003; Yang & Jewitt 2007). Observational studies of Hildas have hitherto revealed largely featureless, reddish spectra in the optical and near-infrared (Dahlgren & Lagerkvist 1995; Dahlgren et al. 1997; Takir & Emery 2012) and very low albedos averaging around 4% (Ryan & Woodward 2011). Taxonomically, Hildas are predominantly D- and P-type asteroids, with a small fraction of C-type objects (Grav et al. 2012). Further into the infrared, a handful of published Hilda spectra reveal a broad, rounded feature centered at around 3 μm, which has been interpreted to be due to a thin layer of water frost coating a dark-grained regolith (Takir & Emery 2012). A study of a similar feature on Trojans shows that this feature could also be consistent with

ammonia ice or irradiation products thereof (Brown et al. 2011); such a surface chemistry would naturally point toward an outer solar system origin.

Analysis of optical colors derived from Sloan Digital Sky Survey photometry and infrared reflectivities measured by the Wide-field Infrared Survey Explorer reveals a strong bimodality among both Hildas (Gil-Hutton & Brunini 2008; Wong & Brown 2017b) and Trojans (e.g., Roig et al. 2008; Wong et al. 2014). This result demonstrates that Hildas and Trojans are composed of two spectrally distinct sub-populations and signifies a new dimension in the study of these objects. Comparative spectroscopy promises to expand our understanding of the surface composition, the underlying cause(s) of the sub-populations' bimodal features, possible divergent evolutionary signatures between Hildas and Trojans, and ultimately, the origin of these objects in the broader context of theories of solar system formation and evolution.

Emery et al. (2011) analyzed near-infrared spectra of 68 Trojans and uncovered a highly robust bifurcation in spectral slope that corresponds with the previously described bimodality in optical colors. In this paper, we describe the results from an analogous near-infrared spectroscopic survey of Hildas. These observations were undertaken with the objective of compiling a significant body of high-quality Hilda spectra to enable detailed comparison with the earlier results of Emery et al. (2011), as well as continuing the search for spectral features that may help further constrain the surface composition of these poorly-understood objects.

7.2 Observations and data reduction

We carried out five observing runs at the NASA Infrared Telescope Facility (IRTF) throughout 2016. The spectra were obtained with the medium-resolution spectrograph and imager SpeX (Rayner et al. 2003). We used the LoRes prism mode with a 0.8×15 arcsec slit, which produces single-order spectra spanning the wavelength range 0.7–2.5 microns. A total of 25 Hildas were observed, of which 5 were observed on two nights.

Our observing strategy closely mirrored the methods described in Emery et al. (2011). Objects were dithered 7.5 arcsec along the slit between pairs of observations. In order to minimize readout time, while reducing the effect of atmospheric variability (in particular, the OH emission at these wavelengths), single-exposure integration times were set at 120 s for all of our observations. The telescope tracked each object using the automatic guider, which measures the spillover of the object outside of

the slit and corrects the pointing to center the object in the slit at a rate of several times a minute. Solar analog G-dwarfs within 5° of the asteroid were regularly observed — typically every ~30 minutes, or whenever the airmass of the object changed by 0.10–0.15. The effect of differential refraction across the wavelength range was minimized by aligning the slit with the parallactic angle (±20°) for all asteroid and star observations. Flat-field and argon lamp wavelength calibration frames were taken at the beginning or end of each observing run. Details of our Hilda observations are listed in Table 7.1.

The prism data were reduced following standard procedures for near-infrared spectra. We utilized the IDL-based spectral reduction program Spextool (Cushing et al. 2004) in our data reduction. For each pair of dithered frames, this program handles flat-field removal, wavelength calibration, non-linearity correction, background subtraction, and spectral extraction through a graphical user interface. To correct for telluric absorptions as well as the solar spectrum, each extracted asteroid spectrum was divided by the corresponding calibration star spectrum that was obtained closest in time and airmass. The effects of instrument flexure on the wavelength calibration and telluric correction were addressed by shifting each asteroid spectrum relative to the corresponding calibration star spectrum to minimize the variability within the water absorption regions. Bad pixels and other significant outliers were manually pruned from the extracted spectra in Spextool before the individual dithered-pair spectra for each object were combined into a single reflectance spectrum.

7.3 Results and discussion

The normalized reflectance spectra of the 25 Hildas targeted in our observing runs are shown in the Appendix. Here, and in the subsequent analysis, we have included additional spectra of three Hildas (153 Hilda, 190 Ismene, and 361 Bononia) obtained using IRTF/SpeX and published in Takir & Emery (2012). The signal-to-noise ratio (S/N) of the 28 Hilda spectra in K-band (2.22 μm) range from 20 to 300.

As is the case with the 0.7–2.5 micron Trojan spectra published in Emery et al. (2011), none of the Hilda spectra show any absorption features to within the noise level in the data. Therefore, while the surface composition of Hildas is typically assumed to be similar to that of Trojans, i.e., rich in water ice, organics, and crystalline silicates (Emery & Brown 2003; Yang & Jewitt 2007), no evidence for these materials are found in the near-infrared spectra.

Table 7.1: Observation Details

Number	Name	Date (UT)	Start Time (UT)	$t_{\rm int}$ (min)	V[a]	H_v	Diam[b] (km)	Standard Star	Spectral Type	$V-J$	$J-K$
499	Venusia	2016 Mar 12	14:40	20	16.4	9.39	88	HD 133011	G2V	1.16	0.33
748	Simeisa	2016 Mar 12	15:11	20	16.0	9.01	105	HD 140990	G2V	1.13	0.34
1162	Larissa	2016 Apr 2	06:23	20	16.2	9.44	86	HD 60298	G2V	1.23	0.34
1180	Rita	2016 Apr 2	05:35	32	16.5	9.14	99	HD 259516	G2V	1.13	0.34
1256	Normannia	2016 Aug 5	07:41	8	15.4	9.66	78	HD 172404	G2V	1.09	0.32
1268	Libya	2016 Mar 12	12:54	12	15.4	9.12	100	HD 129829	G2V	1.03	0.32
1269	Rollandia	2016 Aug 5	14:40	24	15.6	8.82	114	HD 10861	G2V	1.09	0.34
1512	Oulu	2016 Apr 2	06:52	20	16.2	9.62	79	HD 77730	G2V	1.18	0.39
1578	Kirkwood	2016 Mar 15	13:49	92	17.2	10.26	59	HD 136983	G1V	1.14	0.34
1746	Brouwer (1)	2016 Mar 12	15:53	12	17.0	9.95	68	HD 132412	G2V	1.09	0.31
1746	Brouwer (2)	2016 Mar 15	12:20	60	16.9	9.95	68	HD 132412	G2V	1.09	0.31
1754	Cunningham	2016 Aug 5	09:42	8	14.7	9.77	74	HD 197089	G2V	1.07	0.35
1902	Shaposhnikov	2016 Apr 16	05:17	60	16.9	9.51	83	HD 259516	G2V	1.13	0.34
1911	Schubart (1)	2016 Mar 12	12:28	16	16.0	10.11	63	HD 116367	G3V	1.15	0.38
1911	Schubart (2)	2016 Mar 15	11:58	12	15.9	10.11	63	HD 116367	G3V	1.15	0.38
2067	Aksnes	2016 Apr 5	12:17	64	17.1	10.48	53	HD 139485	G5V	1.32	0.46
2312	Duboshin	2016 Mar 12	13:15	60	17.0	10.18	61	HD 124071	G1V	1.09	0.34
2624	Samitchell	2016 Aug 5	08:47	20	16.0	10.8	46	HD 177518	G2V	1.29	0.34
2760	Kacha (1)	2016 Mar 12	12:05	12	15.6	10.04	65	HD 114962	G1V	1.14	0.29
2760	Kacha (2)	2016 Mar 15	11:43	8	15.6	10.04	65	HD 114962	G1V	1.14	0.29
3561	Devine	2016 Aug 5	09:57	28	16.0	11.1	40	HD 196164	G2V	1.10	0.31
3577	Putilin	2016 Aug 5	13:02	76	16.7	10.4	55	HD 224251	G2V	1.20	0.38
4446	Carolyn	2016 Aug 5	09:22	12	15.2	11.2	38	HD 197089	G2V	1.07	0.35
5603	Rausudake (1)	2016 Mar 12	11:29	16	16.0	10.7	48	HD 98503	G5V	1.16	0.37
5603	Rausudake (2)	2016 Mar 15	11:13	20	16.0	10.7	48	HD 98503	G5V	1.16	0.37
5661	Hildebrand	2016 Aug 5	12:36	16	15.2	11.1	40	HD 203311	G2V	1.12	0.36
9121	Stefanovalentini	2016 Aug 5	10:54	72	16.4	10.7	48	HD 196164	G2V	1.10	0.31
11388	1998 VU4	2016 Apr 16	07:19	88	17.2	11.2	38	HD 78536	G3V	1.12	0.41
14669	Beletic (1)	2016 Apr 5	11:28	36	17.4	11.5	33	HD 120204	G2V	1.08	0.31
14669	Beletic (2)	2016 Apr 16	09:24	20	17.2	11.5	33	HD 117860	G2V	1.13	0.36

Notes.
[a]Visible apparent magnitudes at the time of observation.
[b]Diameters are calculated from the listed absolute magnitudes (H_v) assuming $p_v = 0.04$ (Ryan & Woodward 2011).

Classification into sub-populations

Several previous studies have revealed that Hildas are bimodal with respect to visible color and infrared reflectivity. Using these results, we can classify objects into sub-populations and examine their average near-infrared spectra separately.

Analysis of photometry for Hildas contained in the Sloan Digital Sky Survey Moving Object Catalog (SDSS-MOC) demonstrates that the distribution of spectral slopes at visible wavelengths is strongly bimodal, indicative of two sub-populations with visible colors centered at 4.0 and 9.3, in units of %/1000 Å (Gil-Hutton & Brunini 2008; Wong & Brown 2017b). Following previous works, we refer to these two sub-populations as less-red (LR) and red (R). Ten of the 28 Hildas in our sample have SDSS-MOC photometry; an additional eight objects have earlier published visible spectral slopes (Dahlgren & Lagerkvist 1995; Dahlgren et al. 1997). We note that there is significant overlap between the two modes in the visible color distribution, so some objects with intermediate spectral slopes cannot be definitively categorized as LR or R. The sub-population classifications based on visible colors are listed in Table 7.2. We classify 8 objects as LR, 6 objects as R, and 4 objects as intermediate.

The reflectivity of Hildas in the W1 (3.4 μm) and W2 (4.6 μm) bands of the Wide-field Infrared Survey Explorer (WISE) space telescope also allows for classification of Hildas into the LR and R sub-populations. Specifically, the distribution of relative infrared reflectance in the W1/W2 bands with respect to visible albedo shows two clearly separated clusters (see Figure 12 in Grav et al. 2012), with one group systematically more reflective at infrared wavelengths than the other. Selecting for Hildas with reflectance measurements in both W1 and W2 bands, we are able to categorize 18 objects (9 LR and 9 R). The sub-population classifications based on infrared reflectivity are listed in Table 7.2.

Comparing the classifications for objects with both visible spectral slope and infrared reflectivity data, we see that the classifications from these two independent methods are consistent, i.e., objects categorized as LR via visible spectral slope are also categorized as LR based on infrared reflectivity, and likewise for R objects. This same pattern was observed for Trojans (Wong et al. 2014) and indicates that LR and R objects differ systematically and predictably in both the visible and the infrared. Combining the two sets of classifications, we are able to categorize 22 out of 28 Hildas in our near-infrared spectral sample: 11 LR and 11 R. We can classify an additional 4 objects (3 R and 1 LR) in our spectral sample, which do not

Table 7.2: Near-infrared Color Indices and Sub-population Classifications

Number	Name	$0.85 - J$	$0.85 - H$	$0.85 - K$	$J - H$	$J - K$	$H - K$	Vis[a] Class.	IR[a] Class.
153[b]	Hilda	0.107 ± 0.007	0.202 ± 0.008	0.314 ± 0.008	0.096 ± 0.009	0.208 ± 0.009	0.112 ± 0.010	LR	LR
190[b]	Ismene	0.098 ± 0.006	0.173 ± 0.008	0.282 ± 0.009	0.075 ± 0.008	0.184 ± 0.010	0.109 ± 0.011	LR	LR
361[b]	Bononia	0.199 ± 0.013	0.330 ± 0.013	0.476 ± 0.013	0.130 ± 0.012	0.276 ± 0.012	0.146 ± 0.012	LR	LR
499	Venusia	0.077 ± 0.009	0.170 ± 0.011	0.280 ± 0.012	0.093 ± 0.012	0.203 ± 0.013	0.111 ± 0.014	LR	LR
748	Simeisa	0.167 ± 0.012	0.292 ± 0.012	0.410 ± 0.012	0.125 ± 0.013	0.242 ± 0.013	0.117 ± 0.013	I	LR
1162	Larissa	0.175 ± 0.010	0.300 ± 0.007	0.413 ± 0.011	0.126 ± 0.011	0.238 ± 0.014	0.112 ± 0.012	–	R
1180	Rita	0.157 ± 0.012	0.270 ± 0.011	0.380 ± 0.012	0.113 ± 0.013	0.224 ± 0.013	0.111 ± 0.012	LR	LR
1256	Normannia	0.276 ± 0.019	0.459 ± 0.016	0.585 ± 0.016	0.183 ± 0.018	0.309 ± 0.018	0.126 ± 0.015	R	R
1268	Libya	0.179 ± 0.013	0.329 ± 0.015	0.467 ± 0.012	0.150 ± 0.015	0.289 ± 0.012	0.138 ± 0.014	I	LR
1269	Rollandia	0.272 ± 0.018	0.427 ± 0.017	0.551 ± 0.016	0.154 ± 0.016	0.279 ± 0.014	0.124 ± 0.012	R	R
1512	Oulu	0.214 ± 0.015	0.326 ± 0.015	0.455 ± 0.015	0.112 ± 0.014	0.241 ± 0.014	0.130 ± 0.013	I	R
1578	Kirkwood	0.236 ± 0.017	0.371 ± 0.014	0.484 ± 0.015	0.134 ± 0.015	0.248 ± 0.016	0.113 ± 0.013	R	R
1746	Brouwer	0.270 ± 0.019	0.460 ± 0.017	0.576 ± 0.017	0.190 ± 0.017	0.306 ± 0.016	0.116 ± 0.013	–	R
1754	Cunningham	0.134 ± 0.011	0.235 ± 0.010	0.333 ± 0.010	0.101 ± 0.011	0.199 ± 0.010	0.098 ± 0.010	LR	–
1902	Shaposhnikov	0.121 ± 0.010	0.232 ± 0.013	0.362 ± 0.015	0.110 ± 0.014	0.241 ± 0.016	0.130 ± 0.018	–	LR
1911	Schubart	0.059 ± 0.006	0.128 ± 0.008	0.224 ± 0.009	0.069 ± 0.008	0.164 ± 0.009	0.095 ± 0.010	LR	LR
2067	Aksnes	0.066 ± 0.005	0.123 ± 0.006	0.235 ± 0.014	0.057 ± 0.006	0.169 ± 0.014	0.113 ± 0.014	–	–
2312	Duboshin	0.312 ± 0.022	0.484 ± 0.020	0.617 ± 0.019	0.172 ± 0.019	0.306 ± 0.018	0.133 ± 0.016	–	R
2624	Samitchell	0.194 ± 0.013	0.292 ± 0.015	0.377 ± 0.012	0.098 ± 0.014	0.183 ± 0.011	0.085 ± 0.013	R	–
2760	Kacha	0.211 ± 0.014	0.386 ± 0.014	0.522 ± 0.012	0.175 ± 0.016	0.311 ± 0.013	0.136 ± 0.014	–	–
3561	Devine	0.280 ± 0.019	0.453 ± 0.017	0.580 ± 0.017	0.174 ± 0.016	0.300 ± 0.016	0.127 ± 0.014	I	–
3577	Putilin	0.250 ± 0.019	0.382 ± 0.016	0.515 ± 0.017	0.133 ± 0.015	0.265 ± 0.016	0.132 ± 0.013	R	R
4446	Carolyn	0.279 ± 0.019	0.431 ± 0.017	0.538 ± 0.017	0.153 ± 0.014	0.259 ± 0.014	0.106 ± 0.011	R	–
5603	Rausudake	0.251 ± 0.016	0.431 ± 0.014	0.592 ± 0.014	0.180 ± 0.016	0.341 ± 0.016	0.161 ± 0.014	–	R
5661	Hildebrand	0.248 ± 0.016	0.410 ± 0.017	0.523 ± 0.018	0.161 ± 0.014	0.275 ± 0.015	0.113 ± 0.016	–	–
9121	Stefanovalentini	0.183 ± 0.013	0.313 ± 0.011	0.401 ± 0.014	0.129 ± 0.013	0.218 ± 0.015	0.088 ± 0.014	–	–
11388	1998 VU4	0.013 ± 0.010	0.047 ± 0.013	0.101 ± 0.018	0.034 ± 0.014	0.088 ± 0.019	0.054 ± 0.021	LR	–
14669	Beletic	0.269 ± 0.014	0.402 ± 0.012	0.533 ± 0.015	0.133 ± 0.014	0.264 ± 0.017	0.131 ± 0.015	–	–

Notes.
[a]Classification into less-red (LR) and red (R) sub-populations based on visible spectral slopes (Dahlgren & Lagerkvist 1995; Dahlgren et al. 1997; Gil-Hutton & Brunini 2008; Wong & Brown 2017b) and infrared albedos measured by WISE (Grav et al. 2012). An intermediate (I) classification denotes a published spectral slope measurement that does not allow for categorization of the object as less-red or red.
[b]Derived from spectra published in Takir & Emery (2012).

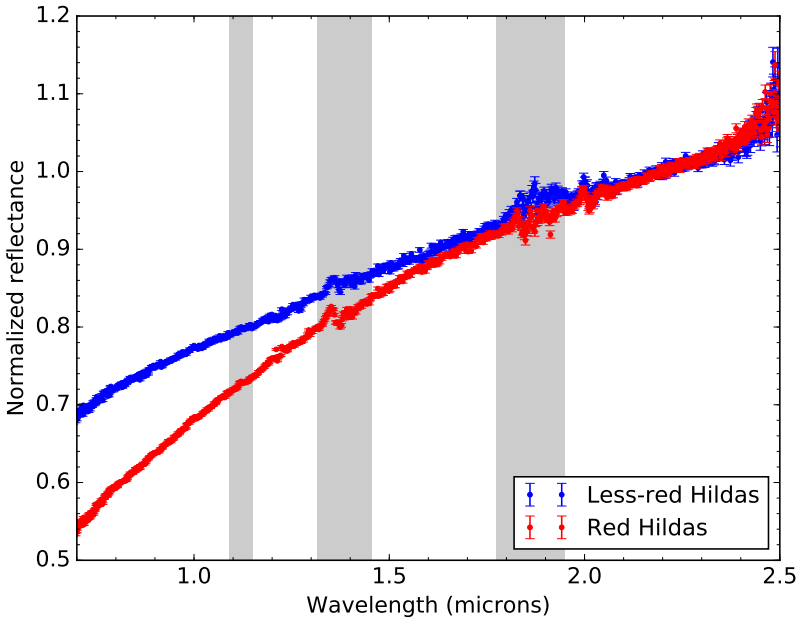

Figure 7.1: Average of spectra in the LR and R Hilda sub-populations, normalized to unity at 2.2 μm. The two spectra are averages of 12 and 14 individual object spectra, respectively. Gray bars mark regions of strong telluric water vapor absorption. The two sub-populations are distinguished primarily by the difference in spectral slope at shorter near-infrared wavelengths ($\lambda < 1.5$). The error bars shown here and in subsequent figures are the uncertainties on the individual reflectance values derived from the weighted average of individual object spectra.

have independent published optical or infrared observations, based on their relative positions in near-infrared color space. This brings the total classification count to 12 LR and 14 R.

Figure 7.1 plots the average of all spectra in the two color sub-populations. The main observation is that the average LR and R Hilda spectra are highly distinct, with the difference in shape concentrated primarily at the shorter end of the near-infrared range ($\lambda < 1.5$). While the R Hilda spectrum is concave down throughout most of the near-infrared, the LR Hilda spectrum is mostly straight, with only a slight downturn at the shortest wavelengths. This indicates that the LR and R Hilda sub-populations have distinct surface properties, in agreement with the bimodality previously seen at both visible and infrared wavelengths.

Comparison with Jupiter Trojans

In order to compare the absolute reflectivity spectra of LR and R Hildas and Trojans, we compiled all previously published visible spectra (Bus & Binzel 2002; Lazzaro et al. 2004; Takir & Emery 2012) as well as broadband SDSS-MOC photometry of Hildas within our near-infrared spectral sample.[1] All five Hildas with visible spectra (153 Hilda, 190 Ismene, 361 Bononia, 1180 Rita, and 1754 Cunningham) are LR objects. The visible spectral and photometric data are matched to the near-infrared reflectance spectra at 0.75 and 0.913 (Sloan z-band) μm, respectively. The absolute reflectivity level is set by the average visible (0.55 μm) geometric albedo: 0.04 (Ryan & Woodward 2011).

Figure 7.2 shows the average reflectivity spectra of LR and R Hildas, along with analogous data for Trojans taken from Emery et al. (2011) and Takir & Emery (2012). We note that the Hilda and Trojan visible spectral samples are a subset of the corresponding near-infrared spectral samples; moreover, there is little overlap between the visible spectral and SDSS-MOC photometric samples. Therefore, some mismatch between the visible spectral and photometric data can be expected.

The main observation from the comparison plot is that the corresponding subpopulations in the Hildas and Trojans have notably similar spectra. Looking at the R objects separately, we find that R Hildas and R Trojans display largely identical spectral slopes across the visible and near-infrared wavelengths. This observation is corroborated by the reported average visible spectral slopes: 9.3 %/1000 Å for R Hildas (Wong & Brown 2017b), and 9.6 %/1000 Å for R Trojans (Wong et al. 2014). A slight difference in spectral slope is apparent between 0.7 and 0.9 μm. While this disparity between the two populations may be real, this region corresponds to the lower end of the IRTF/SpeX wavelength range, where the transmission function rises steeply. As such, data in this wavelength region are especially susceptible to residual signals from telluric correction, as, for example, in the case of uncorrected nonlinear effects from instrument flexure (Section 7.2).

The average LR Hilda and Trojan spectra likewise demonstrate similar overall shapes. However, a closer look reveals the possible presence of a very broad and shallow absorption feature in the region 0.5–1.0 μm. We note that the sharp inflection point at 0.7 μm is likely to be primarily caused by the concatenation of different data sets for the visible and near-infrared average spectra, with the former

[1] We do not include the visible spectra from Dahlgren & Lagerkvist (1995) and Dahlgren et al. (1997), as those spectra are not published with uncertainties on the individual data points.

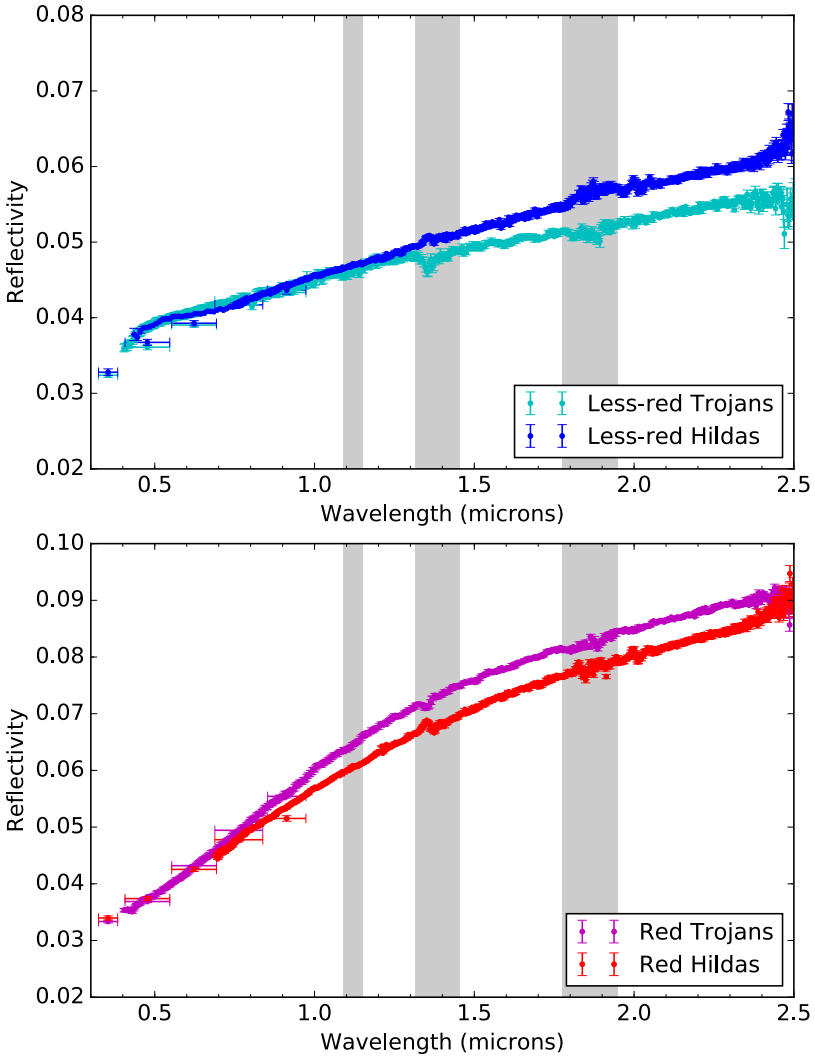

Figure 7.2: Comparison of combined visible and near-infrared average spectra of LR (top) and R (bottom) Hildas and Trojans. The absolute reflectivity level at 0.55 μm for each spectrum is set by the published visible albedos: 0.04 for Hildas (Ryan & Woodward 2011) and 0.041 for Trojans (Fernández et al. 2009). Average $u-g-r-i-z$ broadband reflectances for objects in our spectral sample with SDSS-MOC photometry are overplotted. R Hildas and Trojans have largely identical spectra. On the other hand, LR Hildas are systematically bluer in the visible and redder in the near-infrared than LR Trojans, suggesting the presence of a broad, shallow absorption feature between 0.5 and 1.0 μm.

being a subset of the latter. We note that none of the individual Hilda spectra spanning both visible and near-infrared wavelengths shows a discernible feature in this wavelength region above the level of the uncertainties.

Nevertheless, both visual comparison and color indices (see below) demonstrate that LR Hildas are noticeably redder on average (i.e., have steeper spectral slopes) than LR Trojans throughout much of the near-infrared (0.7–2.0 μm). In contrast, at visible wavelengths, LR Hildas and somewhat bluer than LR Trojans, as evidenced by their average spectral slopes: 4.0 %/1000 Å for LR Hildas (Wong & Brown 2017b), and 5.3 %/1000 Å for LR Trojans (Wong et al. 2014). Together, these disparities imply an overall concave-up shape in the average LR Hilda spectrum relative to the LR Trojan spectrum extending from the visible into the near-infrared. The implications of such an absorption feature are discussed below.

Near-infrared colors

To study the spectra more quantitatively, we calculated near-infrared colors. Following the methods described in Emery et al. (2011), we derived color indices from the normalized reflectance at four wavelengths: 0.85 μm, J (1.25 μm), H (1.65 μm), and K (2.22 μm). The color $m_{\lambda 1} - m_{\lambda 2}$ corresponding to a given reflectance ratio $R_{\lambda 2}/R_{\lambda 1}$ was calculated using the relation $m_{\lambda 1} - m_{\lambda 2} = 2.5 \log(R_{\lambda 2}/R_{\lambda 1})$. Standard error propagation was used to calculate the color uncertainties. The measured colors for all the Hildas in our sample are listed in Table 7.2.

Figure 7.3 shows the distribution of Hilda colors (colored points) in the $J - K$ vs. $0.85 - J$ space, along with the corresponding distribution of Trojan colors (black points), taken from Emery et al. (2011). The colors of the LR and R Hildas are denoted by blue and red. The overall Trojan color distribution is robustly bimodal, with the locations of the LR and R Trojans clearly identifiable. In contrast, while the LR and R Hildas in our near-infrared spectral sample occupy disparate regions in the $J - K$ vs. $0.85 - J$ space, these regions overlap, resulting in an overall Hilda color distribution that lacks the bimodality seen in the Trojan data. Taking the positions of the 6 hitherto unclassified Hildas on the two-color plot into consideration, we are able classify one (2067 Aksnes) as LR and three (3561 Devine, 5661 Hildebrand, and 14669 Beletic) as R, with the remaining two Hildas unclassifiable due to their having near-infrared color indices that lie in the overlap of the LR and R color regions. The final classification count in our spectral sample is 12 LR and 14 R.

Examining the color indices more closely, we see that the R Trojans and R Hildas have comparable near-infrared colors, in line with the observation from our comparison of their average spectra. Meanwhile, the LR Hildas have redder (i.e., higher) color indices than the LR Trojans. The relative shift in the cluster of LR Hildas

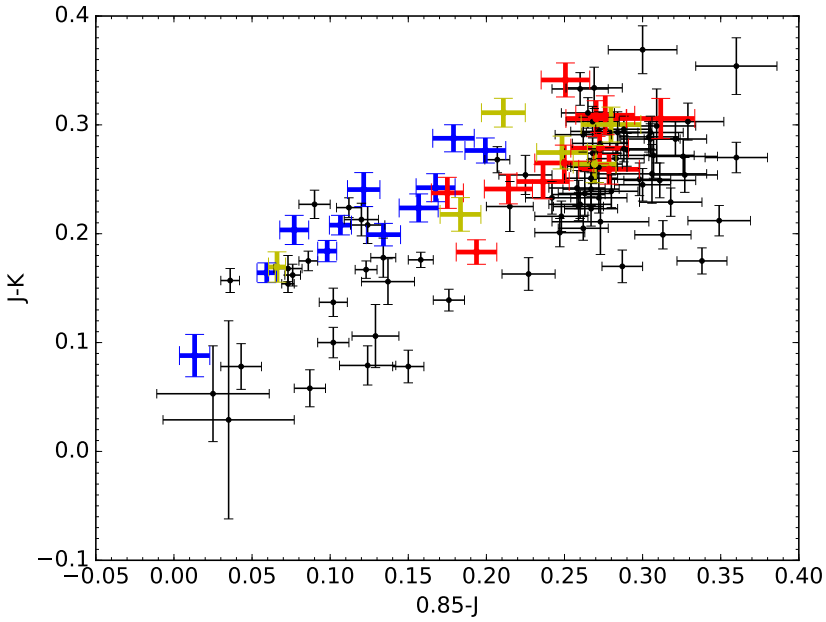

Figure 7.3: Two-color plot derived from the near-infrared spectra of Hildas (colored points) and Trojans (black points). Hildas that are classified as less-red (LR) and red (R) via visible color and/or infrared reflectivity are denoted by blue and red, respectively; unclassifed objects are marked in yellow. The Hilda near-infrared color distribution lacks the robust bimodality evident in the Trojan data. Nevertheless, LR and R Hildas occupy distinct regions in color space, implying systematically different surface properties and allowing us to classify an additional 4 objects into the LR and R sub-populations.

relative to the LR Trojans is particularly noticeable along the $0.85 - J$ axis, in agreement with the visual spectroscopic comparison in Figure 7.2, which shows that the LR Hildas have steeper spectral slopes than LR Trojans in the short wavelength end of IRTF/SpeX wavelength range.

Implications

In the context of general characteristics shared by Hildas and Trojans, e.g., reddish colors, near-identical optical albedos, and bimodalities in visible color and infrared reflectivity, the large-scale similarity in near-infrared spectra offers further support to the idea of a common origin for these two minor body populations. While the overall near-infrared color distribution of Hildas does not display bimodality, as in the case of Trojans, Hildas classified as LR or R via visible color and/or infrared reflectivity cluster around two separate near-infrared color centers.

The systematic spectral differences between LR and R objects within the Hilda and Trojan populations, which are manifested from the visible to the infrared, are indicative of distinct surface compositions (see also discussion in Emery et al. 2011). Wong & Brown (2016) developed a hypothesis within the framework of current dynamical instability models to explain the origin of the sub-populations attested in the Hildas, Trojans, and similarly-sized Kuiper Belt objects (Wong & Brown 2017a). In short, the precursor objects to these three populations initially formed in a planetesimal disk spanning a wide range of heliocentric distances in the outer Solar System beyond the orbits of the ice giants with roughly cometary compositions rich in volatile ices such as ammonia, methanol, hydrogen sulfide, etc. Subsequent insolation-driven sublimation loss led to the development of distinct surface compositions over the course of the first few hundred million years after the end of planet formation, prior to the onset of dynamical stability that scattered these bodies into their present-day locations.

From our modeling, we predict hydrogen sulfide ice (H_2S) to be the crucial volatile ice species responsible for the development of two distinct spectral types. Objects in this outer solar system primordial disk would have been split into two groups: the objects situated closer to the Sun experienced higher surface temperatures and became depleted of H_2S on their surfaces, while objects farther out retained H_2S. Previous experimental work has shown that irradiation of volatile ices leads to a general reddening of the optical color (e.g., Brunetto et al. 2006). We posit that the presence of H_2S, which is known to induce a strong reddening of the surface upon irradiation (see, for example, H_2S frost on Io; Carlson et al. 2007), would contribute additional reddening relative to the case where H_2S was absent. In both cases, the result of irradiation would have been the formation of a refractory mantle on the surface of the objects, with the presence or absence of sulfur-bearing minerals yielding a color bimodality among objects in the primordial planetesimal disk. Objects that retained H_2S on their surfaces would develop R colors, while those that became depleted in H_2S would develop LR colors. The subsequent dynamical instability spread these objects across the present-day minor body populations, which therefore inherit this primordial color bimodality.

Our present analysis has shown that LR Hildas have relatively steeper spectral slopes in the near-infrared when compared to LR Trojans; meanwhile, R Hildas and Trojans have near-identical visible and near-infrared colors. In the context of the aforementioned color bimodality hypothesis, which posits that both LR and

R Hildas and Trojans were scattered into their present-day orbits from the same progenitor population in the outer Solar System, this disparity between LR Hildas and Trojans is likely explained by their different present-day environments. Hildas orbit significantly closer to the Sun than Trojans and thereby experience higher surface temperatures. It follows that the surface chemistries (sulfur-bearing or sulfur-less) of LR and R objects react differently to heating. While R objects appear to be stable to the temperature change between the Trojan and Hilda regions, LR objects develop redder spectral slopes in the near-infrared and bluer optical colors when heated.

The putative broad and shallow absorption feature in the average LR Hilda spectrum between 0.5 and 1.0 μm is notable in that it suggests the first spectroscopic signature to be found at visible or near-infrared wavelengths on Hildas. Future study of more precise spectra of Hildas with continuous wavelength coverage across the visible and near-infrared is needed to confirm and/or characterize this feature. Nevertheless, comparing the Hildas with other nearby minor body populations offers a clue to its possible origin.

Looking inward, we find some clearer examples of this feature. Combined visible and near-infrared spectra of two Cybele group asteroids — 76 Freia and 107 Camilla — show a pronounced concave-up shape throughout the 0.5–1.0 μm region within otherwise featureless spectra (Takir & Emery 2012). These objects lie in the 7:4 mean-motion resonance with Jupiter, with orbital semimajor axes of 3.41 and 3.49 AU, respectively, and, similar to Hildas and Trojans, are presumed to originate in the outer Solar System within the dynamical instability scenario (Roig & Nesvorný 2015). Both of these Cybele asteroids have LR visible colors and, when considered alongside the LR Hildas and Trojans, point to an intriguing trend: the depth of the broad 0.5–1.0 μm feature appears to increase with decreasing heliocentric distance.

This broad absorption feature between 0.5 and 1.0 μm in asteroidal spectra is generally interpreted as indicating hydrated phyllosilicate minerals on the surface (e.g., Rivkin et al. 2015 and references within). The possible presence of hydrated minerals on the surface of Hildas has major implications for their evolutionary history, since it would require melting of surficial water ice, which does not occur at the present-day surface temperatures of Hildas. Within the framework of dynamical instability models, the aforementioned trend between the depth of the 0.7 μm feature and heliocentric distance among LR objects could be explained if the Cybeles and

Hildas were scattered onto orbits that passed systematically closer to the Sun than Trojans during the period of dynamical instability, thereby experiencing higher surface temperatures and possible melting of water ice. The additional observation that R Hildas do not display this absorption signature may indicate that the presence of sulfur-bearing components on the surface blocks the development of hydrated mineral absorption features. Further spectral modeling and dynamical instability orbital simulations are needed to determine the specific chemical species responsible for the absorption feature and how it figures into the origin and evolution of these minor body populations.

7.4 Conclusion

In this paper, we presented new near-infrared spectra of 25 Hilda asteroids. As in the case of analogous spectra of Trojans (Emery et al. 2011), we did not detect any absorption features within the wavelength range covered by the IRTF/SpeX spectrograph (0.7 – 2.5 μm). Classifying the Hildas into less-red and red sub-populations based on their previously published visible color and/or infrared albedo, we found that the average less-red and red Hilda spectra have very distinct shapes. Taken together, the systematic differences in spectroscopic/photometric properties from the visible through the infrared firmly establish that the two Hilda sub-populations possess distinct intrinsic surface compositions, in agreement with the conclusions of earlier studies of Trojans.

Combining our near-infrared spectra with visible spectra from the literature and comparing the results with analogous data for Trojans, we observed that the corresponding sub-populations within the Trojans and Hildas have similar overall spectral shapes. This lends support to the idea that the less-red and red Trojans and Hildas are each sourced from a single progenitor population, as is posited by recent dynamical instability theories of solar system evolution. Upon closer inspection, we uncovered a notable difference between the less-red and red objects in the Hilda and Trojan populations. Whereas the red Hildas and Trojans have nearly identical spectra, the less-red Hildas are significantly redder than less-red Trojans in the near-infrared, while being somewhat bluer than their Trojan counterparts at visible wavelengths. From this observation, we inferred the presence of a very broad and shallow absorption feature in the average less-red Hilda spectrum between 0.5 and 1.0 μm, suggesting the possible presence of hydrated minerals on the surface. In the context of our hypothesis regarding the origin of the two sub-populations, we proposed that the discrepancy between less-red Hilda and Trojan spectra is a consequence of their

different surface temperatures. Meanwhile, objects in the red spectral type are stable to the temperature gradient between the Hilda and Trojan regions.

Pinning down a more detailed picture of the surface (and bulk) composition of Hildas and Trojans remains a crucial and unfulfilled step in the overarching objective of understanding the origin of these minor body populations and validating current models of solar system evolution. A potentially fruitful avenue of further study is analyzing new Hilda spectra covering the 3 μm region. Previous study of Trojans has revealed a significant absorption feature centered at around 3.1 μm, consistent with both water frost and ammonia ice (Brown et al. 2011). Intriguingly, the depth of this feature is strongly correlated with spectral type, with less-red Trojans having systematically deeper absorption than red Trojans. This absorption signal has already been detected in the three extant Hilda spectra covering this wavelength range (Takir & Emery 2012); however, the three objects all belong to the less-red sub-population. Additional spectroscopic observations targeting both less-red and red Hildas will provide a more detailed look into this feature in relation to the two sub-populations and will aid in the continued exploration of environmental effects on the surface properties of these primordial bodies.

Appendix

Plotted here are the final reduced near-infrared spectra of Hildas presented in this paper. Of these, 25 are derived from the IRTF/SpeX observations described in Section 7.2, and three (153 Hilda, 190 Ismene, and 361 Bononia) are previously published in Takir & Emery (2012). All spectra are normalized to unity at 2.2 μm and shifted in intervals of 0.5 for clarity. The gray bars denote the main wavelength regions of telluric water vapor absorption. Residual signals within these bands are caused by variable atmospheric conditions during and/or between observations of asteroids and solar analogs stars used for telluric correction.

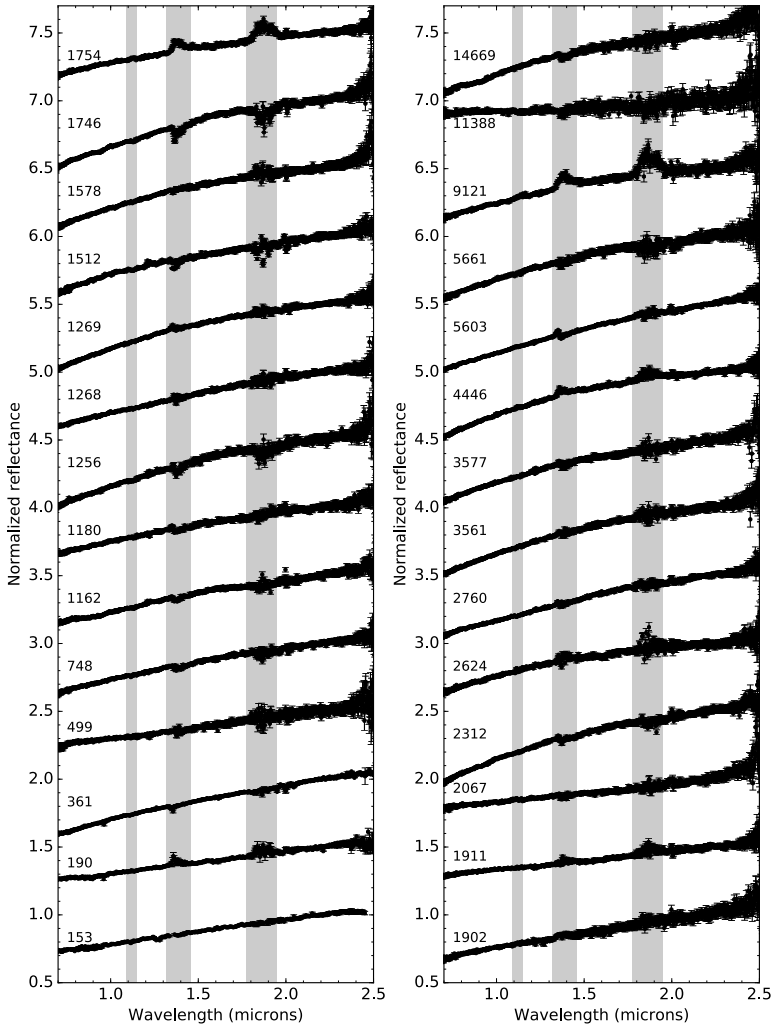

References

Brown, M. E., Schaller, E. L., & Fraser, W. C. (2011). "A hypothesis for the color diversity of the Kuiper belt". *ApJ*, 739, L60.

Brunetto, R., Barucci, M. A., Dotto, E., & Strazzulla, G. (2006). "Ion irradiation of frozen methanol, methane, and benzene: Linking to the colors of Centaurs and trans-Neptunian objects". *ApJ*, 644, 646.

Bus, S. J. & Binzel, R. P. (2002). "Phase II of the Small Main-Belt Asteroid Spectroscopic Survey: The observations". *Icarus*, 158, 106.

Carlson, R. W., Kargel, J. S., Douté, S., Soderblom, L. A., & Brad Dalton, J. (2007). "Io's Surface Composition". In: *Io After Galileo*. Eds. Lopes, R. M. C. & Spencer, J. R. (Chichester, UK: Praxis Publishing Ltd), 194.

Cushing, M. C., Vacca, W. D., & Rayner, J. T. (2004). "Spextool: A spectral extraction package for SpeX, a 0.8 − 5.5 micron cross-dispersed spectrograph". *PASP*, 116, 362.

Dahlgren, M. & Lagerkvist, C.-I. (1995). "A study of Hilda asteroids. I. CCD spectroscopy of Hilda asteroids". *A&A*, 302, 907.

Dahlgren, M., Lagerkvist, C.-I., Fitzsimmons, A., Williams, I. P., & Gordon, M. (1997). "A study of Hilda asteroids. II. Compositional implications from optical spectroscopy". *A&A*, 323, 606.

Emery, J. P. & Brown, R. H. (2003). "Constraints on the surface composition of Trojan asteroids from near-infrared (0.8 − 4.0 micron) spectroscopy". *Icarus*, 164, 104.

Emery, J. P., Burr, D. M., & Cruikshank, D. P. (2011). "Near-infrared spectroscopy of Trojan asteroids: Evidence for two compositional groups". *AJ*, 141, 25.

Fernández, Y. R., Jewitt, D., & Ziffer, J. E. (2009). "Albedos of small Jovian Trojans". *AJ*, 138, 240.

Franklin, F. A., Lewis, N. K., Soper, P. R., & Holman, M. J. (2004). "Hilda asteroids as possible probes of Jovian migration". *AJ*, 128, 1391.

Gil-Hutton, R. & Brunini, A. (2008). "Surface composition of Hilda asteroids from the analysis of the Sloan Digital Sky Survey colors". *Icarus*, 193, 567.

Gomes, R., Levison, H. F., Tsiganis, K., & Morbidelli, A. (2006). "Origin of the cataclysmic Late Heavy Bombardment period of the terrestrial planets". *A&A*, 455, 725.

Grav, T., Mainzer, A. K., Bauer, J. M., Masiero, J. R., & Nugent, C. R. (2012). "WISE/NEOWISE observations of the Jovian Trojan population: Taxonomy". *ApJ*, 759, 49.

Lazzaro, D., Angeli, C. A., Carvano, J. M., & Mothé-Diniz, T. (2004). "S^3OS^2: the visible spectroscopic survey of 820 asteroids". *Icarus*, 172, 179.

Morbidelli, A., Levison, H. F., Tsiganis, K., & Gomes, R. (2005). "Chaotic capture of Jupiter's Trojan asteroids in the early Solar System". *Nature*, 435, 462.

Rayner, J. T., Toomey, D. W., Onaka, P. M., & Denault, A. J. (2003). "SpeX: A medium-resolution 0.8 – 5.5 micron spectrograph and imager for the NASA Infrared Telescope Facility". *PASP*, 115, 362.

Rivkin, A. S., Campins, H., Emery, J. P., & Howell, E. S. (2015). "Astronomical Observations of Volatiles on Asteroids". In: *Asteroids IV*. Eds. Michel, P., DeMeo, F. E., & Bottke, W. F. (Tucson, AZ: University of Arizona Press), 65.

Roig, F. & Nesvorný, D. (2015). "The evolution of asteroids in the jumping-Jupiter migration model". *AJ*, 150, 186.

Roig, F., Ribeiro, A. O., & Gil-Hutton, R. (2008). "Taxonomy of asteroid families among the Jupiter Trojans: comparison between spectroscopic data and the Sloan Digital Sky Survey colors". *A&A*, 483, 911.

Ryan, E. L. & Woodward, C. E. (2011). "Albedos of small Hilda group asteroids as revealed by Spitzer". *AJ*, 141, 186.

Takir, D. & Emery, J. P. (2012). "Outer Main Belt asteroids: Identification and distribution of four 3-μm spectral groups". *Icarus*, 219, 641.

Vilas, F., Jarvis, K. S., & Gaffey, M. J. (1994). "Iron alteration minerals in the visible and near-infrared spectra of low-albedo asteroids". *Icarus*, 109, 274.

Wong, I. & Brown, M. E. (2016). "A hypothesis for the color bimodality of Jupiter Trojans". *AJ*, 152, 90.

Wong, I. & Brown, M. E. (2017a). "The bimodal color distribution of small Kuiper Belt objects". *AJ*, 153, 145.

Wong, I. & Brown, M. E. (2017b). "The color-magnitude distribution of Hilda asteroids: Comparison with Jupiter Trojans". *AJ*, 153, 69.

Wong, I., Brown, M. E., & Emery, J. P. (2014). "The differing magnitude distributions of the two Jupiter Trojan color populations". *AJ*, 148, 112.

Yang, B. & Jewitt, D. (2007). "Spectroscopic search for water ice on Jovian Trojan asteroids". *AJ*, 134, 223.

Chapter 8

CONCLUDING REMARKS AND FUTURE WORK

The previous six chapters encapsulate the contributions of my work to the study of middle and outer solar system minor bodies. The results of this research have greatly expanded and refined our understanding of Trojans, Hildas, and KBOs and have empirically tied the observed properties of these populations to fundamental aspects of solar system formation and evolution.

Some of the highlights from my research include: (1) the first dedicated analysis of the size distributions of the LR and R sub-populations attested in the Trojan and Hilda populations; (2) the unimodal LR color distribution of Trojan and Hilda collisional fragments and the related trend of increasing LR number fraction with decreasing size, suggesting that the color bimodality is a surficial characteristic not reflective of an otherwise uniform bulk composition; (3) the extension of the well-characterized color-size distribution of small Trojans down to kilometer-sized objects, which revealed that the collisionally equilibrated population is composed almost exclusively of LR objects; (4) the first incontrovertible detection of a color bimodality among small KBOs similar in size to Trojans and Hildas, which resolved the origin of the R and VR Centaurs; (5) the first physically- and chemically-motivated compositional hypothesis for the origin of the color bimodality across all middle and outer solar system asteroid populations, rooted in sublimation-driven differential depletion of surficial H_2S ice on the progenitor objects within the pre-instability trans-Neptunian planetesimal disk.

8.1 Evaluating the Trojan-Hilda-KBO connection

Leveraging all of the aforementioned results, we are now in a position to address the properties of Trojans, Hildas, and KBOs as a whole in relation to the predictions of dynamical instability models of solar system evolution. A common origin for all three minor body populations in a dense trans-Neptunian repository of primordial planetesimals implies that all the objects should share similar bulk compositions reflective of the solid material in the protoplanetary disk at those heliocentric distances (~15–30 AU). This similarity must be reflected in the measured colors and spectra of these objects. A shared formation environment should also yield identical initial size distributions, since the original shape of the distribution is determined

solely by the accretion process.

Turning to the results outlined in this thesis, we can see that the Trojans, Hildas, and KBOs display notable population-wide similarities with one another. Firstly, all three populations are bimodal in visible color across the same size ranges. Secondly, the total size distribution of small (non cold classical) KBOs is statistically indistinguishable from the analogous size distributions of Trojans and Hildas of the same size. Since objects in this size range (larger than roughly 30–50 km in diameter) have not experienced any significant collisional alteration, the size distributions here reflect the initial size distributions, lending strong support to the idea of a single formation environment for all three populations. Furthermore, the individual size distributions of the constituent color sub-populations at large sizes are all mutually consistent, indicating that objects in both color classes formed in a similar accretion environment. Meanwhile, the difference in size distribution slope between intermediate-size Trojans and Hildas is straightforwardly attributable to the narrower stability region of Hildas, which leads to gradual preferential depletion of small Hildas.

The realization that all collisional family members in the Trojan and Hilda populations are LR serves as another point of similarity. This behavior is a natural consequence of the color bimodality hypothesis we proposed in Wong & Brown (2016) (Chapter 4), which explains that the difference in color evident in each population can arise from the purely surficial processes of ice sublimation and irradiation, while the overall composition of the objects in both sub-populations is the same; upon shattering at their current heliocentric distances, the volatile ice species responsible for the R and VR colors do not survive, and as a result, the collisional fragments always attain LR colors, regardless of the color of the parent bodies. Likewise, the trend of increasing LR-to-R number ratio with decreasing size, another shared property of Trojans and Hildas, is a corollary of the collisional production of exclusively LR fragments. Lastly, the near-infrared spectra of Trojans and Hildas are similar, with objects belonging to different visible color classes having distinct near-infrared color indices.

All of these similarities, together with the unified hypothesis for the color bimodalities attested in all three populations, offer the first robust, systematic corroboration of the purported connection between Trojans, Hildas, and KBOs within the framework of dynamical instability models. The agreement of the observed properties with the predictions underscores the explanatory power of recent solar system evolution

models, which were initially conceived to explain largely unrelated phenomena regarding to the orbital architecture of the outer planets. My research has therefore yielded preliminary empirical validation of late-stage planetary migration scenarios – a major step in developing a more complete and realistic conception of solar system history.

Nevertheless, one noteworthy unexplained discrepancy remains. While small KBOs are bimodal in color, their colors are systematically redder than the analogous color sub-populations in the Trojans and Hildas. In our model explaining the origin and evolution of these minor bodies, we propose that the significantly higher temperatures experienced by Trojans and Hildas in their present-day locations relative to the conditions in the primordial trans-Neptunian planetesimal disk could have incurred secondary processing of the irradiated surfaces, causing a neutralization of the surface color. However, no specific chemical or physical basis for this suggestion was given, and as such the divergent colors of the middle and outer solar system minor bodies still require a rigorous explanation.

One possible indication that temperature-dependent secondary processing of the surfaces occurred was discussed in Wong et al. (2017) (Chapter 7). A detailed comparison of the combined visible and near-infrared spectra points toward a small, but discernible systematic difference between the average shape of LR Hilda and LR Trojan spectra in the 0.7 μm region. Namely, LR Hildas have flatter visible spectral slopes and steeper near-infrared spectral slopes than their Trojan counterparts. Given the otherwise identical properties of Trojans and Hildas, this difference may indicate the effect of the warmer surface temperatures of Hildas. Further compositional modeling and high signal-to-noise spectroscopy of Hildas and Trojans are needed to definitively explore this region of wavelength space and perhaps constrain the cause of the starker discrepancy in color between Hildas, Trojans, and the distant KBOs.

8.2 Experimental study of Trojan surface analogs

A more general and fundamental deficiency in our understanding of these minor bodies has been the marked lack of robust absorption features retrieved from spectroscopic observations of Trojans, Hildas, and similarly-sized KBOs. This has prevented us from deducing a detailed compositional outline of these objects from observation. In response to this issue, I recently collaborated with a group of laboratory specialists at Jet Propulsion Lab to carry out ice irradiation experiments simulating the compositions and conditions in the early outer Solar System as de-

scribed in the color bimodality hypothesis. Having a concrete compositional model for these primitive asteroids has allowed us to produce laboratory spectra of the exact purported chemical makeup of their surfaces as a definitive point of comparison for future observations.

The team created ice samples containing water ice, methanol ice, and ammonia ice, either with or without the additional inclusion of H_2S ice (called the no sulfur and with sulfur samples, respectively). These ice mixtures correspond to the predicted volatile ice compositions of the primordial outer solar system planetesimals after the location-dependent differential sublimation loss of H_2S. We then bombarded the samples with electrons and heated them to simulate the irradiation, scattering, and subsequent capture of Trojans from the outer Solar System to their current locations (Mahjoub et al. 2016; Mahjoub et al. 2017; Poston et al. 2018). Several of the important trends characteristic of Trojans are evident in the experimental results, providing strong support to the compositional makeup of Trojans described in Wong & Brown (2016): (1) both the no sulfur and with sulfur samples reddened and darkened upon irradiation, with the sample containing H_2S reddening significantly more than the sample without sulfur; (2) both samples displayed flattening of the spectral slope (i.e., neutralization) and further darkening upon heating, though only after raising the temperature above ~150 K, which may indicate that the grayer colors of the Trojans and Hildas relative to small KBOs arose during the transitional scattering phase prior to capture, when the objects were on high-eccentricity orbits with low perihelia that brought them much closer to the Sun than their current orbits do.

8.3 Further spectroscopic study

Both the no sulfur and with sulfur endpoint spectra from the laboratory experiments are largely featureless between 500 nm and 2.5 μm, in agreement with the lack of observed absorption signatures in analogous published spectra of Trojans. However, a set of deep and distinctive absorption features appear in both spectra throughout the near-ultraviolet and blue optical wavelength range. Figure 8.1 shows the continuum-subtracted no sulfur and with sulfur laboratory spectra from 200 to 550 nm. Several absorption features are evident, with the distinction between the two surface types particularly notable in the 200–300 nm range. The handful of visible Trojan spectra collected so far only extend down to ~400 nm. Nevertheless, at least in the LR Trojan and LR Hilda spectra (Figure 7.2), a slight downturn in the reflectance below 500 nm is discernible, indicating the edge of an absorption feature that continues to

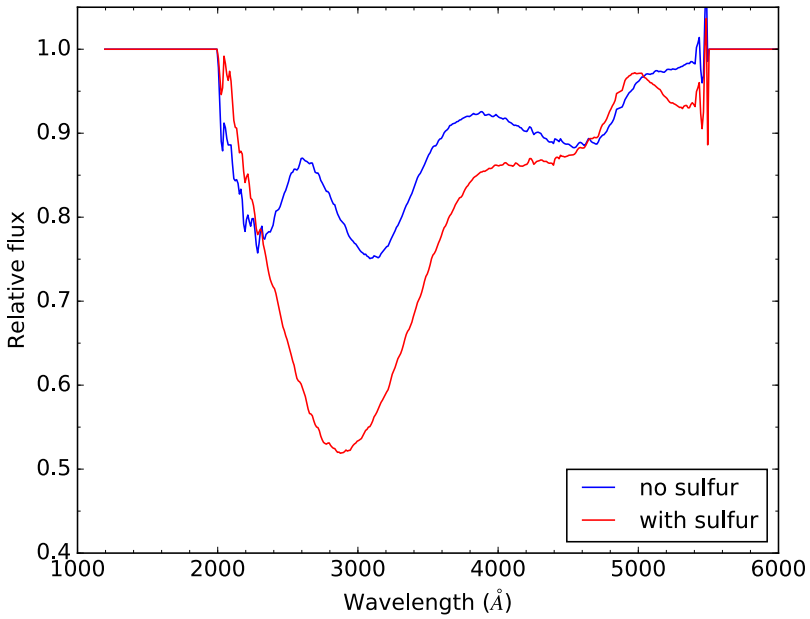

Figure 8.1: Continuum subtracted average laboratory spectra of the experimental ice samples with or without the inclusion of H_2S ice in the near-ultraviolet and blue optical wavelength region. Notably, the no sulfur spectrum shows a relatively narrow absorption feature centered at around 230 nm, which is absent in the spectrum with sulfur.

shorter wavelengths, similar to what we find in the no sulfur laboratory spectrum in Figure 8.1.

None of the middle and outer solar system minor body populations have been studied at UV wavelengths. Later this year, I will obtain the first UV spectra of Trojans using the *Hubble Space Telescope* (accepted Cycle 25 program GO-15249, PI: I. Wong). The targets I plan to observe using the Space Telescope Imaging Spectrograph in low-resolution mode are the three brightest Trojans in each of the two subpopulations (LR: 1437 Diomedes, 3451 Mentor, 659 Nestor; R: 624 Hektor, 911 Agamemnon, 1143 Odysseus). The resulting spectra will provide continuous coverage from 160 nm to 570 nm, spanning the full region in which the predicted absorption features are located.

Detecting spectral features in this wavelength range comparable to the ones we find in the experimental ice mixtures would immediately confirm the color bimodality hypothesis, indicating that Trojans formed on both sides of the H_2S sublimation line. More fundamentally, these results would definitively demonstrate that the Trojans

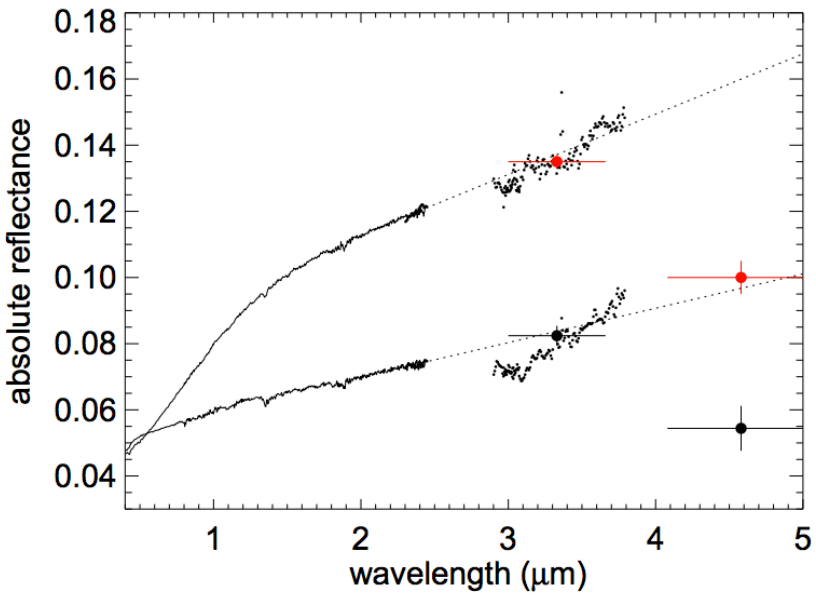

Figure 8.2: Average normalized reflectance spectra of LR and R Trojans (from Brown 2016). The 3.1 μm absorption feature is prominently seen in the LR spectrum. The broadband reflectance data are derived from Wide-field Infrared Survey Explorer data (Grav et al. 2012). Both spectra indicate the presence of a major absorption feature in the 4–5 μm region.

originated in the outer Solar System and offer direct observational validation of the dynamical instability hypothesis. Conversely, a lack of observed features or the presence of features not predicted by the laboratory spectra would necessitate a reconsideration of the chemical and physical processes responsible for the bimodal surface colors of Trojans and related populations.

While optical spectroscopy of Trojans has hitherto not revealed any incontrovertible spectral signatures to confirm the surface compositions predicted by our hypothesis, recent 2.2–3.8 μm near-infrared spectroscopy has uncovered a broad absorption feature at around 3.1 μm (Brown 2016 and Figure 8.2). The shape of the absorption is consistent with either water frost or a N-H vibrational feature. In the latter case, this feature would be indicative of the presence of ammonia ice (or irradiation products thereof) on the surface and would point toward an outer solar system origin for Trojans.

Interestingly, the amplitude of this feature varies systematically with color and is most apparent on LR Trojans. In the context of the hypothesized compositional model of Trojans, this trend would suggest that the presence of sulfur-bearing

molecules on the surface of R Trojans may be blocking certain types of irradiation chemistry and thereby attenuating the 3.1 μm feature. It is also noteworthy that the laboratory spectra of the no sulfur and with sulfur ice mixtures display a similar 3.1 μm feature, with the depth trending in a manner consistent with the Trojan spectra.

Takir & Emery (2012) presented spectra for three LR Hilda asteroids, and all display a feature at 3.1 μm comparable to the feature seen in Trojan spectra. In order to better study this feature, I will obtain analogous high signal-to-noise, medium-resolution near-infrared spectra of the brightest Hildas, specifically targeting objects in both the LR and the R subpopulations. I have previously obtained K- and L-band spectra (2.2–3.8 μm) of five Hildas using the Keck/NIRSPEC near-infrared spectrograph and will propose to observe around a dozen more using the same instrument throughout 2018. These observations will be coupled with broadband visible photometry of all the Hildas in the spectral sample using the new Zwicky Transient Facility at Palomar Observatory, from which optical colors will be derived.

Together, these observations will probe the trend between 3.1 μm absorption depth and color for Hildas in a manner similar to what was done for Trojans in Brown (2016). The smaller heliocentric distance and therefore brighter apparent magnitude of Hildas will enable greater sensitivity in the spectroscopic observations, allowing me to better resolve the detailed shape of the 3.1 μm feature and more definitively model the surface chemistry. Collecting a Hilda spectral dataset analogous to the previously published Trojan K- and L-band spectra may also reveal differences between the two populations, which would add another constraint to the possible secondary evolutionary processes that have affected the surface composition of these objects in the time that has elapsed since their emplacement (see Section 8.1). The characterization of such processes will also provide additional insight on the chemical composition and physical properties of the surface.

8.4 JWST, *Lucy*, and beyond

Future telescopes and space missions will usher in a new age of astronomical observations. The soon-to-be-launched *James Webb Space Telescope* (JWST) will be a boon for planetary science, offering greatly improved sensitivity and broader wavelength coverage over its predecessor *Hubble*.

I will capitalize on the exquisite capabilities of JWST to propose a large Cycle 1 survey of Trojans, Hildas, and similarly-sized KBOs. For each population, targets

from both color sub-populations will be selected. The main objective of this JWST observing campaign will be medium-resolution spectroscopy using NIRSpec spanning the entire wavelength range from 0.6 to 5.3 μm. These spectra will yield a marked improvement in sensitivity over previously obtained or proposed ground-based spectra, allowing for more detailed interpretations of the surface composition. JWST/NIRSpec is also the first instrument capable of effective spectroscopic observations of KBOs smaller than ~200 km in diameter, which will allow me to model the surface of these primitive bodies and directly compare their spectra with those of Trojans and Hildas for the first time. The results from these analyses promise to conclusively resolve the unanswered question of the divergent colors of the KBO sub-populations in relation to the Trojans and Hildas.

Of particular interest in the proposed JWST campaign is the 4–5 μm region. Figure 8.2 shows the average broadband infrared reflectivity of LR and R Trojans at 3.4 and 4.6 μm, derived using data from the Wide-field Infrared Survey Explorer (Grav et al. 2012). The significant dropoff in reflectance across the two bandpasses indicates the presence of a major absorption feature in this wavelength region. This portion of the spectrum is inaccessible from ground-based observations, and JWST/NIRSpec will be the first instrument capable of probing these wavelengths with spectroscopy, opening up a hitherto unexplored region to detailed study. The experimental Trojan analog spectra from our laboratory tests do not contain major absorptions in this region, so a detailed analysis of the 4–5 μm wavelength range will yield major refinements and/or alterations to our current compositional model of Trojans and related asteroid populations.

On 4 January 2017, *Lucy* was announced as the thirteenth NASA's Discovery Program. This space probe will carry out flyby studies of five Jupiter Trojans, 3 LR and 2 LR objects, between 2027 and 2033. The successful selection of this mission underscores the increased prominence of middle and outer solar system minor bodies in the field of planetary science and recognizes the important role Trojans play in unlocking many of the secrets of solar system formation and evolution. The suite of instruments housed on the spacecraft includes a high-resolution visible imager, a thermal infrared spectrometer, and a visible-infrared spectroscopic mapper. The flyby studies will produce extremely detailed maps of the surface regolith at many wavelengths, providing a unique opportunity to explore variations in surface composition across each object. The *Lucy* mission will ultimately offer the definitive ground truth for Trojan studies, with wide-ranging implications for small body

astronomy and solar system science as a whole.

My past and ongoing research will contribute significantly to laying the scientific groundwork for this upcoming mission. In particular, the systematic comparisons between Trojans, Hildas, and KBOs that I have carried out as part of my graduate thesis work will be indispensable in interpreting the results from *Lucy* and placing them in the broader context of solar system evolution. Furthermore, the color bimodality hypothesis presented in Chapter 4, combined with the related laboratory studies described in Section 8.2, offer a well-defined, testable compositional model for Trojans against which the results of the flyby mission can be interpreted. The future work outlined in this chapter will further hone our understanding of Trojans and related asteroid populations in the years leading up to the spacecraft's launch.

Stepping back to appreciate the immense progress that has been made in planetary science over the past decade, from the newest developments in the theory and observations of an increasingly diverse menagerie of exoplanet systems to the advent of detailed characterization of protoplanetary disk with radio telescopes, it has become clear that the recent concerted effort to test dynamical instability models within our own Solar System is but a small piece in the puzzle. But just as breakthroughs in exoplanetary astronomy may fundamentally change our long-held conceptions of solar system evolution, a continued focus on refining our understanding of Trojans, Hildas, and KBOs – some of the smallest objects of study in astronomy – may someday have far-reaching implications for defining the foundational principles that underlie the formation and evolution of planetary systems across the universe.

References

Brown, M. E. (2016). "The 3 – 4 μm spectra of Jupiter Trojans asteroids". *AJ*, 152, 159.

Grav, T., Mainzer, A. K., Bauer, J., & Masiero, J. (2012). "WISE/NEOWISE observations of the Hilda population: Preliminary results". *ApJ*, 744, 197.

Mahjoub, A., Poston, M. J., Blacksberg, J., & Eiler, J. M. (2017). "Production of sulfur allotropes in electron irradiated Jupiter Trojans ice analogs". *ApJ*, 846, 148.

Mahjoub, A., Poston, M. J., Hand, K. P., & Brown, M. E. (2016). "Electron irradiation and thermal processing of mixed-ices of potential relevance to Jupiter Trojan asteroids". *ApJ*, 820, 141.

Poston, M. J., Mahjoub, A., Blacksberg, J., & Brown, M. E. (2018). "Visible-near-infrared spectral evolution of irradiated astronomical mixed ices and application to Kuiper Belt and Jupiter Trojan small bodies". *ApJ*, submitted.

Takir, D. & Emery, J. P. (2012). “Outer Main Belt asteroids: Identification and distribution of four 3-μm spectral groups”. *Icarus*, 219, 641.

Wong, I. & Brown, M. E. (2016). “A hypothesis for the color bimodality of Jupiter Trojans”. *AJ*, 152, 90.

Wong, I., Brown, M. E., & Emery, J. P. (2017). “0.7 – 2.5 μm spectra of Hilda asteroids”. *AJ*, 154, 104.